RF MEMS Technology for Millimeter-Wave Radar Sensors

by

Koen A. P. A. Van Caekenberghe

A dissertation submitted in partial fulfillment
of the requirements for the degree of
Doctor of Philosophy
(Electrical Engineering)
in The University of Michigan
2007

Doctoral Committee:
Professor Kamal Sarabandi, Chair
Professor Brian E. Gilchrist
Professor Eric Michielssen
Associate Professor Katsuo Kurabayashi

To my wife, Cindy

ACKNOWLEDGEMENTS

As I look back upon my doctoral research work, I would like to acknowledge several people who were instrumental in helping me to complete the Ph.D. program at the University of Michigan. First of all, I acknowledge the support of my wife Cindy Callens and my family: my parents Dirk Van Caekenberghe and Rosette De Knop and my brothers Frank, Steven and Stijn. I am especially grateful to Cindy, who endured a lot of hardship during the Ph.D program, first as my girlfriend and later as my wife. I also thank my grandparents: the late Jozef De Knop and the late Paula Olbrechts, who partly raised me during my childhood, and the late Aloïs Van Caekenberghe and Julia Wuyts who were my first math teachers.

I have been blessed to have met several competent engineers during my education. I obtained the M.Sc. degree in electrical engineering at the Katholieke Universiteit Leuven, Belgium, where Prof. Emmanuel Van Lil introduced me to radar basics. I wrote my M.Sc. thesis at the EADS Systems & Defence Electronics, Ulm, Germany, and I am thankful to Günter Wolf for teaching me radar signal processing. Upon graduation, I joined Thales Naval, Hengelo, the Netherlands, and I am thankful to Robert Oude Velthuis, Dr. Rob Legtenberg and John de Groot for teaching me practical microwave, MEMS, and antenna design respectively. I am especially grateful to Robert, who spent a lot of time bringing me up to speed with EM simulation tools like HP Momentum and Ansoft HFSS, including the macro language which proved to be of great value. At the University of Michigan, Prof. Gabriel Rebeiz and Dr. Tauno Vähä-Heikkilä were my mentors in micro-fabrication and RF MEMS technology. During the summer of 2005, I left Michigan for an internship at Bell Labs, Murray Hill, NJ, where Prof. Yves Baeyens taught me several things about active microwave circuits. I have also learned a lot from discussions with Dr. Bernhard Schönlinner, with Dr. Denis Mercier, and with my colleagues Karl Brakora and Mustafa Rangwala.

I am indebted to the staff of the Michigan Nanofabrication Facility (MNF) which runs a

one-of-a-kind class 100 clean room. In alphabetical order, I thank Gregory Allion, Kimberly Appel, Katherine Beach, Timothy Brock, Russ Clifford, Phil Collica, Aaron Glatzer, Dr. Dennis Grimard, Dr. Robert Hower, James Kulman, Dr. Sandrine Martin, Matthew Oonk, Steven Sostrom, Edward Tang, Brian VanDerElzen and Cedric Whitney. I thank Prof. Dimitrios Peroulis and Dr. Lee Harle for reviewing RF MEMS related research papers.

I thank all people with whom I have spent much time in the EECS 3421 office over the years: Carsten Barth, Tanja Biedermann, Dr. Amelia Buerkle, Karl and Kenneth Brakora, Dr. Lee Harle, and Jacqueline Vitaz.

Finally, I acknowledge the hospitality of the nearly extinct Dutch and Flemish community of Ann Arbor. I am especially grateful to Karla and Hugo Vandersypen, as well as to Prof. Ton Broos, the organizer of the Dutch Lunches.

TABLE OF CONTENTS

LIST OF TABLES

Table

LIST OF FIGURES

Figure

LIST OF APPENDICES

Appendix

CHAPTER 1

Introduction

1.1 RF MEMS Technology

The RF MEMS acronym stands for radio frequency microelectromechanical system, and refers to components of which freestanding or moving sub-millimeter-sized parts provide RF functionality. RF functionality can be implemented using a variety of passive and active RF technologies. Besides RF MEMS (passive) technology, ferrite (passive), ferroelectric (passive), GaAs (active), GaN (active), InP (active), RF CMOS (active), Sb (active), SiC (active), and SiGe (active) technology are available to the RF designer. Each of the RF technologies offers a distinct trade-off between cost, frequency, gain, large scale integration, linearity, noise figure, packaging, power consumption, power handling, reliability, size, supply voltage, switching time and weight. RF MEMS components offer low insertion loss and high isolation, linearity, power handling and Q factor, do not consume power, but require a high supply voltage and in-situ wafer-level, liquid crystal polymer (LCP) or low temperature co-fired ceramic (LTCC) packaging.

1.1.1 Components

There are various types of RF MEMS components, such as RF MEMS resonators and self-sustained oscillators with low phase noise [1], RF MEMS tunable inductors [2], and RF MEMS switches, switched capacitors and varactors. The devices discussed in the dissertation are based on RF MEMS switches, switched capacitors and varactors [3].

RF MEMS switches, switched capacitors and varactors are classified by actuation method (electrostatic, magnetic, piezoelectric, thermal), by contact mechanism (capacitive, ohmic),

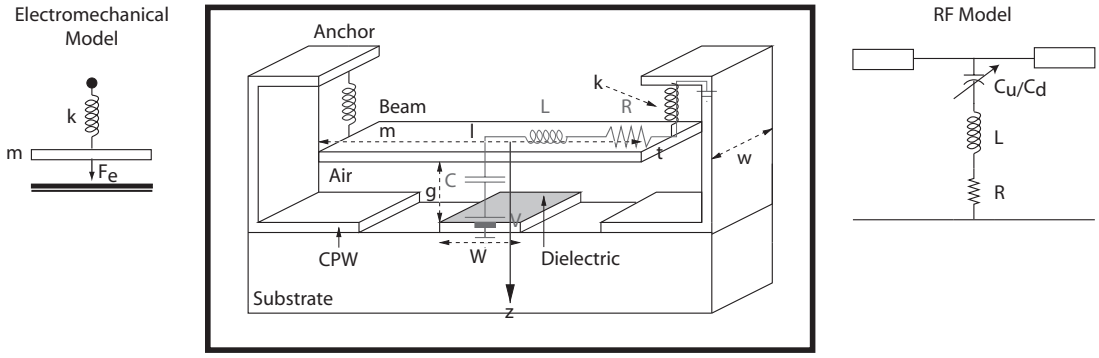

Figure 1.1: The capacitive fixed-fixed beam RF MEMS switch

or by anchor mechanism (cantilever, fixed-fixed beam). The component shown in Fig. 1.1, is a center-pulled capacitive fixed-fixed beam RF MEMS switch, developed and patented by Raytheon in 1993 [4, 5]. A capacitive fixed-fixed beam RF MEMS switch is in essence micro-machined capacitors with a moving top electrode - i.e. the beam.

From an electromechanical perspective, the component behaves like a mass-spring system, actuated by an electrostatic force. The effective mass of the beam is given by (1.1),

$$m = 0.4\,\rho\,l\,w\,t \tag{1.1}$$

in which l, t, w, are the dimensions of the beam, as shown in Fig. 1.1, and ρ is the mass density of the beam material. Because the beam is fixed at both ends, the moving mass of the beam is discounted by 60% [3]. The spring constant, k, is given by (1.2),

$$k = 32\,E\,w\left(\frac{t}{l}\right)^3\left(\frac{27}{49}\right) + 8\,\sigma\,(1-\nu)\,w\,\frac{t}{l}\left(\frac{3}{5}\right) \tag{1.2}$$

in which E, is the Young's modulus, σ is the residual stress, ν is the Poisson ratio of the beam material. The electrostatic force, F_e, is a function of the capacitance, C, and the bias voltage, V_s. Knowledge of k and m allows for calculation of the pull-in voltage, V_p, which is the bias voltage necessary to pull-in the beam, and the switching time, t_s. V_p is given by (1.3).

$$V_p = \sqrt{\frac{8\,k\,(g_0 + t_d/\epsilon_d)^3}{27\,\epsilon_0\,A}} \tag{1.3}$$

in which $A = W\,w$, g_0 is the gap between the beam and the dielectric, t_d is the thickness of the dielectric, and ϵ_d is the dielectric constant of the dielectric. The switching time, t_s,

is given by (1.4).

$$t_s = 3.67 \frac{V_p}{V_s \sqrt{k/m}} \tag{1.4}$$

From an RF perspective, the components behave like a series RLC circuit with negligible resistance, R, and inductance, L. The up-state capacitance, C_u, is given by (1.5), and the down-state capacitance, C_d, is given by (1.6)

$$C_u = 1.4 \frac{\epsilon_0 A}{g_0 + t_d/\epsilon_d} \tag{1.5}$$

$$C_d = 0.65 \frac{\epsilon_0 \epsilon_d A}{t_d} \tag{1.6}$$

C_u is assumed to be 40% larger than the parallel plate value due to fringing fields, and C_d is assumed 35% smaller than the parallel plate value due to surface roughness of the dielectric [3]. C_u and C_d are in the order of 50 fF and 1.2 pF, which are functional values for millimeter-wave circuit design. The capacitance ratio, $C_R = C_d/C_u$, is in the order of 30 or higher. A high capacitance ratio is a prerequisite for high isolation. Other examples of RF MEMS switches are ohmic cantilever switches [6, 7], and capacitive single pole N throw (SPNT) switches based on the axial gap wobble motor [8].

RF MEMS switched capacitors are capacitive fixed-fixed beam switches with a low capacitance ratio. RF MEMS varactors are capacitive fixed-fixed beam switches which are biased below pull-in voltage. RF MEMS switched capacitors and varactors have a capacitance ratio of about 1.2 to 10. The Q factor, as given by (1.7), is between 20 and 50 in the X-, Ku- and Ka-band.

$$Q = \frac{1}{\omega R C_u} \tag{1.7}$$

1.1.2 Microfabrication

RF MEMS fabrication processes allow for integration of thin film resistors (SiCr, TaN), metal-air-metal (MAM) capacitors, metal-insulator-metal (MIM) capacitors, and RF MEMS components. RF MEMS components can be fabricated in class 100 clean rooms using 6 to 8 lithography steps, whereas state-of-the-art MMIC and RFIC fabrication processes require 13 to 25 lithography steps. Essential microfabrication steps are:

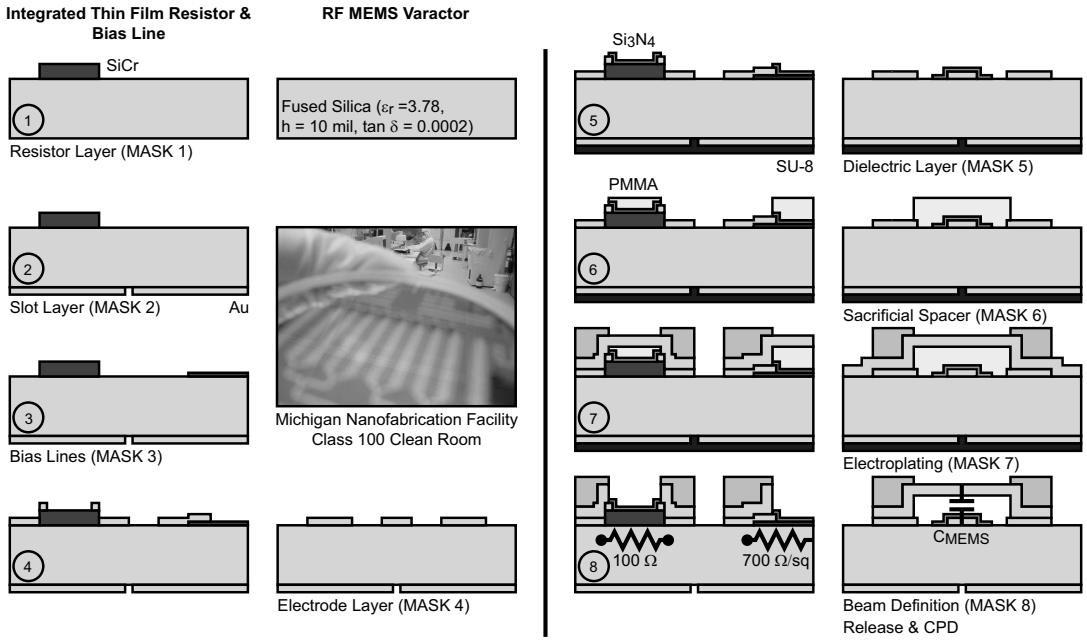

Figure 1.2: RF MEMS fabrication process

- Deposition of the bias lines (Fig. 1.2, step 3)
- Deposition of the electrode layer (Fig. 1.2, step 4)
- Deposition of the dielectric layer (Fig. 1.2, step 5)
- Deposition of the sacrificial spacer (Fig. 1.2, step 6)
- Deposition of seed layer and subsequent electroplating (Fig. 1.2, step 7)
- Beam definition, release and critical point drying (Fig. 1.2, step 8)

RF MEMS fabrication processes, unlike MMIC or barium strontium titanate (BST) ferroelectric fabrication processes, do not require molecular beam epitaxy (MBE) or metal organic chemical vapor deposition (MOCVD). With the exception of the removal of the sacrificial spacer, all fabrication steps are compatible with CMOS fabrication processes.

1.1.3 Packaging

In-situ wafer-level packaging (chip capping, thin film capping) [9], liquid crystal polymer (LCP) packaging [10], and low temperature co-fired ceramic (LTCC) packaging for RF-MEMS components have been developed and characterized. Package design encompasses

RF design, thermomechanical design, and design for reliability. Package characterization includes RF, temperature stability, and hermeticity measurements.

1.1.4 Reliability

Contact region deformation poses a reliability issue for ohmic cantilever RF MEMS switches, while dielectric charging induced beam stiction poses a reliability issue for capacitive fixed-fixed beam RF MEMS switches. Anno 2007, commercially-available ohmic cantilever RF MEMS switches and capacitive fixed-fixed beam RF MEMS switches have reached a lifetime in excess of 100 billion cycles [11].

1.2 Radar Sensors

Radio detection and ranging (radar) is used to sense angle, range and velocity of (moving) scatterers in the environment [12, 13, 14]. Radar sensor figures of merit include field of view in terms of solid angle and maximum unambiguous range and velocity, as well as angular, range and velocity resolution. Applications of radar sensors include autonomous cruise control (ACC), autonomous landing guidance (ALG), altimetry, air traffic management (ATM), early warning, fire control, forward warning collision sensing (FWCS), ground penetrating radar (GPR), surveillance, and weather forecasting. Radar sensors are classified by architecture, radar mode, platform, and propagation window.

1.2.1 Architecture

- **Bistatic** versus **monostatic**: Bistatic radars have a spatially-dislocated transmitter and receiver. Monostatic radars have a spatially co-located transmitter and receiver. Bistatic radars benefit from increased target visibility due to forward radar cross section (RCS) enhancement, but lack stereoscopic vision. Bistatic radars are rumored to be able to detect stealth targets which have virtually no backscatter RCS.

- **Electronical** versus **mechanical scanning**: The angle of a target is detected by scanning the field of view with a highly directive beam. Scanning is done electronically, by scanning the beam of an array, or mechanically, by rotating an antenna. An electronically scanned array (ESA), or a phased array, offers several advantages over

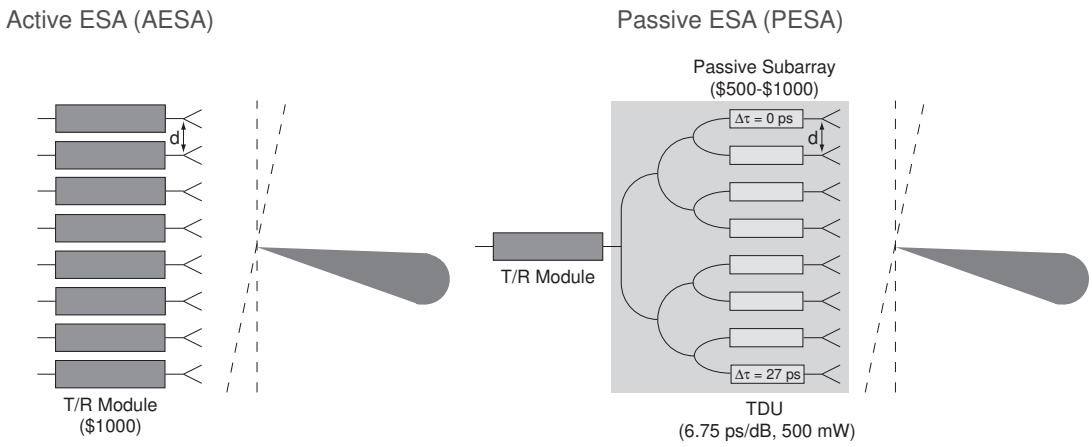

Figure 1.3: Active versus passive ESA

a mechanically scanned antenna, such as instantaneous beam scanning, the availability of multiple concurrent agile beams, and concurrently operating radar modes. Figures of merit of an ESA are the bandwidth, the effective isotropically radiated power (EIRP) and the G_r/T quotient, the field of view, and the half-power beamwidth (HPBW). EIRP is the product of the transmit gain, G_t, and the transmit power, P_t. G_r/T is the quotient of the receive gain and the antenna noise temperature. A high EIRP and G_r/T are a prerequisite for long-range detection. Design choices are:

- **Active** versus **passive** (see Fig. 1.3): In an active electronically scanned array (AESA), each antenna is connected to a T/R module featuring solid state power amplification (SSPA). An AESA has distributed power amplification and offers high performance and reliability, but is expensive. In a passive electronically scanned array (PESA), the array is connected to a single T/R module featuring vacuum electronics devices (VED). A PESA has centralized power amplification and offers cost savings, but requires low-loss phase shifters.
- **Aperture**: The aperture of a radar sensor is real or synthetic. Real-beam radar sensors allow for real-time target sensing. Synthetic aperture radar (SAR) allows for an angular resolution beyond real beamwidth by moving the aperture over the target, and adding the echoes coherently.
- **Architecture**: The field of view is scanned with a highly directive-frequency-orthogonal (slotted waveguide), spatially-orthogonal (switched beamforming net-

works), or time-orthogonal beams [15, 16]. In case of time-orthogonal scanning, the beam of an ESA is preferably scanned by applying a progressive time delay, $\Delta\tau$, constant over frequency, instead of applying a progressive phase shift, constant over frequency. Usage of true-time-delay (TTD) phase shifters avoids beam squinting with frequency. The scanning angle, θ, as given by (1.8)-(1.9), is expressed as a function of the phase shift progression, β, which is a function of the frequency and the progressive time delay, $\Delta\tau$, which is invariant with frequency:

$$k\,d\,\cos\theta = \beta\,(f) = 2\,\pi\,\frac{c}{\lambda_0}\,\Delta\tau \tag{1.8}$$

$$\theta = \arccos\left(\frac{c}{d}\,\Delta\tau\right) \tag{1.9}$$

Note that θ is not a function of frequency. A constant phase shift over frequency has important applications as well, albeit in wideband pattern synthesis. For example, the generation of wideband monopulse Σ/Δ receive patterns depends on a feed network which combines two subarrays using a wideband hybrid coupler.

- **Beam forming**: The beam is formed in the digital, intermediate frequency (IF), optical, or RF domain. Digital beam forming (DBF) receivers offer instantaneous beam forming capabilities limited only by computing power, but require low noise amplifiers (LNA), mixers and analog to digital converters (ADC) with a wide dynamic range. Optical beam forming receivers offer TTD beam steering across large apertures, but suffer from high conversion losses. RF beam forming is the most common beam forming method and does not require coherent distribution of the local oscillator (LO) signal across the aperture.
- **Construction**: An electronically scanned array is a brick, stick, tile, or tray construction. Brick and tray refer to a construction approach in which the RF circuitry is integrated perpendicular to the array plane. Tile, on the other hand, refers to a construction approach in which the RF circuitry is integrated on substrates parallel to the array plane. Stick refers to a construction approach in which the RF circuitry is connected to a line array in the array plane.
- **Feed Network**: The feed network is constrained (corporate, series) or space-fed (lens, reflect-array).

  - **Grid**: The grid is periodic (rectangular, triangular) or aperiodic (thinned).
  - **Polarization**: Ground-based radar sensors are vertically polarized in order to reduce multipath (Brewster angle). All-weather radar sensors are polarimetric.

- **FMCW** versus **pulse-Doppler**: The range, R, and radial velocity, v, of a target are detected through frequency modulation (FM) ranging and range differentiation, or through pulse delay ranging and the Doppler effect (pulse-Doppler). FM ranging is based on the measurement of a frequency shift, Δf, between the transmitted and received chirp, as given by (1.10).

$$R = c\frac{T_c}{2}\frac{\Delta f}{f_m} \tag{1.10}$$

in which c is the speed of light, f_m is the maximum frequency shift of the chirp and T_c is the duration of the chirp. v is given by (1.11).

$$v = \frac{\mathrm{d}\,R}{\mathrm{d}\,t} \tag{1.11}$$

Pulse-delay ranging, as given by (1.12), is based on the measurement of the time difference, Δt, between the transmitted and received pulse. v is given by (1.13).

$$R = c\frac{\Delta t}{2} \tag{1.12}$$

$$v = \frac{f_D\,\lambda_0}{2} \tag{1.13}$$

in which f_D is the Doppler frequency shift between the transmitted and received pulse. Pulse-Doppler radar sensors are half-duplex, while FMCW radar sensors are full-duplex. Hence, pulse-Doppler radar sensors provide higher isolation between transmitter and receiver, increasing the receiver's dynamic range (DR) and the range detection considerably. In addition, an antenna or an array can be time-shared between transmitter and receiver, whereas FMCW radars require two antennas or arrays, one for transmit and one for receive. A drawback of half-duplex operation is the existence of a blind zone in the immediate vicinity of the radar sensor, as given by (1.14),

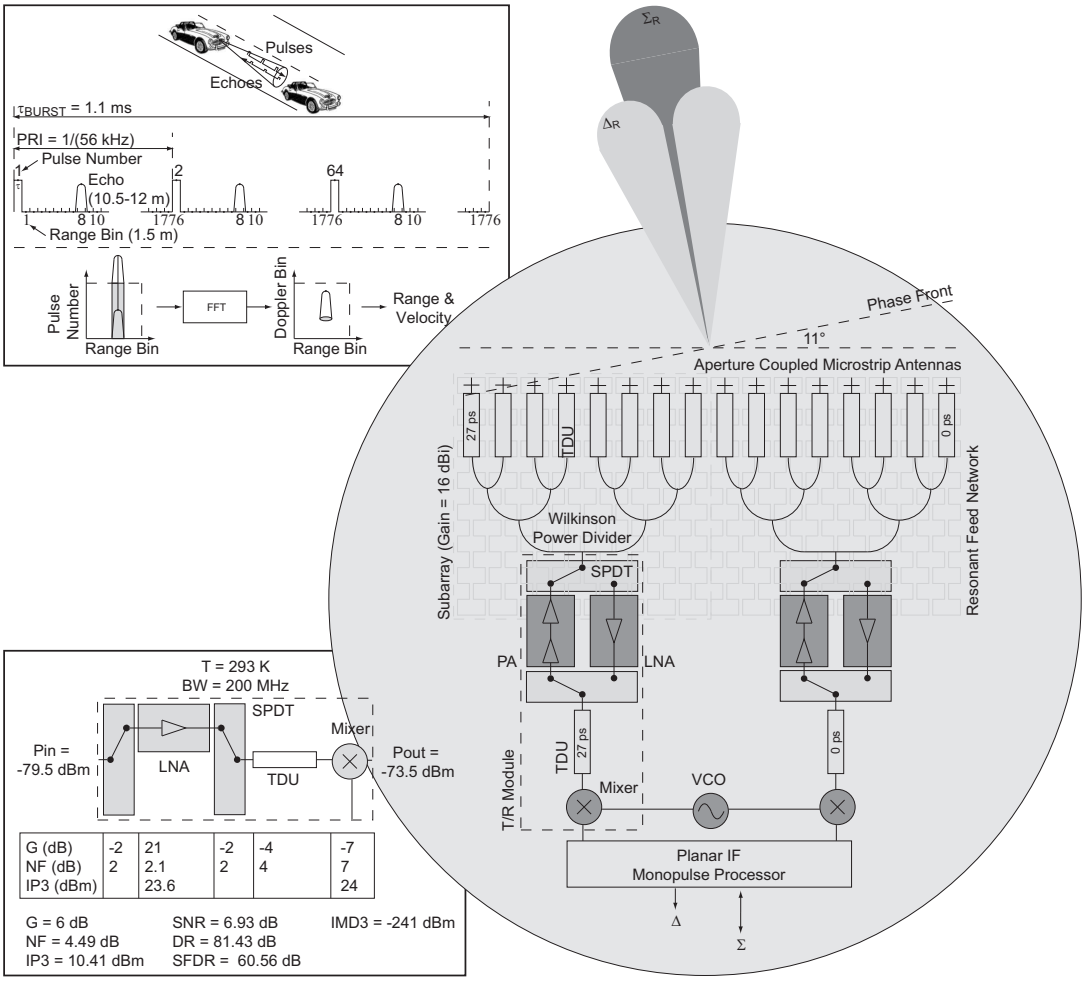

Figure 1.4: A passive electronically scanned array with a monopulse feed network

$$R_b = c\,(\Delta\tau + t_s)/2 \tag{1.14}$$

in which t_s is the switching time of the T/R switch. Pulse-Doppler radar sensors are therefore more suited for long-range detection, whereas FMCW radar sensors are more suited for short-range detection. The range resolution, r, is limited by the instantaneous signal bandwidth, $r = c/(2\,BW)$, in both pulse-Doppler and frequency modulated continuous wave (FMCW) radar sensors.

Extensions for pulse-Doppler radar sensors are:

– **Monopulse**: Monopulse feed networks are the proverbial cross hairs of the radar

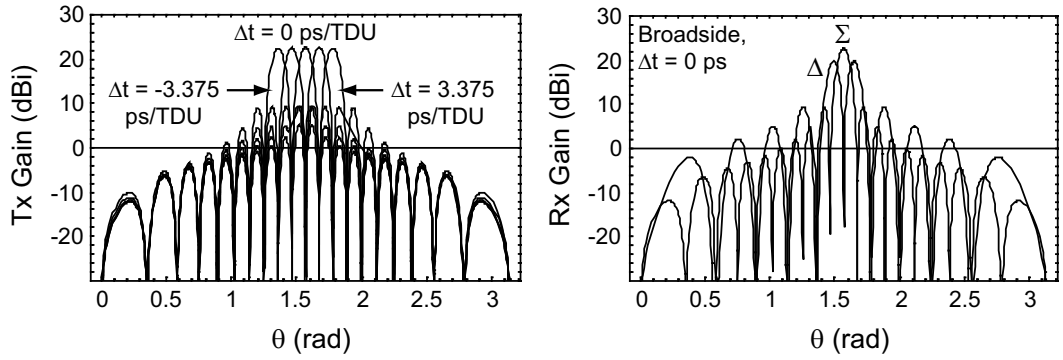

(a) Transmit radiation patterns

(b) Sum and azimuth-difference receive radiation patterns

Figure 1.5: Simulated radiation patterns of the ESA with monopulse feed network, as shown in Fig. 1.4

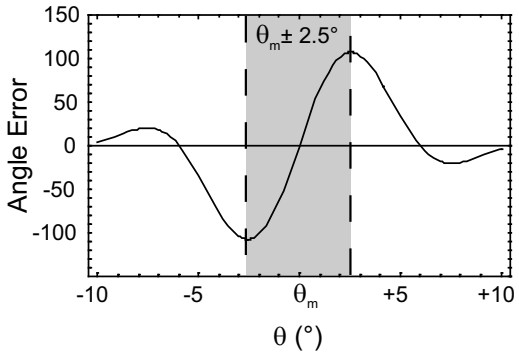

Figure 1.6: Simulated monopulse angle error. θ_m is the scanning angle.

sensor. A monopulse feed network, as shown in Fig. 1.4, increases the angular accuracy to a fraction of the beamwidth by comparing echoes, which originate from a single radiated pulse and which are received in two or more concurrent and spatially-orthogonal beams. The pulse is transmitted through the sum channel only. The transmit patterns of the ESA with monopulse feed, shown in Fig. 1.4, are shown in Fig. 1.5(a). Upon reception, echoes are received in both sum and difference channel which correspond to two concurrent spatially-orthogonal beam patterns. The monopulse receive patterns of the ESA with monopulse feed, shown in Fig. 1.4, are shown in Fig. 1.5(b). The monopulse comparator extracts the angle error, e, from a single echo and feeds it back to the beam steering controller until it is zero. e, as shown in Fig. 1.6, is given by (1.15)

$$e = \frac{\vec{\Sigma} \cdot \vec{\Delta}}{||\vec{\Sigma}||} \tag{1.15}$$

in which $\vec{\Sigma}$ is the echo signal received in the sum channel, and $\vec{\Delta}$ is the echo signal received in the azimuth-difference channel [13].

Spatial orthogonality, and not frequency, polarization or time orthogonality, is the essence of monopulse, meaning that the echoes are received at the same time, using the same polarization, and at the same frequency. Sequential lobing uses time orthogonality, conical scan uses spatial and time orthogonality and subpulsing uses frequency and time orthogonality. Sequential lobing, conical scan and subpulsing are easier to implement but yield a lower angular resolution improvement.

- **Pulse compression**: Pulse compression derelates the pulse width and the instantaneous signal bandwidth, which are otherwise inversely related. The pulse width is related to the time-on-target, the signal to noise ratio (SNR) and the maximum range. The instantaneous signal bandwidth is related to the range resolution.
- **Pulse-Doppler processing**: Echoes originating from a radiated coherent burst are transformed to the spectral domain using a discrete Fourier transform (DFT). In the spectral domain, stationary clutter can be removed because it has a Doppler frequency shift which is different from the Doppler frequency shift of the moving target. The range and velocity of a target can be estimated with increased SNR due to coherent integration of echoes [17].

1.2.2 Platform

Clutter and environmental conditions are platform-dependent. Mobile platforms require low power consumption, small size, and low weigth, and represent an opportunity for RF MEMS technology. Examples of platforms are airborne, car-borne, ship-borne, space-borne, and ground-based platforms.

1.2.3 Propagation Window

The radar frequency is selected based on radar sensor size, target range, target RCS, which is frequency-dependent, and technology readiness level (TRL) considerations. Examples of propagation windows with low path loss are the 3 GHz (S), 10 GHz (X), 24 GHz (K), 35 GHz (Ka), 77 GHz (W), and 94 GHz (W) propagation windows.

1.2.4 Radar Mode

Radar modes for point targets, which are electrically-small targets with constant RCS, include search and track. Radar modes for distributed targets, which are electrically-large targets with fluctuating RCS, include ground mapping and target classification. The radar mode sets the radar waveform.

1.3 RF MEMS Technology for Radar Sensors

Tunable antennas and filters for multi-band radios, and passive electronically scanned arrays and T/R modules for radar sensors, represent an opportunity for RF MEMS technology.

1.3.1 Antennas

Polarization and radiation pattern reconfigurability, and frequency tunability, are usually achieved by incorporation of lumped components based on III-V semiconductor technology, such as single pole single throw (SPST) switches or varactor diodes. However, these components can be readily substituted for RF MEMS switches and varactors in order to take advantage of the low insertion loss and high Q factor offered by RF MEMS technology. In addition, RF MEMS components can be integrated monolithically on low-loss dielectric substrates, such as borosilicate glass, fused silica or LCP, whereas III-V semiconducting substrates are generally lossy and have a high dielectric constant. A low loss tangent and low dielectric constant are of importance for the efficiency and the bandwidth of the antenna.

The prior art includes an RF MEMS frequency tunable fractal antenna for the 0.1-6 GHz frequency band [18], an RF MEMS frequency tunable slot antenna for the 2.4-4.6 GHz band [19], an RF MEMS radiation pattern reconfigurable spiral antenna for 6 and 10 GHz [20], an RF MEMS radiation pattern reconfigurable spiral antenna for the 6-7 GHz

frequency band based on packaged Radant MEMS SPST-RMSW100 switches [21], and an RF MEMS Sierpinski multiband fractal antenna for 2.4 and 18 GHz [22]. A 2-bit Ka-band RF MEMS frequency tunable slot antenna is discussed in chapter 3.

1.3.2 Filters

RF bandpass filters are used to increase out-of-band rejection, if the antenna fails to provide sufficient selectivity. Out-of-band rejection eases the dynamic range requirement of LNA and mixer in the light of interference. Off-chip RF bandpass filters based on lumped ceramic, surface acoustic wave (SAW), quartz crystal, and thin film bulk acoustic resonator (FBAR) resonators have superseded distributed RF bandpass filters based on transmission line resonators, printed on substrates with low loss tangent, or based on waveguide cavities. RF MEMS resonators offer the potential of on-chip integration of high-Q resonators and low-loss bandpass filters. The Q factor of RF MEMS resonators is in the order of 1000-1000 [1].

Tunable RF bandpass filters offer a significant size reduction over switched RF bandpass filter banks. They can be implemented using III-V semiconducting varactors, barium strontium titanate (BST) ferroelectric and RF MEMS switches, switched capacitors and varactors, and yttrium-on-garnet (YIG) ferrites. RF MEMS technology offers the tunable filter designer a compelling trade-off between insertion loss, linearity, power consumption, power handling, size, and switching time [23]. Tunable RF bandpass filters based on III-V semiconducting varactors, such as reverse biased PIN diodes, have a lower switching time, but a higher insertion loss and lower linearity and power handling [24]. BST ferroelectric tunable filters currently lack the performance of RF MEMS tunable filters. YIG ferrite filters, based on magnetostatically-tuned gyrotropic resonance, have lower insertion loss and switching time, but have a considerable higher power consumption, size and weight.

1.3.3 Phase Shifters

A phase shifter provides a controlled phase shift of the RF signal. Figures of merit of RF MEMS phase shifters are the number of effective bits (if digital), the loss (if passive), the group velocity dispersion, the linearity, the phase shift / noise figure or the group delay / noise figure, the power handling, the reliability, the size, and the switching time. Loaded-line, reflection, switched-network, and switched-line phase shifters designs have been

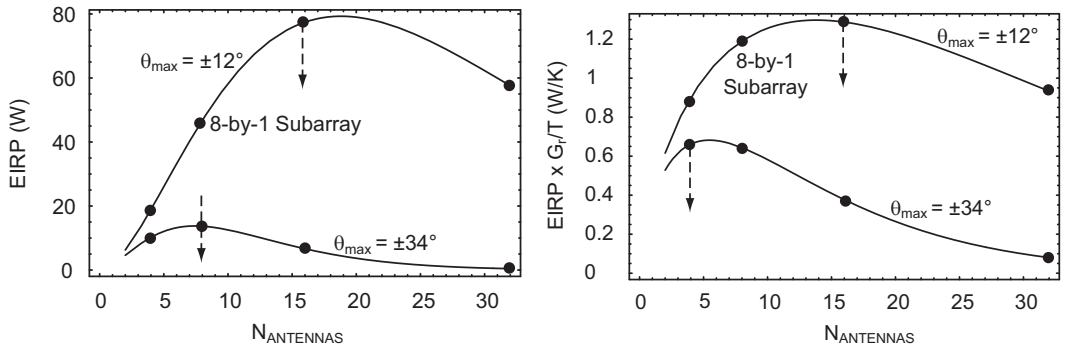

(a) EIRP

(b) EIRP $\times$ G_r/T

Figure 1.7: EIRP and EIRP $\times$ G_r/T versus number of antenna elements in a passive subarray

implemented using RF MEMS technology.

RF MEMS phase shifters have enabled wide-angle passive electronically scanned arrays (PESA) with high effective isotropically radiated power (EIRP), also referred to as the power-aperture product, and high G_r/T. A high EIRP and G_r/T are a prerequisite for long-range detection. The EIRP and G_r/T are a function of the number of antenna elements per subarray, and of the maximum scanning angle θ_m. The number of antenna elements per subarray should be chosen in order to optimize the EIRP or the EIRP $\times$ G_r/T product, as shown in Fig. 1.7(a) and Fig. 1.7(b).

Due to the low insertion loss and the high power handling of RF MEMS phase shifters, a PESA based on RF MEMS technology offers an alternative to the active electronically scanned array (AESA) solution. The statement is illustrated with examples in Fig. 1.8: assume a one-by-eight passive subarray is used for transmit as well as receive, with following characteristics: $f = 38$ GHz, $G_r = G_t = 10$ dBi, BW $= 2$ GHz, $P_t = 4$ W. The low loss (6.75 ps/dB) and good power handling (500 mW) of the RF MEMS TTD phase shifters allow an EIRP of 40 W and a G_r/T of 0.036 1/K. What is the maximum range for which targets can be detected with 10 dB of SNR at the input of the receiver? The radar range equation, given by (1.16),

$$R = \sqrt[4]{\frac{\lambda_0^2 \, EIRP \, G_r/T \, \sigma}{64 \, \pi^3 \, k_B \, BW \, SNR}} \tag{1.16}$$

in which k_B is the Boltzmann constant, λ_0 is the free-space wavelength, and σ is the RCS of the target. Range values are tabulated in Table 1.1 for following targets: a sphere with

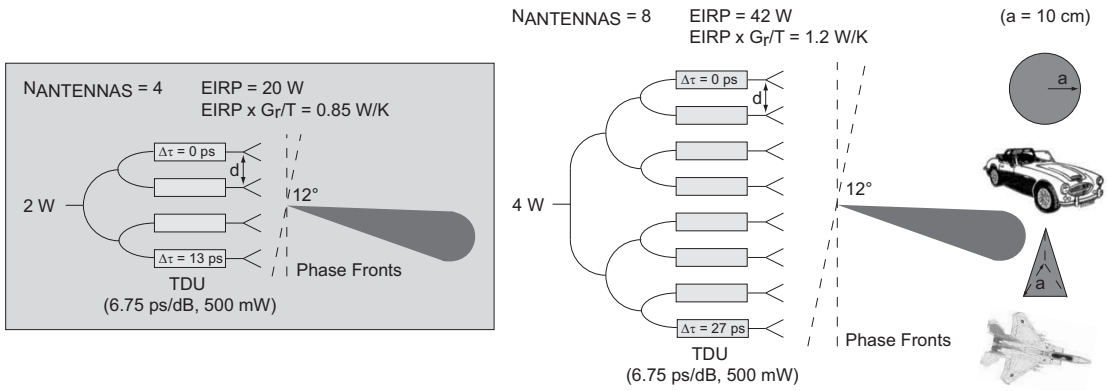

Figure 1.8: EIRP $\times$ G_r/T for a one-by-four and a one-by-eight element passive subarray

Table 1.1: Maximum detectable range (SNR = 10 dB)

	(m^2)	Range (m)
Sphere	0.0314	10
Rear of car	20	51
Dihedral corner reflector	60.9	67
Fighter jet	400	107

a radius, a, of 10 cm ($\sigma = \pi\, a^2$), a dihedral corner reflector with facet size, a, of 10 cm ($\sigma = 12\pi\, a^4/\lambda^2$), the rear of a car ($\sigma$ = 20 m^2) and for a contemporary non-evasive fighter jet (σ = 400 m^2). A Ka-band hybrid ESA capable of detecting a car 100 m in front and engaging a fighter jet at 10 km can be realized using 2.5 and 422 passive subarrays (and T/R modules), respectively.

The usage of TTD phase shifters instead of RF MEMS phase shifters allows ultra-wideband (UWB) radar waveforms with associated high range resolution, and avoids beam squinting or frequency scanning. TTD phase shifters are designed using the switched-line principle [25, 26, 27] or the distributed loaded-line principle [28, 29, 30, 3, 31, 32, 33]. Switched-line TTD phase shifters are superior to distributed loaded-line TTD phase shifters in terms of time delay per decibel noise figure (NF), especially at frequencies up to X-band, but are inherently digital and require low-loss and high-isolation SPNT switches. Distributed loaded-line TTD phase shifters, however, can be realized analogously or digitally,

and in smaller form factors, which is important at the subarray level. Analog phase shifters are biased through a single bias line, whereas multibit digital phase shifters require a parallel bus along with complex routing schemes at the subarray level. In addition, usage of an analog bias voltage avoids large phase quantization errors, which deteriorate the EIRP and beam-pointing accuracy, and elevate the sidelobe level of an electronically scanned array [15].

The prior art, as shown in Fig. 1.9, includes an X-band continuous transverse stub (CTS) array fed by a line array of sixteen 5-bit reflect-type RF MEMS phase shifters, demonstrated by Raytheon in 2002. The ESA scans 90° in the H-plane, but the reflect-type phase shifters make the design narrow-band [34, 35]. A 2-D time-delaying lens consisting of parallel-plate waveguides and featuring 250,000 RF MEMS switches was demonstrated by Radant MEMS in 2006. The lens is illuminated with a transverse electromagnetic (TEM) wave and TTD phase shifting is achieved by periodically loading the parallel-plate waveguides with tunable capacitive LCP diaphragms based on hermetically packaged RF MEMS switches [36]. Both radar sensors operate at X-band and are based on ohmic contact RF MEMS switches. A switched beam forming network (BFN) based on an RF MEMS SP4T switch and a Rotman lens, was demonstrated by Bosch and IMEC in 2006 [37]. As discussed in chapter 4, the transmit power and EIRP of a switched BFN are limited by the power handling of the SPNT switch. Chapter 5 discusses an analog RF MEMS slotline TTD phase shifter for a 2-D time delaying lens.

1.3.4 T/R Modules

Following RF MEMS devices could be used within a T/R module, as shown in Fig. 1.10:

- **RF MEMS limiter**: RF MEMS limiters could be used to protect the LNA.
- **RF MEMS T/R switch**: RF MEMS T/R switches could replace the ferrite circulators, which occupy a large area. However, the high switching time drastically increases the blind zone, as given by (1.14). To date, RF MEMS T/R switches could only be used in low PRF and medium PRF radar waveforms for long-range detection, which use pulse compression and therefore have a duty cycle in the order of microseconds. Scaling of the critical dimensions of RF MEMS components, as discussed in chapter 2, offers the potential of submicrosecond T/R switching times.

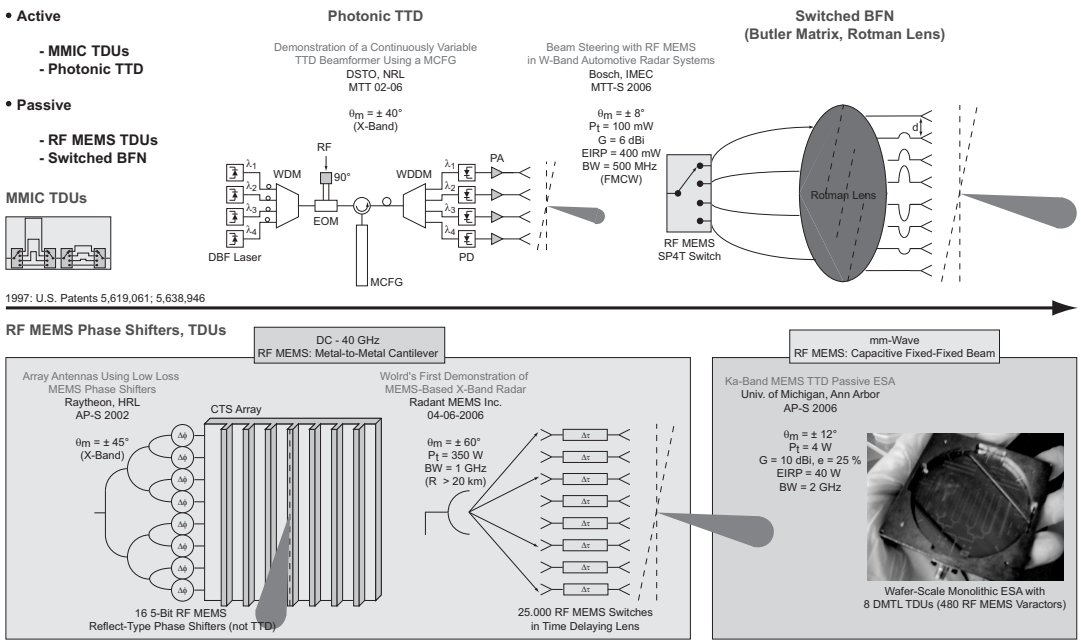

Figure 1.9: TTD beamformers

- **RF MEMS TTD phase shifter**: RF MEMS TTD phase shifters are passive and reciprocal. As such, the use of RF MEMS phase shifters simplifies the T/R module design, as shown in Fig. 1.10, because less SPDT switches are required between the three ports of the T/R module to route the RF signal through active and unidirectional phase shifters [38].

- **RF MEMS tunable matching network**: RF MEMS tunable matching networks could be used to maintain maximum transmit power while scanning, by load-pulling the power amplifier in order to cope with a changing active element impedance [39, 40].

1.4 Overview of the Thesis

This thesis discusses RF MEMS technology for millimeter-wave radar sensors.

Chapter 2 discloses a self-aligned fabrication process for capacitive fixed-fixed beam RF MEMS components. It enables scaling of the critical dimensions and reduces the number of processing steps by 40% as compared with a conventional RF MEMS fabrication process. RF MEMS varactors with beam lengths of 30 μm are demonstrated using the self-aligned fabrication process, and the performance of a 4 by 4 RF MEMS varactor bank is discussed

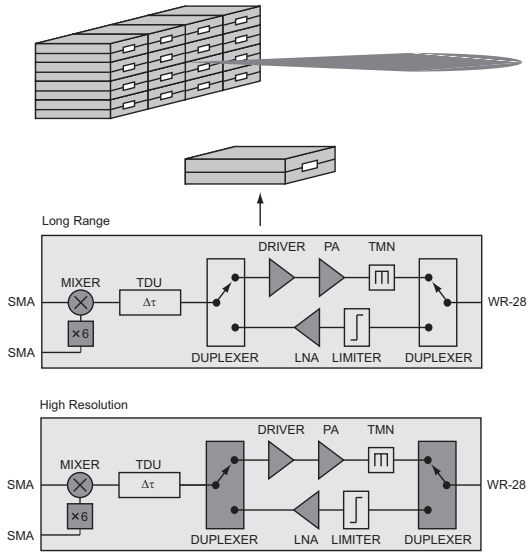

Figure 1.10: RF MEMS devices in a T/R module

as well. At 20 GHz, the measured capacitance values range between 180.5 fF and 199.2 fF. The measured capacitance ratio is 1.15, when a driving voltage of 35 V is applied, and the measured loaded Q factor ranges between 14.5 and 10.8. The measured cold-switched power handling is 200 mW.

Chapter 3 discloses a 2-bit Ka-band RF MEMS frequency tunable slot antenna. It is demonstrated on a fused silica wafer using a micro-fabrication process requiring 6 masks. The return loss and gain for each of the 4 states are measured using a probe station based setup for on-wafer antenna measurements. The antenna has a measured tunable bandwidth of 6.8 GHz. The average measured gain is 1.74 dBi, and the average measured cross-polarization is -9.22 dBi. The extracted switching time is 5.19 μs for a drive voltage of 45 V.

Chapter 4 discloses a high-power X-band differential RF MEMS SPST switch which is an ideal candidate for integration in the SPNT switches of switched BFNs. SPNT switches are used to scan the beam of switched BFNs, based on, for example, the Butler matrix or the Rotman lens, by commutating between the N beam ports. Switched BFNs are passive ESAs of which the power-aperture product at X-band is limited by the linearity or the power handling, and the insertion loss of the SPNT switch. The switching time is set by the burst time of the radar waveform or by the time-on-target of the radar mode, which are usually in the order of milliseconds. Usage of the presented SPST switches

therefore dramatically improves the power-aperture product, with virtually no downside. The discussed SPST switch has a simulated cold-switched power handling of 10 W, and demonstrates high measured isolation (> 70 dB from 8-12 GHz) in the OFF-state, as well as low measured insertion loss (< 1 dB from 8-12 GHz) in the ON-state. The measured pull-in voltage is between 25 and 30 V and the simulated switching time is 6.6 μs.

Chapter 5 discloses an analog RF MEMS slotline TTD phase shifter, for use in conjunction with tapered slot antennas, such as the Vivaldi aerial and the double exponentially tapered slot antenna. The design is a scalable distributed loaded-line cascade of 62 novel differential slow-wave unit cells. Each differential slow-wave unit cell comprises an electrically-short slotline section, which is loaded with a shunt impedance consisting of two center-pulled contactless fixed-fixed beam RF MEMS varactors in series, sharing a common electrode. The analog RF MEMS slotline true time delay phase shifter is demonstrated on a borosilicate glass wafer using a micro-fabrication process requiring 6 masks. It is designed for transistor to transistor logic (TTL) bias voltage levels and exhibits a measured phase shift of 28.2°/dB (7.8 ps/dB) and 59.2°/cm at 10 GHz, maintaining a 75 Ω differential impedance match ($S_{11_{dd}}$ < -15.8 dB). The input third-order intercept point (IIP3) is 5 dBm at 10 GHz for a Δf of 50 kHz, measured in a 100 Ω differential transmission line system. Design and fabrication opportunities, concerning distortion and loss reduction, as well as packaging, are highlighted.

Chapter 6 discloses a 94 GHz orthogonal frequency division multiplexing (OFDM) frequency scanning radar (FSR) for autonomous landing guidance, which is a novel phased array concept. The invention juxtaposes commercially-available waveguide components, such as a wide-angle helical waveguide-fed slot array and vacuum electronics devices (VEDs), with emerging technologies such as OFDM ultra wideband (UWB) transceivers.

The first appendix discusses a 2 to 40 GHz probe station based setup for on-wafer antenna measurements. The setup allows for measurement of return loss and radiation patterns of an on-wafer antenna - henceforth referred to as the antenna under test (AUT), radiating at broadside and fed through a coplanar waveguide (CPW). It eliminates the need for wafer dicing and custom-built test fixtures with coaxial connectors or waveguide flanges by contacting the AUT with a coplanar microwave probe. In addition, the AUT is probed exactly where it will be connected to a transceiver IC later on, obviating de-embedding of the measured data. Sources of measurement errors are related to calibration, insufficient

dynamic range, misalignment, forward scattering from nearby objects, and vibrations. The performance of the setup is demonstrated from 2 to 40 GHz through measurement of an on-wafer electrically small slot antenna ($\lambda_0/35 \times \lambda_0/35$, 3.5 × 3.5 mm^2) radiating at 2.45 GHz and an aperture coupled microstrip antenna (2.4 × 1.7 mm^2) radiating at 38 GHz.

The second appendix discloses a 2.45 GHz electrically small slot antenna ($\lambda_0/35 \times \lambda_0/35$, 3.5 × 3.5 mm^2). Miniaturization is achieved through symmetric inductive loading of an electrically small slot section. It is fabricated on a low-loss fused silica wafer through a back-etch of a 5000 Å golden metal film, which is 31.5% of the skin depth at 2.45 GHz. The measured bandwidth is 106 MHz and the measured gain is -15 dBi. The theoretical Wheeler-Chu-McLean limit for the gain of a $\lambda_0/35 \times \lambda_0/35$ electrically small antenna with a similar Q factor is -9.6 dBi.

CHAPTER 2

A Self-Aligned Fabrication Process for Capacitive Fixed-Fixed Beam RF MEMS Components

2.1 Introduction

The introduction of the self-aligned polysilicon gate [41] and the self-aligned titanium silicide process, which silicides the source and drain regions as well as the polysilicon gate simultaneously [42], allowed for further scaling of complementary metal oxide semiconductor (CMOS) transistors [43]. In addition, the self-aligned polysilicon gate and self-aligned silicidation, or salicidation, fabrication process reduced cost by lowering the number of necessary lithography steps. In imitation of the salicide fabrication process, this paper proposes a self-aligned fabrication process for capacitive fixed-fixed beam RF MEMS components based on self-aligned dielectric and sacrificial spacer. Anno 2008, the market potential of RF MEMS is still limited by cost, packaging and reliability issues [44]. The self-aligned fabrication process reduces the number of processing steps by 40% compared with a conventional RF MEMS fabrication process. In addition, scaling of RF MEMS components offers the potential of reliable sub-microsecond switching [45, 46].

Electrostatically actuated RF MEMS components are commonly classified by contact mechanism - i.e. ohmic versus capacitive, and by anchor mechanism - i.e. cantilever beam versus fixed-fixed beam [3, 11]. Capacitive fixed-fixed beam RF MEMS components are further classified by capacitance ratio, which is the ratio of the down-state capacitance and the up-state capacitance. Capacitive fixed-fixed beam RF MEMS switches have a capacitance ratio in excess of 30, and are used in routing applications. RF MEMS switched capacitors have a capacitance ratio of 2 to 10, and the capacitance of RF MEMS varactors

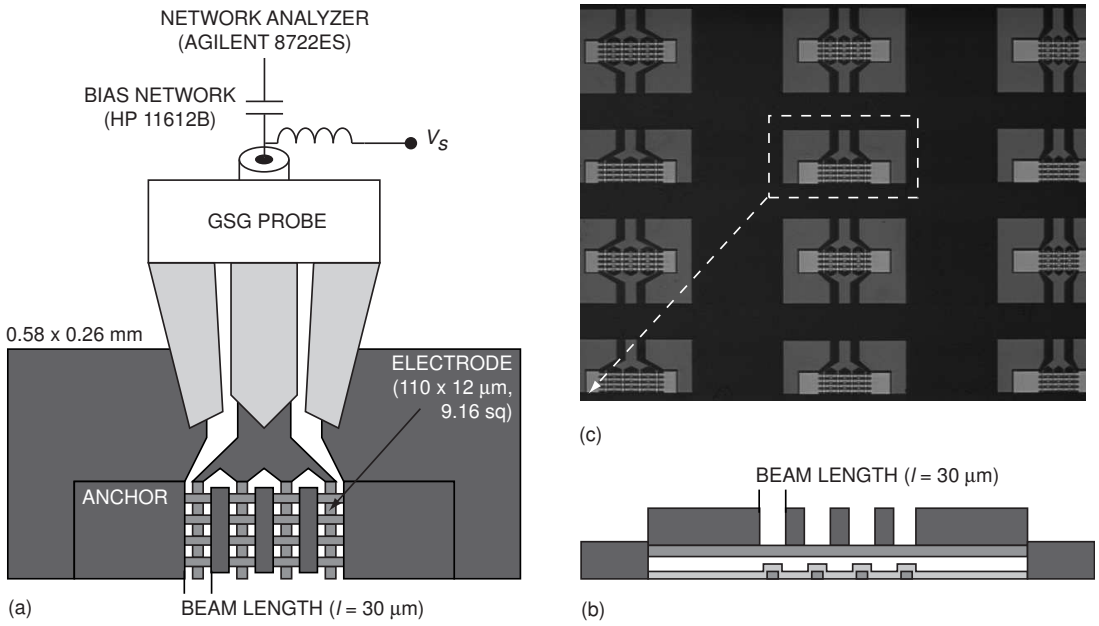

Figure 2.1: Top view (a), cross section (b), and wafer imagery before anchor layer deposition (c) of the 4 by 4 RF MEMS varactor bank.

can be tuned to 120% of its up-state value. Both components are used to tune device characteristics. Applications of capacitive fixed-fixed beam RF MEMS components include phase shifters [31, 32, 33], tunable antennas, filters [47], matching networks [39, 48] and resonators for voltage-controlled oscillators. Table A.1 summarizes the characteristics of state-of-the-art fabrication processes for capacitive RF MEMS components [4, 30, 49, 50, 45, 46].

2.2 Design

In order to maintain a functional reactance for circuit design at 20 GHz, a 4 by 4 RF MEMS varactor bank is designed, comprising 16 scaled fixed-fixed beam RF MEMS varactors, connected in parallel and fed by a 4-way coplanar waveguide (CPW) power divider, as shown in Fig. 2.1. The 4 by 4 RF MEMS capacitor bank is fed through a 50 Ω CPW with 35/60/35 μm dimensions, and fabricated on a high-resistivity silicon wafer (ϵ_r = 11.9, h = 500 μm, $\tan\delta$ = 0.006), which is covered with 1.5 μm of silicon oxide (ϵ_r = 4.1, $\tan\delta$ = 0.0017).

Dimensions and design parameters of an RF MEMS varactor with 30 micron beam

Table 2.1: Comparison of fabrication processes for capacitive fixed-fixed beam RF MEMS components (unmeasured quantities are denoted with -)

	Goldsmith, et al. 1994, [4]	Barker, et al. 2000, [30, 45]	Goldsmith, et al. 2002, [49]	Lacroix, et al. 2007, [46]	This work
Beam dimensions	300 x 120 μm^2	300 x 80 μm^2	300 x 120 μm^2	40 x 10 μm^2	30 x 12 μm^2
Dielectric / beam material	SiN/Al	SiN/Au	Air/Al	Al_2O_3/Al	SiN/Au
Number of masks	5	5	5	7	3
Capacitance ratio	70-100	1.25-1.3	10-30	2.3	1.15
Power handling	4 W (Cold) / 0.5 W (Hot) [51]	0.5 W (Cold)	0.5 W (Hot)	-	200 mW (Cold)
Q factor	-	30 @ 10 GHz	-	20 @ 20 GHz	14.5 @ 20 GHz
Reliability (cycles)	10 B	-	$>$ 100 B	14 B	-
R_s	0.2-0.25 Ω	-	0.2-0.25 Ω	7 Ω @ 20 GHz	3.1 Ω @ 20 GHz
Switching time	$<$ 20 μs	-	$<$ 20 μs	0.15 - 0.4 μs	-

length, are given in Table 2.2. The center-pulled fixed-fixed beam RF MEMS varactors have an up-state capacitance, C_u, of 7.0 fF. The value is hand-calculated using (2.1),

$$C_u = 1.4\frac{\epsilon_0 A}{g_0 + t_d/\epsilon_d}, \tag{2.1}$$

in which $A = W w$. The up-state capacitance, C_u, as a rule-of-thumb, is assumed to be 40% larger than the parallel plate value due to fringing fields [3]. The beam's spring constant, k, is 89.9 N/m using (2.2),

$$k = 32 E w \left(\frac{t}{l}\right)^3 \left(\frac{27}{49}\right) + 8\sigma (1-\nu) w \frac{t}{l}\left(\frac{3}{5}\right) \tag{2.2}$$

in which E, ν, and σ are the Young's modulus, the Poisson ratio and the residual stress respectively of the golden beam. The pull-in voltage, V_p, is the bias voltage for which beam buckling occurs, and is hand-calculated to be 31.2 V using (2.3),

$$V_p = \sqrt{\frac{8 k (g_0 + t_d/\epsilon_d)^3}{27 \epsilon_0 A}}. \tag{2.3}$$

The switching time, t_s, is 354.6 ns using (2.4),

$$t_s = 3.67 \frac{V_p}{V_s \omega_m} = 3.67 \frac{V_p}{V_s \sqrt{k/m}}, \tag{2.4}$$

with ω_m the mechanical resonant frequency, $m = 0.4 \rho l w t$ the effective mass of the beam and V_s the driving voltage. The simulated S-parameters, as well as capacitance and Q factor, will be discussed in the Measurement section.

2.3 Fabrication

Fabrication processes based on surface micro-machining techniques [52, 53, 54, 55], in general, can be realized on any polished dielectric or high-resistivity semiconductor substrate. Conventional fabrication processes for center-pulled capacitive fixed-fixed beam RF MEMS switches, switched capacitors and varactors, as described in [5, 30, 3, 32, 45], require at least 5 masks. The proposed self-aligned fabrication process requires only 3 masks and

[1]The Young's modulus, E, the Poisson ratio, ν, and the mass density, ρ, of gold are: 78 GPa, 0.44 and 19.3 g/cm^3 respectively. The resistivity of gold is 2.44 $\mu\Omega$ cm and the resistivity of aluminum is 2.65 $\mu\Omega$ cm.

[2]The residual stress is calculated as a plug in (2.3). A-posteriori knowledge of V_p, allows for estimation of σ.

Table 2.2: Simulated parameters of the center-pulled fixed-fixed beam RF MEMS varactor

Parameter	Value	Parameter	Value
Air Gap, g_0	0.4 μm	Dielectric Thickness, t_d	2000 Å
Beam Holes	No	Drive Voltage, V_s	50 V
Beam Length, l	30 μm	Electrode Area, A	240 μm^2
Beam Material[1]	Au	Electrode Width, W	12 μm
Beam Thickness, t	3000 Å	Residual Stress[2], σ	100 MPa
Beam Width, w	20 μm		
Effective Mass, m	1.4 pkg	Spring Constant, k	89.9 N/m
Mech. Res. Freq., f_m	1.3 MHz	Switching Time, t_s	354.6 ns
Pull-In Voltage, V_p	31.2 V	Up-State Capacitance, C_u	7.0 fF

approximately 40% fewer processing steps. The three masks are used for definition of the electrodes, the beams and the anchors of the capacitive fixed-fixed beam RF MEMS components. Both fabrication processes allow for monolithic construction of air bridges, integrated thin film resistors and metal-insulator-air-metal capacitors as well. The two aforementioned fabrication processes are compared below.

2.3.1 Conventional Fabrication Process

The conventional fabrication process is illustrated in Fig. 2.2(a). It consists of the following steps:

1. The electrode layer is defined through a wet back-etch of a 100/2000/100 Å thick film of evaporated Ti/Au/Ti.

2. The dielectric layer, used to insulate the electrode, is defined through a buffered hydrofluoric acid (BHF) back-etch process of a 2000 Å thick film of plasma enhanced chemical vapor deposition (PECVD) silicon nitride with a dielectric constant of 7.6. At 380° C, the PECVD is the highest temperature process step. The breakdown voltage of PECVD silicon nitride is 50 V/kÅ.

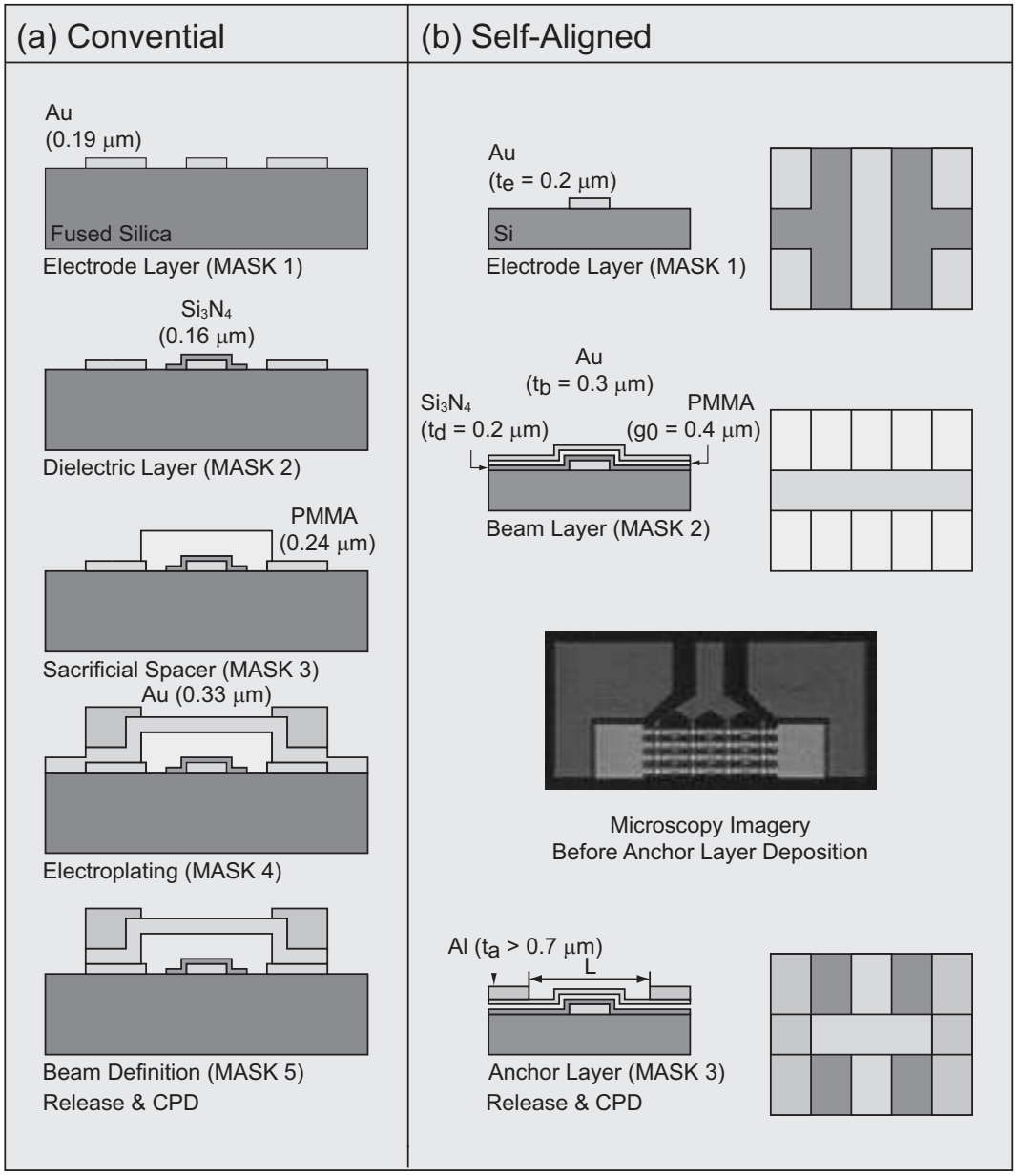

Figure 2.2: Comparison of the conventional and self-aligned RF MEMS fabrication process.

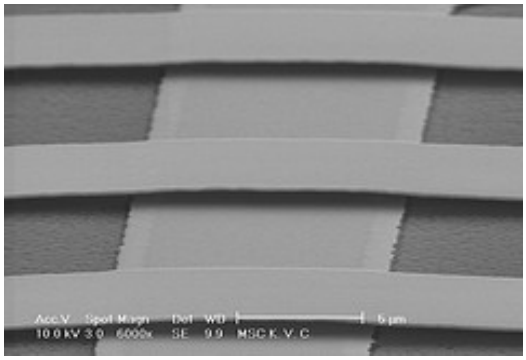

(a) Beams of RF MEMS varactors

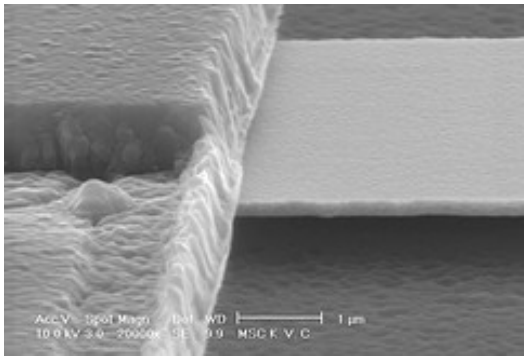

(b) Anchor of an RF MEMS varactor

Figure 2.3: SEM imagery

3. The sacrificial spacer is defined through a back-etch of a 2 μm thick film of spin coated Microchem 950PMMA A9. The reactive ion etcher (RIE) is used for the back-etch, using a 500 Å thick on-wafer mask of evaporated Ti. The major advantage of PMMA as a sacrificial spacer over conventional photo resists is that it reflows conformally after spin coating, making the beams flatter and avoiding mechanical failure due to vertical steps.

4. A 100/8000/500 Å thick film of Ti/Au/Ti is sputtered over the entire wafer and used as a seed layer to selectively plate > 1.5 μm of gold on top of the device. The purpose of the gold electroplating is threefold. Firstly, the anchors of the RF MEMS beams are reinforced, which ensures beam flatness after release. Secondly, electroplating makes the air bridge and the top electrodes of the metal-insulator-air-metal capacitors stiffer, and prevents them from pulling in when a bias voltage is applied. Thirdly, the metal thickness is increased, which reduces conduction losses.

5. The beams are defined through a trifluoroacetic acid (TFA) back-etch of the seed layer. The sacrificial spacer is desolved overnight in hot PRS-2000 solution, and the wafer is dried in a critical point dryer (CPD), which is necessary to prevent the beams from becoming stuck in the down-state.

2.3.2 Self-Aligned Fabrication Process

The self-aligned fabrication process is illustrated in Fig. 2.2(b). It consists of the following steps:

1. The electrode layer is defined through a wet back-etch process of a 100/2000/100 Å thick layer of evaporated Ti/Au/Ti. The RF sheet resistance of a 2000 Å film of gold is 0.138 Ω/sq at 10 GHz and 0.145 Ω/sq at 20 GHz. The entire wafer is subsequently covered with two layers which are not patterned: a dielectric layer and a sacrificial layer. The dielectric layer is deposited during a plasma enhanced chemical vapor deposition (PECVD) process at 380° C. The material is silicon nitride with a dielectric constant of 7.6 and a thickness of 2000 Å. The sacrificial layer is Microchem 950PMMA A4 (polymethylmethacrylate) with a thickness of 0.4 μm.

2. The beam layer is defined using a wet back-etch process of a 500/3000/100 Å thick layer of evaporated Ti/Au/Ti. The golden beams are now used as an on-wafer self-aligned mask for back-etching of the PMMA sacrificial layer and the silicon nitride dielectric using reactive ion etching (RIE) and undiluted BHF, respectively. The back etch process leaves the beams resting on a pillow of PMMA and silicon nitride, disconnected from the electrode layer.

3. The anchor layer is defined through a lift-off process of a 7000 Å thick layer of evaporated aluminum. The purpose of the anchor layer is threefold. Firstly, the anchors connect the beams to CPW ground strips. Secondly, the anchor layer makes air bridges and the top electrodes of the metal-insulator-air-metal capacitors stiffer, and prevents them from pulling in when a bias voltage is applied. Thirdly, the metal thickness of the CPW is increased which reduces ohmic losses. The RF sheet resistance of a 0.7 μm film of aluminum is 0.0563 Ω/sq at 10 GHz and 0.0652 Ω/sq at 20 GHz.

   The thickness of the anchor layer is kept minimal in order not to strain the lift-off process which uses Shipley 1827 photo resist. The minimal thickness of the anchor layer, t_a, able to connect the beams to the CPW, is calculated using the expression below:

$$t_a = t_d + g_0 + t_b - t_e \tag{2.5}$$

   Increasing the electrode layer thickness, t_e, beyond 2000 Å would reduce the line loss and increase the Q factor, but would require a sacrificial spacer with better step coverage than 950PMMA A4[1]. The air gap, g_0, is limited by the lift-off process

[1]Note that chemical mechanical polishing (CMP) can not be used on resists.

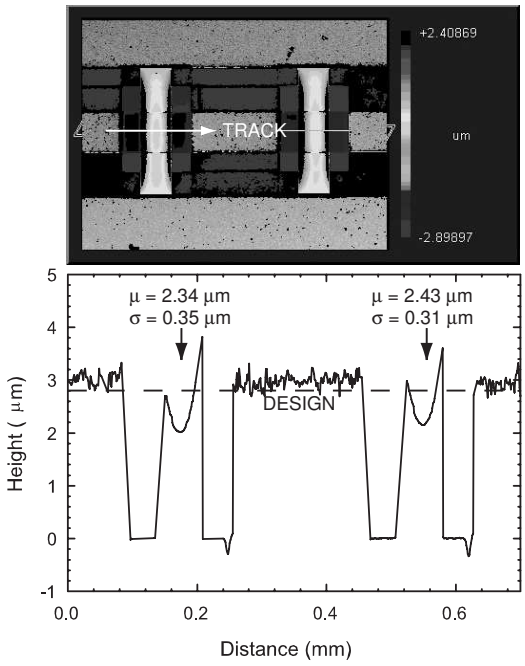

Figure 2.4: Optical interferometry imagery (top) and surface profile (bottom) of RF MEMS components fabricated using the conventional fabrication process. The mean and standard deviation of the transverse beam profile are shown.

defining the anchors, and can be increased using lift-off processes based on bilayer photo resists, thereby extending the use of the self-aligned fabrication process to RF MEMS switches with a high capacitance ratio, or to applications where line loss is to be minimized.

Soaking the wafer in hot Baker PRS-2000 solution not only lifts off the unnecessary parts of aluminum, but at the same time releases the beams because the PMMA sacrificial layer is desolved as well. Scanning electron microscopy (SEM) is used to verify that the beams are in up-state, as shown in Fig. 2.3.

2.3.3 Comparison

The advantages of the self-aligned RF MEMS fabrication process are:

- The self-aligned fabrication process reduces the number of lithography steps necessary; only three masks are used compared with five for a conventional RF MEMS fabrication process. The use of an on-wafer self-aligned mask for patterning of the sacrificial spacer

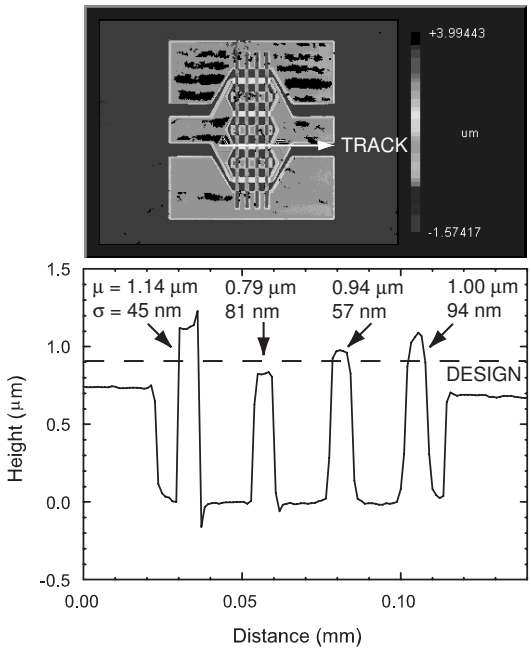

Figure 2.5: Optical interferometry imagery (top) and surface profile (bottom) of RF MEMS components fabricated using the self-aligned fabrication process. The mean and standard deviation of the transverse beam profile are shown.

and dielectric layer reduces the amount of alignment errors and thereby allows for a significant scaling of the beam length.

- The self-aligned fabrication process allows for flatter beams. In contrast to the conventional fabrication process, it prevents a BHF wet etch, or an RIE, from etching out part of the substrate during definition of the dielectric. The beams are longitudinally flatter because they track a flatter topology. In addition, the self-aligned fabrication process allows a stacked beam layer deposition using evaporation, whereas the conventional fabrication process requires a conformal beam layer deposition using sputtering. Evaporation yields beams with lower residual stress, which are transversely flatter. Optical interferometry surface profiles of RF MEMS components fabricated using the conventional fabrication process, as shown in Fig. 2.4, and using the self-aligned fabrication process, as shown in Fig. 2.5, confirm the claims. The standard deviation of the self-aligned transverse beam profiles is 69 nm on average, whereas the standard deviation of the conventional transverse beam profiles is 0.33 μm on average. It is also observed that the conventional fabrication process yields an average air gap which

is lower than the design value, whereas the self-aligned fabrication process yields an average air gap which is higher than the design value.

- The self-aligned fabrication process allows a broad selection of the materials because it is not tied to electroplated Ti/Au/Ti stacks, which are incompatible with aluminum and ultra-nanocrystalline diamond (UNCD) films [56]. Aluminum has a higher stiffness versus mass ratio, and would yield faster components when used as a beam material. However, as indicated in Table A.1, there are examples of 5-mask fabrication processes based on a W/SiN/Al stack. UNCD possesses a stable low stiction surface chemistry, and would yield more reliable components when used as a dielectric material [57].

A disadvantage of the self-aligned fabrication process is the increased vulnerability to over-etching. An over-etched beam will lead to an over-etched sacrificial spacer and dielectric.

2.4 Measurements

Measurements show that the 4 by 4 RF MEMS varactor bank - henceforth referred to as device under test (DUT), is functional and that the RF performance is comparable with the work discussed in [45, 46].

2.4.1 Biasing

The measured pull-in voltage, V_p, is between 35 and 50 V, which is higher than the design value. The DUT is biased using a bipolar drive voltage, V_s, in order to avoid dielectric charging and to increase the lifetime of the device. V_s is kept below 35 V, in order not to damage the HP 11612B bias network and the Agilent 8722ES network analyzer. As such, the DUT operation is limited to the varactor mode ($V_s < V_p$).

2.4.2 S-Parameters

The one-port S-parameters of the up-state and the biased state of DUTs with beam lengths of 30 and 45 μm, are measured and compared with method of moments simulation results in Fig. 2.6. One-port S-parameters of the open-ended transmission line test

structures without beams are measured and simulated as well, in order to discriminate between the capacitance and loss of the open-ended transmission line test structures and the capacitance and loss of the RF MEMS varactors. The difference in capacitance for the up-state (133.9 fF) is close to $16 \times C_u$ (112 fF), with C_u being the analytically predicted up-state capacitance of a single scaled RF MEMS varactor, as discussed in the design section. Capacitances and Q factors are tabulated in Table 2.3.

The Q factor, which includes losses incurred in the 4-way power divider and transmission lines, limits the applicability of the DUT. It is obtained using the S-parameter method, as discussed in [3],

$$Q_l = \frac{1}{\omega\, R_s\, C_s} = \frac{|X_s|}{R_s} = \frac{2\,|\Im(S_{11})|}{1\,-\,|S_{11}|^2}, \tag{2.6}$$

in which the DUT is modelled as a lossy capacitor at every frequency - i.e. a capacitor C_s in series with a resistor R_s, yielding an input impedance $Z_{IN} = R_s + j\,X_s = R_s + \frac{1}{j\,\omega\,C_s}$. At 20 GHz, the measured C_s ranges between 180.5 and 199.2 fF (-j44 Ω $< jX_s <$ -j40 Ω) for the DUT with 30 μm beam lengths and between 190.7 and 210.3 fF for the DUT with 45 μm beam lengths. The measured Q factor ranges between 14.5 and 10.8 for the DUT with 30 μm beam lengths and between 25.1 and 11.6 for the DUT with 45 μm beam lengths.

The series resistance, R_s, which adversely affects the Q factor, is mainly due to the resistance of the electrodes. The electrode layer is the thinnest layer in the material stack. As stated in the Fabrication section, the RF sheet resistance of the 2000 Å thick golden electrodes is 0.138 Ω/sq at 10 GHz and 0.145 Ω/sq at 20 GHz. The resistance of the electrodes, consisting of 9.16 squares, is therefore at least 1.27 Ω at 10 GHz and 1.33 Ω at 20 GHz. However, the DUT comprises 16 scaled fixed-fixed beam RF MEMS varactors, connected in parallel and fed by a 4-way CPW power divider. R_s is therefore not only located in the electrode of the RF MEMS varactors. The series capacitance, C_s, affects for example the return loss of the 4-way power divider and the fitted R_s. The S-parameter measurements of the biased state are believed to be perturbed by the HP 11612B bias network and the biasing of a semiconducting substrate, causing a difference in R_s between the up- and biased state.

Table 2.3: Capacitance and Q factor of the transmission line and the DUT (up-state and biased)

SIMULATED							
		T-LINE		UP-STATE		BIASED STATE	
	l (μm)	30	45	30	45	30	45
10 GHz	R_s (Ω)	2.05	2.05	1.5	1.6	1.5	1.6
	X_s (Ω)	-286.2	-278.4	-126.9	-112.8	-109.5	-95.7
	C_s (fF)	55.6	57.2	125.5	141.2	145.5	166.4
	Q	139.6	135.8	84.6	70.5	73.0	59.8
20 GHz	R_s (Ω)	1.5	1.6	1.6	1.7	1.65	1.8
	X_s (Ω)	-139.7	-135.6	-58.4	-50.8	-49.45	-42
	C_s (fF)	57.0	58.7	136.3	156.7	161.0	189.6
	Q	93.1	84.8	36.5	29.9	30.0	23.3
MEASURED							
		T-LINE		UP-STATE		BIASED STATE	
	l (μm)	30	45	30	45	30	45
10 GHz	R_s (Ω)	8.2	11.1	4.7	2.5	10.7	8.7
	X_s (Ω)	-287.8	-274.6	-99.9	-95.6	-90.6	-87.4
	C_s (fF)	55.3	58.0	159.3	166.5	175.8	182.2
	Q	35.0	24.7	21.4	38.5	8.5	10.0
20 GHz	R_s (Ω)	4.5	7.2	3.1	1.7	3.7	3.3
	X_s (Ω)	-140.1	-134.0	-44.1	-41.8	-40.0	-37.9
	C_s (fF)	56.8	59.4	180.5	190.7	199.2	210.3
	Q	31.1	18.7	14.5	25.1	10.8	11.6

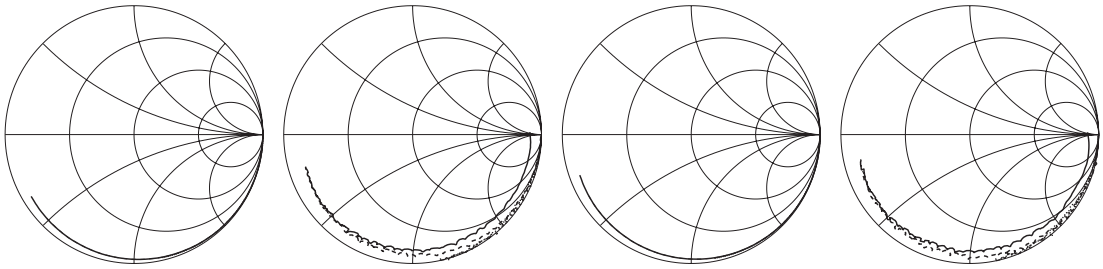

(a) l = 30 μm - Simulated (b) l = 30 μm - Measured (c) l = 45 μm - Simulated (d) l = 45 μm - Measured

Figure 2.6: S_{11} Smith charts of the up-state (solid), the biased state (dashed), and the test structure (dotted) from 0.05 to 40 GHz

2.4.3 Power Handling

The power handling of capacitive fixed-fixed beam RF MEMS components is discussed in [51]. Self-actuation and electromigration are the primary causes of failure under cold-switched high-power operation. Self-actuation occurs when the root mean square (RMS) of the RF voltage across electrode and beam, V_{RMS}, exceeds the pull-in voltage, V_p. Electromigration occurs when the RMS of the RF current density through the golden beam, J_{RMS}, exceeds 0.5 MA/cm^2 [58] and rips loose atoms out of the conductor lattice.

The cold-switched power handling of the DUT is measured by placing a Hughes 1177H X-band travelling-wave tube (TWT) power amplifier in between the network analyzer, operating in CW mode, and the DUT. Due to the high pull-in voltage of the DUT, it is limited by electromigration. An established method for characterizing electromigration is the median-time-to-failure measurement [59], in which the median duration is recorded before a metallic thin film line fails to conduct a controlled current density at a controlled temperature. Likewise, the cold-switched power handling of the DUT is verified up to 200 mW at 10 GHz with no electromigration observed after 10 min. At 500 mW, however, the anchors of some DUTs delaminated instantaneously causing irreversible damage.

2.5 Conclusion

A self-aligned fabrication process for capacitive fixed-fixed beam RF MEMS components is disclosed. RF MEMS varactors with a beam length of 30 μm are demonstrated and the RF performance of a 4 by 4 RF MEMS varactor bank is comparable with state-of-the-art

results for capacitive RF MEMS components with beam lengths smaller than 50 μm.

Acknowledgements

Dr. Denis Mercier is thanked for helping out with the SEM imagery. Prof. Jack East is thanked for lending the Hughes 1177H X-band TWT power amplifier. Fabrication of the scaled capacitive fixed-fixed beam RF MEMS components was done in the Michigan Nanofabrication Facility (MNF).

CHAPTER 3

A 2-Bit Ka-Band RF MEMS Frequency Tunable Slot Antenna

3.1 Introduction

Frequency tunability is of interest in software-defined radios, which require a programmable modem and RF front-end, in order to tune to a multitude of frequency bands. Antenna tunability is usually achieved by incorporation of lumped components based on III-V semiconductor technology, such as single pole single throw (SPST) switches or varactor diodes. However, these components can be readily substituted for RF MEMS switches and varactors in order to take advantage of the low insertion loss and high Q factor offered by RF MEMS technology [3]. In addition, RF MEMS components can be integrated monolithically on low-loss dielectric substrates, such as borosilicate glass (ϵ_r = 5.1, $\tan\delta$ = 0.006), fused silica (ϵ_r = 3.78, $\tan\delta$ = 0.0002) or liquid crystal polymer (LCP), whereas III-V semiconducting substrates are generally lossy and have a high dielectric constant. A low loss tangent and low dielectric constant are of importance for the efficiency and the bandwidth of the antenna.

The prior art includes an RF MEMS frequency tunable fractal antenna for the 0.1-6 GHz frequency band [18], an RF MEMS frequency tunable slot antenna for the 2.4-4.6 GHz band [19], an RF MEMS radiation pattern reconfigurable spiral antenna for 6 and 10 GHz [20], an RF MEMS radiation pattern reconfigurable spiral antenna for the 6-7 GHz frequency band based on packaged Radant MEMS SPST-RMSW100 switches [21], and an RF MEMS Sierpinski multiband fractal antenna for 2.4 and 18 GHz [22].

In this chapter, design and measurement of a 2-bit Ka-band RF MEMS frequency tun-

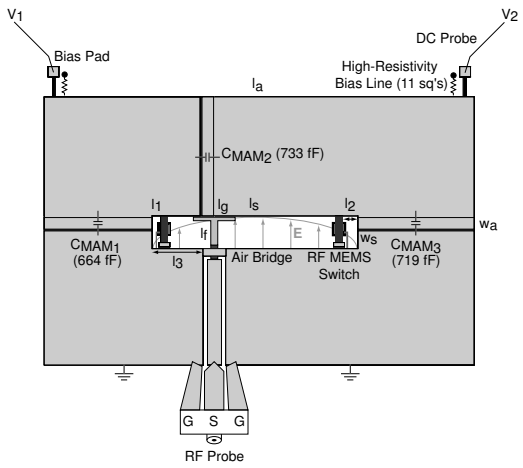

Figure 3.1: The 2-bit Ka-band RF MEMS frequency tunable slot antenna

able slot antenna, shown in Fig. 3.1, are discussed. The uniplanar slot antenna, fed through a coplanar waveguide (CPW), is amenable to micro-fabrication techniques which allow monolithic integration of air bridges, metal-air-metal capacitors and center-pulled capacitive fixed-fixed beam RF MEMS switches, as shown in Fig. 3.2. The RF MEMS switches shorten the electrical length of the resonant slot when actuated, increasing the radiation frequency.

3.2 Design

The 2-bit Ka-band RF MEMS frequency tunable slot antenna is fabricated on a 500 μm thick fused silica wafer. The slot width is 0.37 mm and the slot length is 2.3 mm. The input impedance of a center-fed slot antenna is 550-700 Ω at first resonance. In order to match the input impedance, the slot antenna is fed off-center through a capacitively coupled 20/150/20 μm CPW. Dimensions, as defined in Fig. 3.1, are given in Table 3.1.

The ground plane of the antenna is divided into three bodies using large metal-air-metal DC caps to allow for independent biasing of the two RF MEMS switches. The metal-air-metal capacitors have capacitance values between 660 and 730 fF, which are rather low, even at Ka-band, and cannot be disregarded during full-wave simulations. The electrodes of the RF MEMS switches are connected to the lower half of the ground plane, which is grounded upon RF probing. The beams of the RF MEMS switches connect to the two

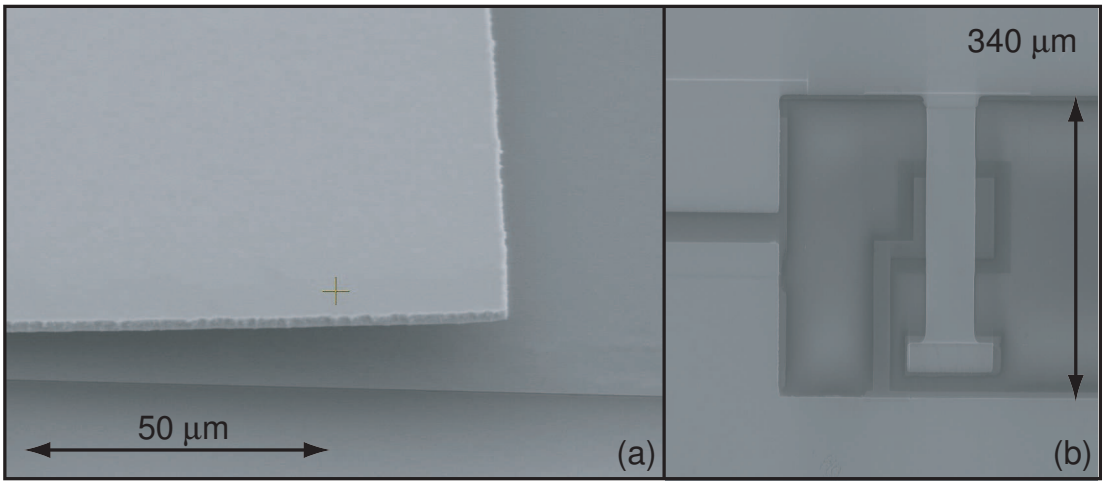

Figure 3.2: SEM imagery of a metal-air-metal capacitor (a) and a center-pulled capacitive fixed-fixed beam RF MEMS switch (b)

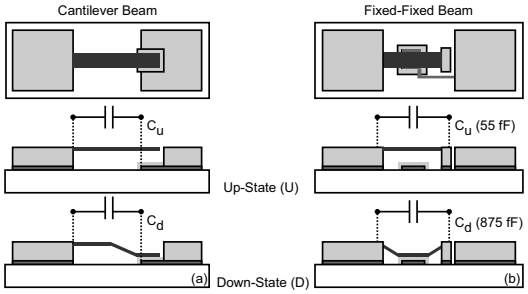

Figure 3.3: Capacitive RF MEMS switches for slot lines: cantilever beam (a) versus fixed-fixed beam (b)

upper bodies, which are biased using bias pads, connected by high-resistivity bias lines. The bias pads are used to avoid disturbing the current distribution on the ground plane of the antenna.

Electrostatically actuated RF MEMS switches are commonly classified by contact mechanism - i.e. metal-to-metal versus capacitive, or by anchorage - i.e. cantilever beam versus fixed-fixed beam. Capacitive cantilever beam switches are preferred for slot lines because capacitive switches typically outperform their metal-to-metal contact counterparts above X-band and a cantilever anchorage is more amenable to balanced transmission lines, as shown in Fig. 3.3. The choice for capacitive fixed-fixed beam type stems from the fact that a mature fabrication process with high wafer yield has been demonstrated at the Michigan

Table 3.1: Dimensions of the 2-bit Ka-band RF MEMS frequency tunable slot antenna, as shown in Fig. 3.1

Parameter	Value	Parameter	Value
Antenna Length, l_a	4.8 mm	Offset Length 1, l_1	0.1 mm
Antenna Width, w_a	3 mm	Offset Length 2, l_2	0.605 mm
Feed Length, l_f	0.43 mm	Offset Length 3, l_3	0.17 mm
Feed Width, w_f	0.05 mm	Slot Length, l_s	2.3 mm
Gap Length, l_g	0.5 mm	Slot Width, w_s	0.37 mm
Gap Width, w_g	0.02 mm		

Nanofabrication Facility [3]. However, capacitive fixed-fixed beam RF MEMS switches can be used successfully across slot lines whenever the beams span most of the slot width, and the disconnected anchor is placed as close as possible to the edge of the slot line without shorting it.

Dimensions and design parameters of the center-pulled capacitive fixed-fixed beam RF MEMS switches are tabulated in Table 3.2. Expressions for the up- and down-state capacitance, the pull-in voltage, V_p, the spring constant, k, and the switching time, t_s, can be found in [3]. The finite Q factor of the RF MEMS switches bounds the gain of the loaded slot antenna. The Q factor is obtained using the S-parameter method [3]. A one-port method of moments simulation of the center-pulled fixed-fixed beam RF MEMS switch layout for slot lines is performed, as shown in Fig. 3.4(a), taking into account the finite conductivity of the metal films. The Q factor is calculated using (3.1),

$$Q = \frac{1}{2\,\pi\,f\,R\,C_u} = \frac{2\,|\Im(S_{11})|}{1\,-\,|S_{11}|^2}, \tag{3.1}$$

where R is the parasitic resistance of the RF MEMS switch. The calculated Q factor, as shown in Fig. 3.4(b), is between 18.7 and 11[1] and is rather low, mainly due to the layout of the electrode. The electrode is a 2000 Å thick film of evaporated gold and the RF sheet resistance, R_s, of a 2000 Å thick gold film is 0.149 Ω/sq at 26.5 GHz and 0.156 Ω/sq at 40

[1]No attempts have been made to de-embed the transmission line loss from the one-port simulation. As such, the stated Q factor slightly understates the Q factor of the center-pulled fixed-fixed beam RF MEMS switch layout for slot lines.

Table 3.2: Simulated parameters of the center-pulled capacitive fixed-fixed beam RF MEMS switch

Parameter	Value	Parameter	Value
Air Gap, g_0	1.75 μm	Dielectric Thickness, t_d	4000 Å
Beam Holes	No	Drive Voltage, V_s	50 V
Beam Length, l	300 μm	Electrode Area, A	8,000 μm^2
Beam Material	Au	Electrode Width, W	100 μm
Beam Thickness, t	8000 Å	Residual Stress, σ	100 MPa
Beam Width, w	80 μm	Unloaded Characteristic Impedance[2], Z_u	152.7-171.5 Ω
Capacitance Ratio, C_R	15.9	Parasitic Resistance[2], R	5.8-6.5 Ω
Down-State Capacitance, C_d	874 fF	Spring Constant, k	66.6 N/m
Effective Mass, m_{eff}	147 pkg	Switching Time, t_s	5.5 μs
Mechanical Resonant Frequency, f_m	108.6 kHz	Q Factor[2]	18.7-11
Pull-In Voltage, V_p	41 V	Up-State Capacitance, C_u	55 fF

GHz, using (3.2).

$$R_s = \frac{\rho}{t}\frac{1}{1-e^{-t/\delta}} \tag{3.2}$$

The RF resistance of the electrode, which consists of 12 squares, is therefore 1.872 Ω at 40 GHz (12 sq's × 0.156 Ω/sq) and adversely affects the Q factor of the RF MEMS switch layout for slot lines. One way to reduce the RF resistance of the electrode is to increase the electrode line width. Doubling the electrode line width results in an electrode area of approximately 6 squares. The additional line loss incurred per RF MEMS switch, α, stated in dB/switch, can be calculated using (3.3),

$$\alpha = 8.686\,\frac{R\,Z_u\,\omega^2\,C_u^2}{2}, \tag{3.3}$$

[2]The parameter is calculated for 26.5-40 GHz.

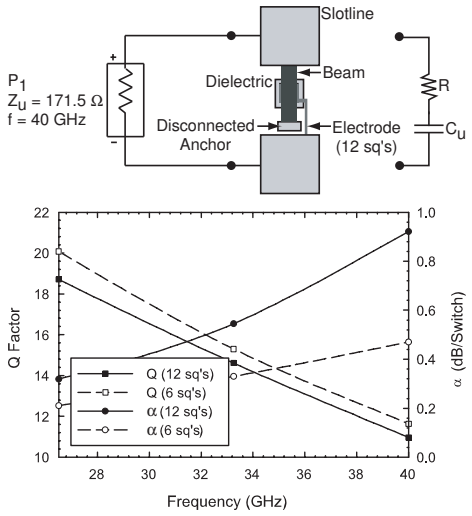

Figure 3.4: One-port method of moments simulation of the center-pulled capacitive fixed-fixed beam RF MEMS switch layout for slot lines (top), calculated Q factor and additional line loss per RF MEMS switch, α (bottom)

where Z_u is the unloaded characteristic impedance of the slot line and the parasitic resistance, R, of the RF MEMS switch is extracted from the calculated Q factor using (3.1). While slot antennas are resonant, the additional line loss incurred per RF MEMS switch, α, as shown in Fig. 3.4, gives an impression of the decrease in gain due to the finite Q factor of the RF MEMS switches.

The placement of the RF MEMS switches simultaneously impacts the input impedance, the instantaneous bandwidth and the resonant frequency of the 4 states. The 4 states are defined by the state of the beams of the two RF MEMS switches, which are up-up (UU) with the lowest resonant frequency, up-down (UD), down-up (DU) or down-down (DD) with the highest resonant frequency. Method of moments simulations include the air bridge, the two bias lines, the three metal-air-metal capacitors, the two RF MEMS switches, and account for the finite conductivity of the metal layers and the finite dimensions of the ground plane. The simulated return loss for each of the 4 states is shown in Fig. 3.5(a)-(d). Trade-offs are to be made in the design process: for example, in Fig. 3.5(a) it is shown that the antenna in the UU state spurs in the DD band, because in the UU state the shorter side of the slot looks shorted at 36 GHz. Increasing capacitive coupling between CPW feed and the slot antenna will reduce the effect. However, decreasing the slit between CPW feed and ground

plane to below 20 μm is challenging from a fabrication perspective. E- and H-plane co- and cross-polarized radiation patterns for each of the 4 states resemble the radiation patterns of an ordinary slot antenna radiating at its dominant mode.

3.3 Measurements

3.3.1 Biasing

The RF MEMS switches are biased using a bipolar drive voltage, V_s, of 45 V in order to avoid dielectric charging and to increase the lifetime of the device. The measured pull-in voltage, V_p is 35-40 V, which is close to the design value.

3.3.2 Return Loss & Gain

Characterization of a 4.8 $\times$ 3 mm^2 antenna under test (AUT) at millimeter-wave frequencies is challenging. The return loss and gain for the 4 states of the actuated AUT, as well as for 4 on-wafer AUTs with the RF MEMS beams in the up- or down-fabricated position depending on the state, henceforth referred to as the *hard-wired* AUTs, are therefore measured using a probe station based setup [60]. The setup eliminates the need for wafer dicing and custom-built test fixtures with coaxial connectors or waveguide flanges. The wafer is placed on a cavity filled with absorber, located in the far field of the AUT, which replaces the probe station wafer chuck, and is probed with a Picoprobe Model 40A-GSG-150-C after a short-open-load (SOL) calibration. The measurement results are shown in Fig. 3.5(a)-(d), and are tabulated in Table 3.3. Discrepancies between simulations and *hard-wired* measurements are attributed to deviations from nominal design parameters and alignment errors during fabrication. Stress induced bow of the top electrode of the metal-air-metal capacitors, as shown in Fig. 3.2, or the RF MEMS beams in up-state, also changes the resonant frequencies. Discrepancies between the *hard-wired* measurements and actuated measurements are attributed primarily to the DC probes cluttering the near field of the actuated AUT, and to deviations in the down-state capacitance, C_d.

Subsequently, a WR-28 standard gain horn is moved along a hemispherical arc in order to measure the gain and the cross-polarization in the principal planes at broadside. Table 3.3 tabulates the measured gain of the *hard-wired* AUTs. The average gain is 1.74 dBi. The average cross-polarization is -9.22 dBi. Discrepancies between the simulated and measured

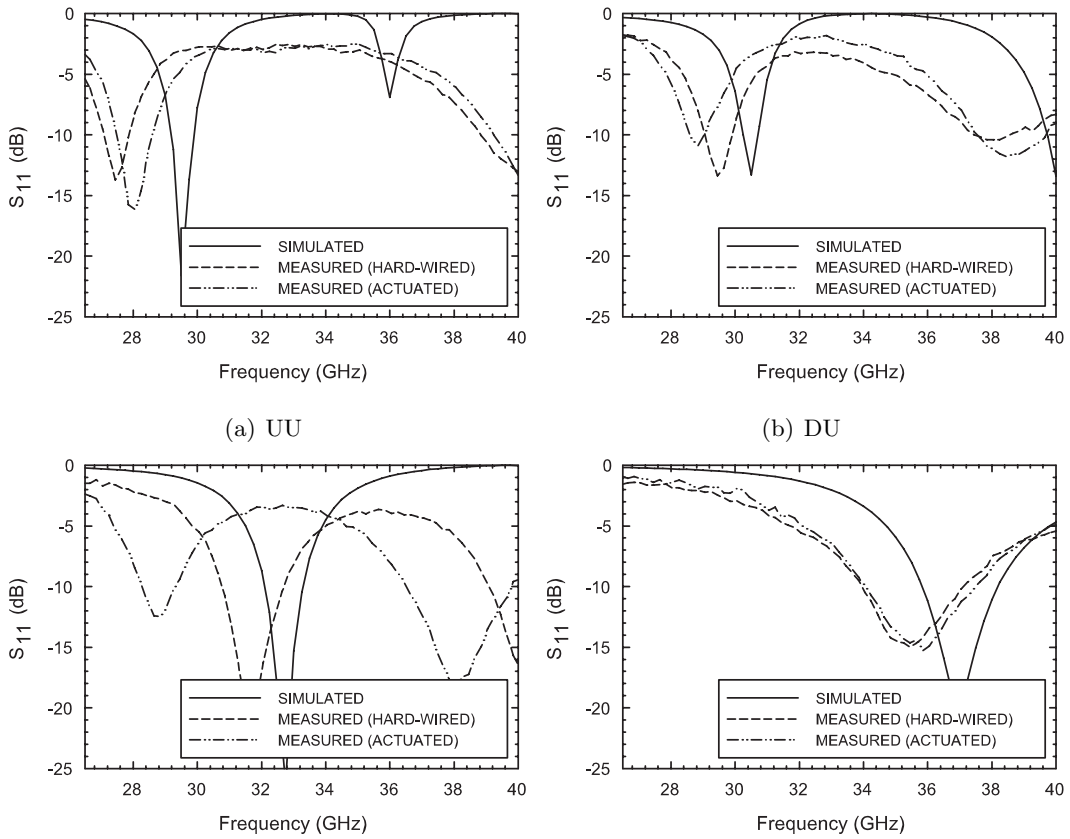

(a) UU (b) DU

(c) UD (d) DD

Figure 3.5: Measured return loss of each of the 4 states of the AUT

gain and cross-polarization are primarily due to measurement errors induced by forward scattering from the RF probe and probe positioner and scattering induced polarization cross-talk, as discussed in [60]. Given the measurement uncertainty, the average, μ_G, and the standard deviation, σ_G, of the gain within an angular window of 10° from broadside in the principal planes are also stated. σ_G is an indicator for the measurement error caused by the frequency-specific cyclic angular variation of the gain due to forward scattering from the RF probes and probe positioner. The gain and cross-polarization of the actuated AUT could not be measured reliably because of the scattering from the DC probes and accompanying probe holders. Taking into account the simulation results and poor repeatability of the actuated AUT measurements, the *hard-wired* return loss and gain measurements most accurately represent those corresponding to the self-impedance of the AUT states.

Table 3.3: Simulated and measured figures of merit for each of the 4 states.

Simulated				
	UU	DU	UD	DD
f_r	29.5 GHz	30.5 GHz	32.75 GHz	37 GHz
BW	0.75 GHz	0.5 GHz	1.25 GHz	2.5 GHz
G	2.3 dBi	2.3 dBi	2.1 dBi	1.8 dBi
e	67.9%	66.3%	67.3%	65.3%
Measured (*hard-wired* AUTs)				
f_r	28 GHz	29.25 GHz	31.5 GHz	35 GHz
BW	0.8 GHz	0.8 GHz	2 GHz	3.2 GHz
G	2.2 dBi	1.3 dBi	-4.33 dBi	7.8 dBi
μ_G	-0.99 dBi	-2.23 dBi	-7.30 dBi	3.38 dBi
σ_G	1.42 dB	0.36 dB	0.01 dB	1.25 dB

3.3.3 Switching Time

The switching time, t_s, of the AUT is measured indirectly through a mechanical measurement of the spring constant, k, of the fixed-fixed beam. An indirect mechanical measurement of t_s avoids measurement perturbation due to the bias electronics and cabling. k is measured with the Veeco Dektak 6M surface profiler which measures step heights on surfaces with a programmable stylus force, F_i. The stylus is moved over the beam along a transversal path, and the displacement, z_i, at the center of the beam is measured for stylus masses, m_i, ranging from 1 mg to 10 mg, as shown in Fig. 3.6. Note that displacement upon probing depends on the distance between the stylus and the gravitational center of the beam, because k is a function of the moment of inertia of the beam. A least squares method is used to fit k, using (3.4), which assumes a static equilibrium between the stylus force and the restoring force exerted by the beam on the stylus.

$$F_i = m_i\, g = k\, z_i \tag{3.4}$$

g is the acceleration due to gravity constant (9.81 N/kg). The fitted value of 58.1 N/m is in good agreement with the simulated value, as stated in Table 3.2. Knowledge of the measured pull-in voltage V_p and k allows for accurate prediction of

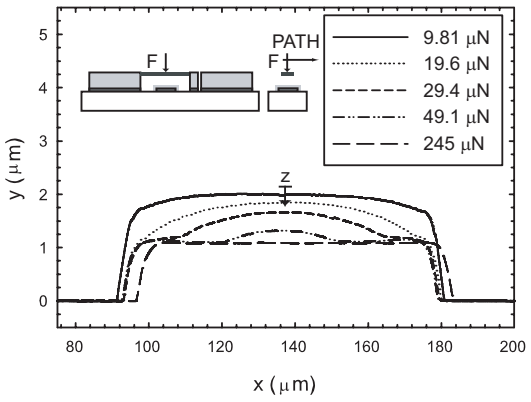

Figure 3.6: Beam displacement versus stylus force

$$t_s = 3.67 \frac{V_p}{V_s \sqrt{k/m_{eff}}}, \tag{3.5}$$

in which $m_{eff} = 0.4\,\rho\,l\,t\,w$ is the effective mass of the beam, yielding 5.19 μs for a drive voltage, V_s, of 45 V.

3.4 Conclusion

A 2-bit Ka-band RF MEMS frequency tunable slot antenna is disclosed.

CHAPTER 4

A High-Power X-Band Differential RF MEMS SPST Switch

This chapter will be released upon acceptance for publication.

CHAPTER 5

An Analog RF MEMS Slotline True Time Delay Phase Shifter

5.1 Introduction

The advent of RF MEMS phase shifters has enabled wide-angle passive electronically scanned arrays with high effective isotropically radiated power (EIRP), also referred to as power-aperture product, and with associated long-range detection capability [34, 35, 36]. In addition, the usage of monopulse comparators and true time delay (TTD) phase shifters results in high angular resolution and high range resolution respectively. Four-quadrant monopulse comparators are the proverbial cross hairs of a fire control radar. They increase the angular accuracy to a fraction of the beamwidth by comparing echoes, which originate from a single pulse and which are received in three concurrent and spatially-orthogonal channels, being the sum channel, Σ, the azimuth-difference channel, Δ_{AZ}, and the elevation-difference channel, Δ_{EL} [14]. TTD refers to the invariance of time delay with frequency, or equivalently, to the linear phase shift with frequency. Usage of TTD components allows ultra wideband (UWB) radar waveforms with associated high range resolution, and avoids beam squinting or frequency scanning.

TTD phase shifter are designed using the switched-line principle [25, 26, 27] or the distributed loaded-line principle [28, 29, 30, 3, 31, 32, 33]. Switched-line TTD phase shifters are superior to distributed loaded-line TTD phase shifters in terms of time delay per decibel noise figure (NF), especially at frequencies up to X-band, but are inherently digital and require low-loss and high-isolation single pole N throw (SPNT) switches. Distributed loaded-line TTD phase shifters, however, can be realized analogously or digitally, and in

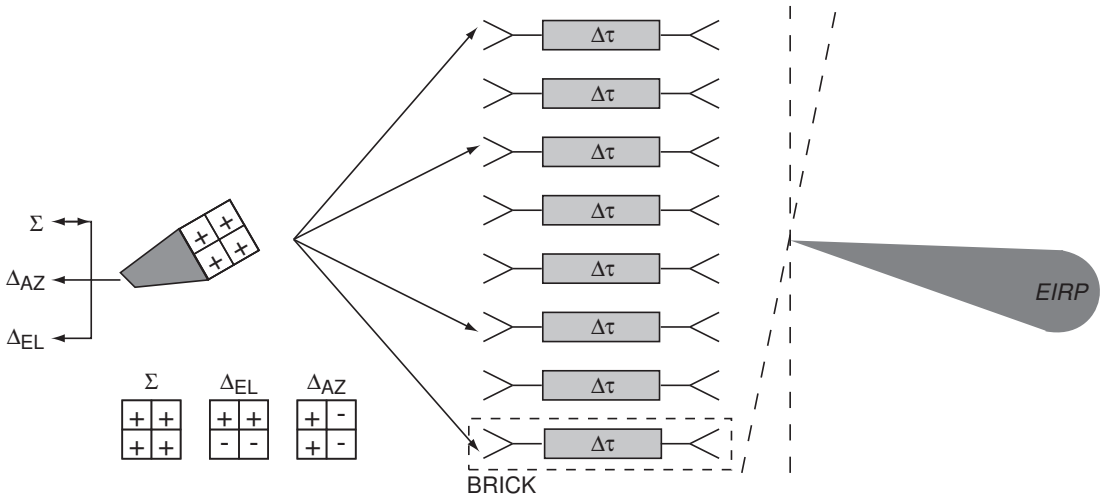

(a) A time-delaying lens is illuminated by a four-quadrant monopulse horn. EIRP denotes effectively isotropically radiated power.

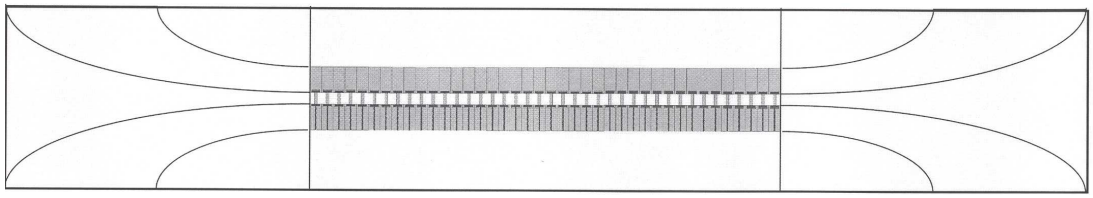

(b) UWB brick (double exponentially tapered slot antenna - slotline TTD phase shifter - double exponentially tapered slot antenna)

Figure 5.1: Envisioned application of the analog RF MEMS slotline TTD phase shifter

smaller form factors, which is important at the subarray level. Analog phase shifters are biased through a single bias line, whereas multi-bit digital phase shifters require a parallel bus along with complex routing schemes at the subarray level. In addition, usage of an analog bias voltage avoids large phase quantization errors which deteriorate the effective isotropically radiated power and beam pointing accuracy, and elevate the sidelobe level of an electronically scanned array [16, 15].

In this chapter, an analog RF MEMS slotline TTD phase shifter is presented, which is developed for a brick-assembled time-delaying lens in which each brick comprises a tapered slot antenna followed by an RF MEMS slotline TTD phase shifter followed by a tapered slot antenna, as shown in Fig. 5.1. Brick assembly refers to the microwave circuitry being integrated perpendicularly to the array plane, and is most often implemented using metal housings and racks. Tile assembly, on the contrary, refers to the microwave circuitry being integrated parallelly to the array plane, and is most often implemented using multi-layer

laminates. From an electronically scanned array perspective, the usage of the RF MEMS slotline TTD phase shifter in the proposed brick design yields several advantages over tile designs [61], such as:

- **Antenna selection:** The RF MEMS slotline TTD phase shifter can be cascaded to tapered slot antennas, such as the Vivaldi aerial or the double exponentially tapered slot antenna [62, 63, 64, 65], obviating lossy and resonant baluns, impedance transformers and mode transitions.
- **Bandwidth:** The brick design allows for UWB beam steering.
- **EIRP:** The RF MEMS slotline TTD phase shifter has a lower phase shift versus decibel NF, but a higher V_{RMS}-limited power handling compared with its coplanar waveguide (CPW) counterpart.
- **Fabrication:** The brick design is uniplanar and allows for monolithic integration of the RF MEMS slotline TTD phase shifter and efficient tapered slot antennas on fused silica or borosilicate glass wafers or liquid crystal polymer (LCP) flexible substrates [66], which are the substrates of choice for high-Q RF MEMS fabrication. The uniplanar monolithic integration obviates microvia technology and does not deteriorate the scan performance because the RF MEMS TTD phase shifters are not lying in the radiating half-space of the end-fire radiating tapered slot antennas.
- **Feed network:** The space-fed time delaying lens can be illuminated with a four-quadrant monopulse horn.
- **Scalability:** The brick assembly is 2D scalable and can be made polarimetric.

5.2 Design

An RF MEMS distributed loaded-line TTD phase shifter consists of a high impedance transmission line, which is periodically loaded with capacitive fixed-fixed beam RF MEMS switches used as varactors (biased up to 90% of their pull-in voltage, air gap, g_0, reduction to 2/3 of its nominal value). The increase in distributed capacitance with bias voltage provides a progressive phase shift with respect to the transmission phase in the unbiased state. A limitation of capacitive loading is the achievable phase shift per decibel NF in the light of

Table 5.1: Comparison of distributed loaded-line TTD phase shifters

	Barker and Rebeiz 1999, [28]	Perruisseau-Carrier, et al. 2006, [31]	Lakshminarayanan and Weller 2007, [33]	This work
Design characteristics				
Analog or digital	analog	digital (1 bit)	digital (1 bit)	analog
Differential or single-ended	single-ended	single-ended	single-ended	differential
Drive voltage	< 13 V	20 V	30-45 V	< 7 V
Frequency	40 GHz	20 GHz	12 GHz	10 GHz
Substrate	fused silica	silicon	fused silica	borosilicate glass
	$\epsilon_r = 3.78$, $\tan\delta = 0.0002$	$\epsilon_r = 11.7$, $\sigma = 10$ kΩ cm	$\epsilon_r = 3.78$, $\tan\delta = 0.0002$	$\epsilon_r = 5.1$, $\tan\delta = 0.006$
RF MEMS technology	fixed-fixed beam varactors	capacitive fixed-fixed beam switches	capacitive cantilever & fixed-fixed beam switches	fixed-fixed beam varactors
Transmission line	CPW	CPW	CPW	slotline
Figures of merit				
Phase shift / length	11.8°/mm	14.7°/mm	35°/mm	5.9°/mm
Phase shift / noise figure	70°/dB	72°/dB	429°/dB	28.2°/dB
Time delay / length	0.8 ps/mm	2 ps/mm	8.1 ps/mm	1.6 ps/mm
Time delay / noise figure	4.9 ps/dB	10 ps/dB	99.3 ps/dB	7.8 ps/dB

impedance matching (70°/dB at 40 GHz and 90°/dB at 60 GHz) [28], but can be overcome in digital designs using a combination of capacitive and inductive loading, which allowed for the realization of the lowest loss analog distributed loaded-line TTD phase shifter with 429°/dB at 12 GHz, 358°/dB at 50 GHz, and 150°/dB at 110 GHz [33]. A comparison with the prior art in distributed loaded-line TTD phase shifters is given in Table 5.1.

The RF MEMS slotline TTD phase shifter, designed for an electrically-thin Corning Pyrex 7440 borosilicate glass wafer ($\epsilon_r = 5.1$, $h = 500$ μm, $\tan\delta = 0.006$), is a scalable cascade of 62 novel differential slow-wave unit cells - i.e. more can be cascaded to obtain additional phase shift. The layout of the differential slow-wave unit cell is based on an electrically-short slotline section, s, of 350 μm, with a gap of 300 μm and an unloaded characteristic impedance, Z_u of 101.7 Ω at 10 GHz, which is loaded with a shunt impedance consisting of two center-pulled fixed-fixed beam RF MEMS varactors in series, sharing a common electrode, as shown in Fig. 5.3. The design parameters of the RF MEMS varactors are tabulated in Table 5.2. Expressions for pull-in voltage V_p, spring constant k, and switching time t_s, can be found in [3]. The RF MEMS varactors are integrated in the slot line edges in order to minimally disturb edge currents flowing along the slot. However, doing so increases the attenuation, α, as it becomes a function of the beam thickness, t_b, of the RF MEMS varactors, and it also increases the self-inductance of the slotline, L_T.

The theory and design methodology of analog distributed loaded-line TTD phase shifters, as described by Barker and Rebeiz [28, 30, 3], is not readily applicable because the RF MEMS slotline TTD phase shifter is differential, lossy and does not support a transverse electromagnetic (TEM) mode. The mode of propagation in a slotline is almost transverse electric (TE), exhibiting more dispersion than CPW or microstrip. Lossy transmission line theory is therefore applied on the lumped differential-mode half-circuit model of the slow-wave unit cell, as shown in Fig. 5.3, in order to derive expressions for attenuation, distortion, phase shift, power handling, S-parameters, and time delay. The model parameters are tabulated in Table 5.3 and are obtained from fitting the unbiased measurement results from 6 to 14 GHz. Due to the TE nature of the RF MEMS slotline TTD phase shifter, one should be cautious in extrapolating the lumped and semi-lumped simulation results beyond one octave bandwidth. The expressions can be evaluated with a numerical computing package such as GNU Octave or MATLAB in order to provide insight into the limitations of the disclosed design. In order to simplify the derivations, the equivalent shunt

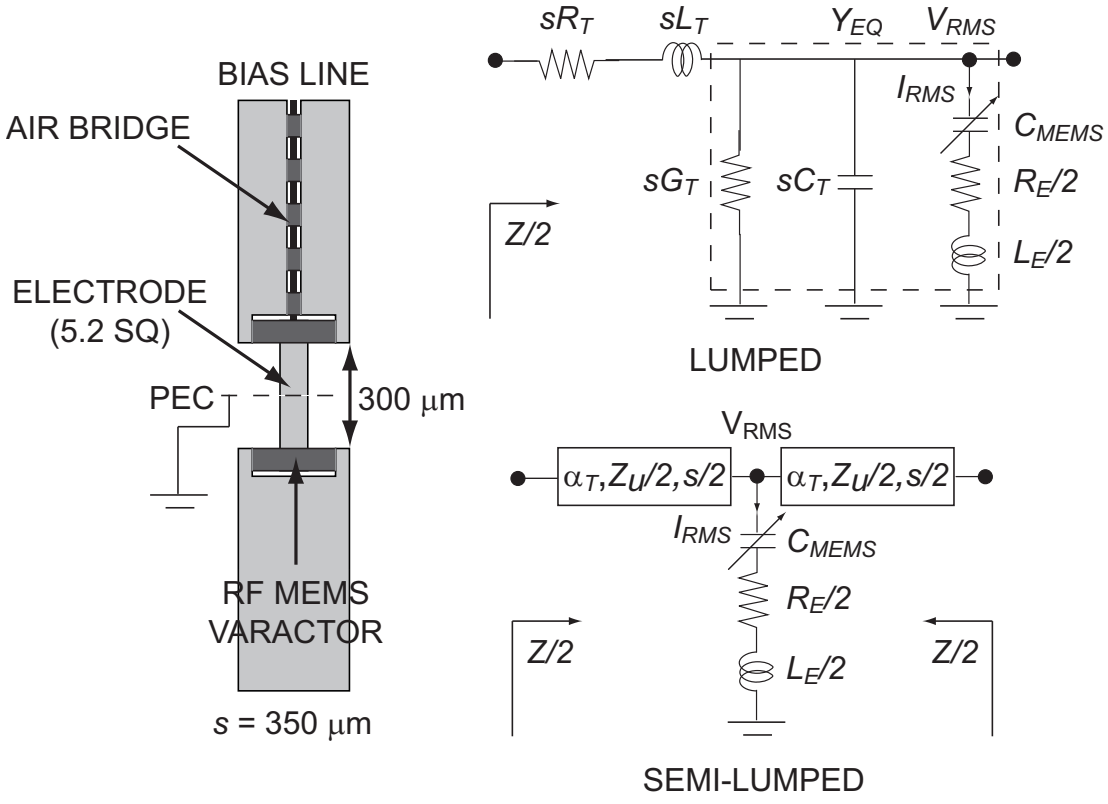

Figure 5.2: A differential slow-wave unit cell (left) and equivalent lumped and semi-lumped differential-mode half-circuit models (right).

admittance, Y_{EQ}, of the lumped differential-mode half-circuit model of the slow-wave unit cell is defined, as shown in Fig. 5.3.

$$Y_{EQ} = s\,(\,G_T + j\omega\,C_T) + \frac{1}{R_E/2 + j\,\omega\,L_E/2 + \frac{1}{j\,\omega\,C_{MEMS}}} \tag{5.1}$$

$G_{T_{EQ}}$ is defined as the equivalent transmission line shunt conductance, and $C_{T_{EQ}}$ is defined as the equivalent transmission line shunt susceptance of the differential-mode half-circuit.

$$G_{T_{EQ}} = \frac{\Re(Y_{EQ})}{s} \tag{5.2}$$

$$C_{T_{EQ}} = \frac{\Im(Y_{EQ})}{s\,\omega} \tag{5.3}$$

Table 5.2: Design parameters of the center-pulled contactless fixed-fixed beam RF MEMS varactor

Parameter	Value	Parameter	Value
Air Gap, g_0	1.5 μm	Dielectric Thickness, t_d	4000 Å
Beam Holes	No	Drive Voltage, V_s	0-7 V
Beam Length, l	300 μm	Electrode Area, A	8,000 μm^2
Beam Material[2]	Au	Electrode Width, W	100 μm
Beam Thickness, t	4000 Å	Residual Stress, σ	25 MPa
Beam Width, w	80 μm		
Capacitance Ratio, C_R	< 1.5	Pull-In Voltage, V_p	11.6 V
Capacitance, C_{MEMS}	63.9 fF - 95.8 fF	Spring Constant, k	8.6 N/m
Effective Mass, m	73.7 pkg	Switching Time, t_s	3.1 μs
Mech. Resonant Freq., f_m	54.2 kHz		

The complex propagation constant of the RF MEMS slotline TTD phase shifter becomes

$$\gamma = \sqrt{(R_T + j\,\omega\,L_T)\left(G_{T_{EQ}} + j\,\omega\,C_{T_{EQ}}\right)} \tag{5.4}$$

The characteristic impedance, Z, of the RF MEMS slotline TTD phase shifter can be optimized between 50 and 100 Ω in order to cut down on taper of the tapered slot antennas while preventing the structure from radiating. In this chapter, a characteristic impedance of 75 Ω differential is chosen, which is the input impedance of a $\lambda_0/2$ dipole. The characteristic impedance of the single-ended differential-mode half-circuit is $Z/2$.

$$\frac{Z}{2} = \sqrt{\frac{R_T + j\,\omega\,L_T}{G_{T_{EQ}} + j\,\omega\,C_{T_{EQ}}}} \tag{5.5}$$

With all model parameters defined, simple expressions are now derived for attenuation, distortion, phase shift, power handling, S-parameters, and time delay. Results are tabulated in Table 5.3 as well.

- **Attenuation:** The insertion loss of a well-matched RF MEMS slotline TTD phase shifter is $N\,s$ times the attenuation, α, expressed in dB/m.

[2]The Young's modulus, E, the Poisson ratio, ν, and the mass density, ρ, of gold are: 78 GPa, 0.44 and 19.2 g/cm^3 respectively. The resistivity of gold is 2.44 $\mu\Omega$ cm and the skin depth is 4830 Å at 26.5 GHz.

$$\alpha = 8.686\,\Re(\gamma) \tag{5.6}$$

$$\approx \frac{8.686}{2}\left(R_T\sqrt{\frac{C_{T_{EQ}}}{L_T}} + G_{T_{EQ}}\sqrt{\frac{L_T}{C_{T_{EQ}}}}\right) \tag{5.7}$$

The insertion loss is affected by the T-line resistance, R_T, and the electrode resistance, R_E, or equivalently by the finite Q factor of the shunt impedance. The attenuation of an RF MEMS slotline TTD phase shifter is higher than the attenuation of its CPW and microstrip counterparts.

- **Differential phase shift:** At frequencies below the Bragg frequency, f_B, the phase shift, $\Delta\phi$, expressed in degrees, of the RF MEMS slotline TTD phase shifter is the difference of $N\,s$ times the propagation constant, β, between the biased and the unbiased state.

$$\Delta\phi = \frac{180}{\pi}N\,s\,(\beta\,[V_s] - \beta\,[0]) \tag{5.8}$$

$$= \frac{180}{\pi}N\,s\,(\Im(\gamma\,[V_s]) - \Im(\gamma\,[0])) \tag{5.9}$$

The Bragg frequency is the frequency at which the characteristic impedance, Z, of the RF MEMS slotline TTD phase shifter becomes zero, indicating a transmission zero. The Bragg frequency of the RF MEMS slotline TTD phase shifter is primarily affected by the electrode inductance, L_E.

- **Distortion:** Lossy transmission lines can be distortionless if

$$\frac{R_T}{L_T} = \frac{G_{T_{EQ}}}{C_{T_{EQ}}} \tag{5.10}$$

The R_T/L_T quotient is 1.29e9 and the $G_{T_{EQ}}/C_{T_{EQ}}$ is 2.35e9 for the unbiased state and 2.45e9 for the biased state of the disclosed RF MEMS slotline TTD phase shifter. A quantitative number for distortion is the group velocity dispersion [67], expressed in fs / (mm mm),

$$D = -\frac{2\pi c}{\lambda_0^2}\frac{d^2\beta}{d\omega^2}10^3 \tag{5.11}$$

in which λ_0 is the wavelength in free space and β is the propagation constant, expressed in rad/m. $|D|$ is the temporal pulse spreading, expressed in ps, per unit bandwidth, expressed in mm, and per unit distance travelled, also expressed in mm. $|D|$ is 20.8 fs/(mm mm) for the unbiased state and 37.1 fs/(mm mm) for the biased state of the disclosed RF MEMS slotline TTD phase shifter.

- **Power handling:** Self-actuation is the primary cause of failure of a center-pulled contactless fixed-fixed beam RF MEMS varactor under high-power operation [51]. Self-actuation occurs when the root mean square (RMS) of the RF voltage across the RF MEMS varactor, $V_{s_{EQ}}$, exerts an equivalent drive voltage exceeding the pull-in voltage, V_p. However, for analog center-pulled fixed-fixed beam RF MEMS varactors, $V_{s_{EQ}}$ should be further restrained to approximately $V_p/2$ in order to prevent the RF signal from self-phasing under high power operations. In order to calculate the RF power corresponding to $V_{s_{EQ}} = V_p/2$, an expression for the RMS of the RF voltage across the differential-mode half-circuit, V_{RMS}, is derived, applying voltage division:

$$V_{RMS} = \left| \frac{\frac{1}{j\,\omega\,C_{MEMS}} + j\,\omega\,L_E/2 + R_E/2}{\frac{1}{j\,\omega\,C_{MEMS}}} \right| V_{s_{EQ}} \tag{5.12}$$

  The maximum power handling of the RF MEMS slotline TTD phase shifter, expressed in dBm, can be calculated as

$$P = 10\,\log\frac{V_{RMS}^2}{|Z/2|} + 33 \tag{5.13}$$

  The power handling of a 50 or 75 Ω differential RF MEMS slotline TTD phase shifter exceeds the power handling of its CPW and microstrip counterparts, based on the same center-pulled fixed-fixed beam RF MEMS varactors, by more than 3 dB, because of the power division among the differential-mode half-circuits and because of the RF voltage division over the RF MEMS varactors, the electrode inductance, L_E, and the electrode resistance, R_E. The reported power handling of RF MEMS CPW and microstrip TTD phase shifters is 27 dBm [3].

- **S-parameters:** The S-parameters can be calculated by converting the Nth power of the ABCD matrix to an S matrix.

$$\begin{bmatrix} A & B \\ C & D \end{bmatrix}^N = \left(\begin{bmatrix} 1 & s\,R_T + j\,\omega\,s\,L_T \\ 0 & 1 \end{bmatrix} \begin{bmatrix} 1 & 0 \\ Y_{EQ} & 1 \end{bmatrix} \right)^N \tag{5.14}$$

- **Time delay:** The time delay, $\Delta\tau$, is expressed as:

$$\Delta\tau = \frac{\Delta\phi}{\omega} \tag{5.15}$$

The scanning angle, θ, measured from the boresight, of an electronically scanned array with TTD beam steering is expressed as:

$$\theta = \arcsin\left(\frac{c}{d}\,\Delta\tau\right) \tag{5.16}$$

in which c is the speed of light in free space and d is the element spacing of the electronically scanned array.

The semi-lumped differential-mode half-circuit model is shown in Fig. 5.3 and model parameters are tabulated in Table 5.3. Full-wave simulations, such as method of moments (MoM) simulations, are, although less insightfull, preferred over lumped and semi-lumped modelling because the non-TEM nature of the slotline is taken into account. The RF sheet resistance of the layers, necessary for accurate MoM simulations, is given in the Fabrication section. Good agreement between simulation results, obtained with all techniques, and measurement results is observed for the unbiased state, as will be illustrated in the Measurements section.

5.3 Fabrication

Micro-fabrication techniques allow monolithic integration of air bridges, bias lines, and RF MEMS varactors. The fabrication process requires 6 masks and consists of the following steps:

1. The electrode layer is defined through a trifluoroacetic acid (TFA) back-etch of a 100/2000/200 Å thick film of evaporated Ti/Au/Ti. The RF sheet resistance, R_s, of a 2000 Å film is 0.145 Ω/sq.

Table 5.3: Model parameters of the lumped and semi-lumped differential-mode half-circuit of the slow-wave unit cell at 10 GHz

Lumped model	
Parameter	Value
Attenuation, α	158.7 - 192.1 dB/m
Bragg frequency, f_B	$>$ 60 GHz
Effective phase velocity, v_{eff}	0.997 - 0.846 10^8 m/s
Electrode Inductance, L_E	204.4 pH
Electrode Resistance, R_E	8.3 Ω
Group velocity dispersion, $\|D\|$	20.9 - 37.1 fs/(mm mm)
Number of unit cells, N	62
Power, P	27 dBm
Propagation constant, β	630.4 - 743.1°/m
Q factor	59.9
RF MEMS capacitance, C_{MEMS}	63.9-95.8 fF
Spacing, s	350 μm
T-line capacitance, C_T	58.1 pF/m
T-line conductance, G_T	0.376 S/m
T-line inductance, L_T	411 nH/m
T-line resistance, R_T	531 Ω/m
Semi-Lumped model	
Parameter	Value
Effective dielectric constant, ϵ_{eff}	3.05
Loss tangent, $\tan\delta$	0.006
Unloaded characteristic impedance, Z_u	101.7 Ω

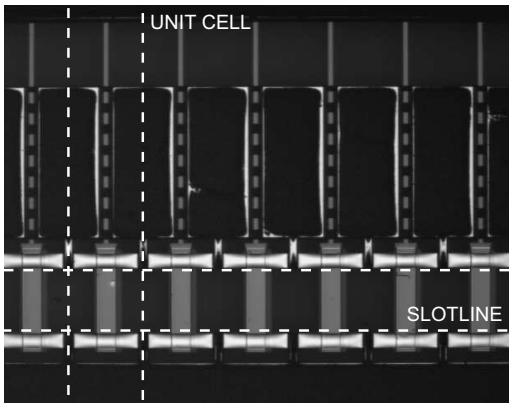

Figure 5.3: Optical microscopy imagery of the fabricated analog RF MEMS slotline TTD phase shifter.

2. The dielectric layer, used to insulate the dielectric, is defined through a buffered hydrofluoride (BHF) back-etch process of a 2000 Å thick film of plasma enhanced chemical vapor deposition (PECVD) silicon nitride with a dielectric constant of 7.6, which is deposited twice in order to avoid pin holes. The breakdown voltage of PECVD silicon nitride is 50 V/kÅ.

3. The bias lines are defined through lift-off of a 1200 Å thick film of sputtered high-resistivity SiCr (70% Si and 30% Cr). The resistivity of SiCr is 8657 $\mu\Omega$ cm and the DC sheet resistance of the bias lines is 721 Ω/sq. Note that RF MEMS varactors are electrostatically actuated and do not draw a bias current nor dissipate DC power.

4. The sacrificial spacer is defined through a back-etch of a 1.75 μm thick film of spin coated Microchem 950PMMA A9. The reactive ion etcher (RIE) is used for the back-etch, using a 500 Å thick on-wafer mask of evaporated Ti. The major advantage of PMMA as a sacrificial spacer over conventional photo resists is that it reflows conformally after spin coating, making the beams flatter and avoiding mechanical failure due to vertical steps.

5. A 200/4000/500 Å thick film of Ti/Au/Ti, with an RF sheet resistance of 0.074 Ω/sq, is sputtered over the entire wafer and used as a seed layer to selectively plate 1.1 μm of gold on top of the device. The purpose of the gold electroplating is threefold. Firstly, the anchors of the RF MEMS beams are reinforced, which ensures beam flatness after

release. Secondly, electroplating makes the air bridges stiffer and prevents them from pulling in when a bias voltage is applied. Thirdly, the metal thickness is increased, which reduces conduction losses. The RF sheet resistance, R_s, of a 1.7 μm film is 0.045 Ω/sq.

6. The beams are defined through a trifluoroacetic acid (TFA) back-etch of the seed layer. The sacrificial spacer is desolved overnight in hot PRS-2000, and the wafer is dried in a critical point dryer, which is necessary to prevent the beams from getting stuck in the down-state. Optical microscopy, as shown in Fig. 5.3, and optical interferometry are used to verify that the beams are in the up-state. A deviation between the desired air gap (1.75 μm) and the average realized air gap (1.5 μm) is observed, and is due to the sacrificial spacer reflow and beam inflatness.

5.4 Measurements

5.4.1 Biasing

The RF MEMS varactors of the analog RF MEMS slotline TTD phase shifter - henceforth referred to as the device under test (DUT), are designed to have a low pull-in voltage, V_p, in order to make the design compatible with transistor transistor logic (TTL) biasing circuits, which operate at 2-5 V voltage levels. The DUT is biased through a Picoprobe 40A-GSG-150-T probe using a bipolar drive voltage, V_s, of 0-7 V in order to avoid dielectric charging and to increase the lifetime of the device. The measured pull-in voltage, V_p, is 7.5-11 V, which is close to the design value.

5.4.2 S-Parameters

The differential S-parameters of the DUT are measured with a 2-port Agilent 8722ES vector network analyzer in conjunction with two 6-26.5 GHz Krytar Model 4060265 180° hybrid couplers. The 180° hybrid couplers and the Picoprobe Model 40A-GSG-250/40A-GSG-250-D-500 differential probes are connected by semi-rigid SMA cables, which limit the differential measurement setup to 14 GHz due to the amplitude and phase imbalance they cause. In this regard a differential S-parameter measurement with a 4-port vector network analyzer, such as the Agilent N5230A, would have extended the measurement to

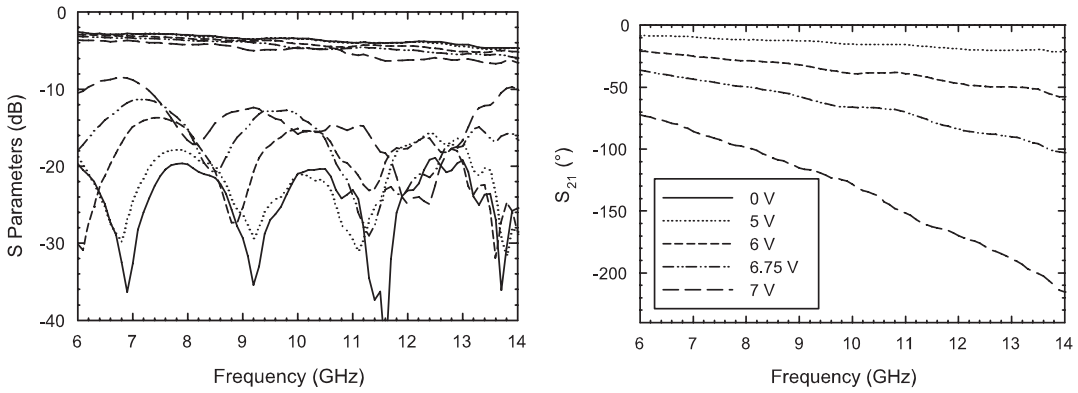

(a) Insertion loss and return loss (0-7 V)

(b) Differential phase shift (0-7 V)

Figure 5.4: Measured S-parameters of DUT (Renormalized to 75 Ω differential)

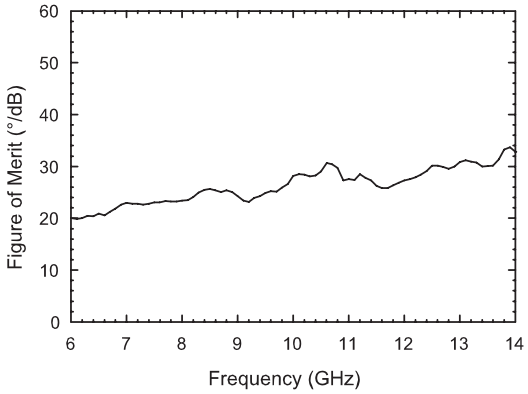

Figure 5.5: Measured phase shift versus noise figure

20 GHz. The wafer is placed on a glass chuck, in order not to ground the slot mode, and the setup is calibrated using the Picoprobe CS-2-250 differential calibration substrate and the short-open-load-thru SOLT calibration algorithm of Cascade WinCal 3.5, in which the probe-manufacturer's specifications for standards were not used. The differential S-parameters, measured in a 100 Ω differential transmission line system, are renormalized to 75 Ω differential after deembedding of the probe pads. The measurement results are shown in Fig. 5.4; the measured insertion loss at 10 GHz varies between 3.45 to 4.56 dB (0-7 V), the measured return loss varies between 21 dB to 15.8 dB (0-7 V) and the obtained phase shift is 128.5° (7 V). The phase shift per decibel NF, as shown in Fig. 5.5, is 28.2°/dB and the time delay per decibel NF is 7.8 ps/dB. The loss can be reduced by increasing the beam thickness of the RF MEMS varactors, t_b, at the expense of an increase in bias voltage

Table 5.4: DUT Performance at 10 GHz

Simulated (Method of Moments)					
	S_{11} (dB)	S_{21} (dB)	S_{21} (°)	$\Delta\tau$ (ps)	$\lvert D\rvert$ (fs/(mm mm))
UNBIASED	-23.8	-3.5	-760.9	0	20.8
BIASED (7 V)	-14.8	-4.2	-856.4	26.5	37.1
Measured					
	S_{11} (dB)	S_{21} (dB)	S_{21} (°)	$\Delta\tau$ (ps)	$\lvert D\rvert$ (fs/(mm mm))
UNBIASED (0 V)	-21	-3.45	-782.03	0	3.7
BIASED (7 V)	-15.8	-4.56	-910.5	35.6	10.4

from 0-7 V to 0-40 V. UWB (DC-14 GHz) operation is feasible. Simulated and measured return loss, insertion loss, phase shift and time delay of the DUT are tabulated in Table 5.4. Good agreement between lumped, semi-lumped and method of moments simulation results and measurement results is observed for the unbiased state, as shown in Fig. 5.6. The lumped and semi-lumped simulation results for the biased state, obtained by changing the C_{MEMS} model parameter from 63.9 fF to 95.8 fF, deviate on average approximately 1 dB in insertion loss and 10 dB in return loss from the measurement results. Nevertheless, lumped and semi-lumped modelling remains a useful tool for first-order performance evaluation.

5.4.3 Linearity

The third-order intercept point, IP3, follows the mechanical response of the beam of the RF MEMS varactor and the third-order intermodulation product, IM3, drops 40 dB/decade for $\Delta f > f_m = 54.2$ kHz, in which f_m is the mechanical resonant frequency of the RF MEMS varactor [3]. The linearity of the DUT is demonstrated through a measurement of the IP3 at 10 GHz in a 100 Ω differential transmission line system, in which $S_{11_{dd}}$ is -13.621 dB and $S_{21_{dd}}$ is -3.866 dB at 10 GHz (0 V). The spacing of the two carriers Δf is 50 kHz, and the fundamental and IM3 frequencies are: $2f_1 - f_2 = 9.999973$ GHz, $f_1 = 10.000022$ GHz, $f_2 = 10.000070$ GHz, $2f_2 - f_1 = 10.000118$ GHz. Fig. 5.7 depicts the measurement setup where the distinction is made between the transmitted power at the vector network analyzers operating in CW mode, P_T, the power at the input port of the DUT, P_{IN}, the power at the output port of the DUT, P_{OUT}, and the received power at the spectrum analyzer P_R. P_{IN}

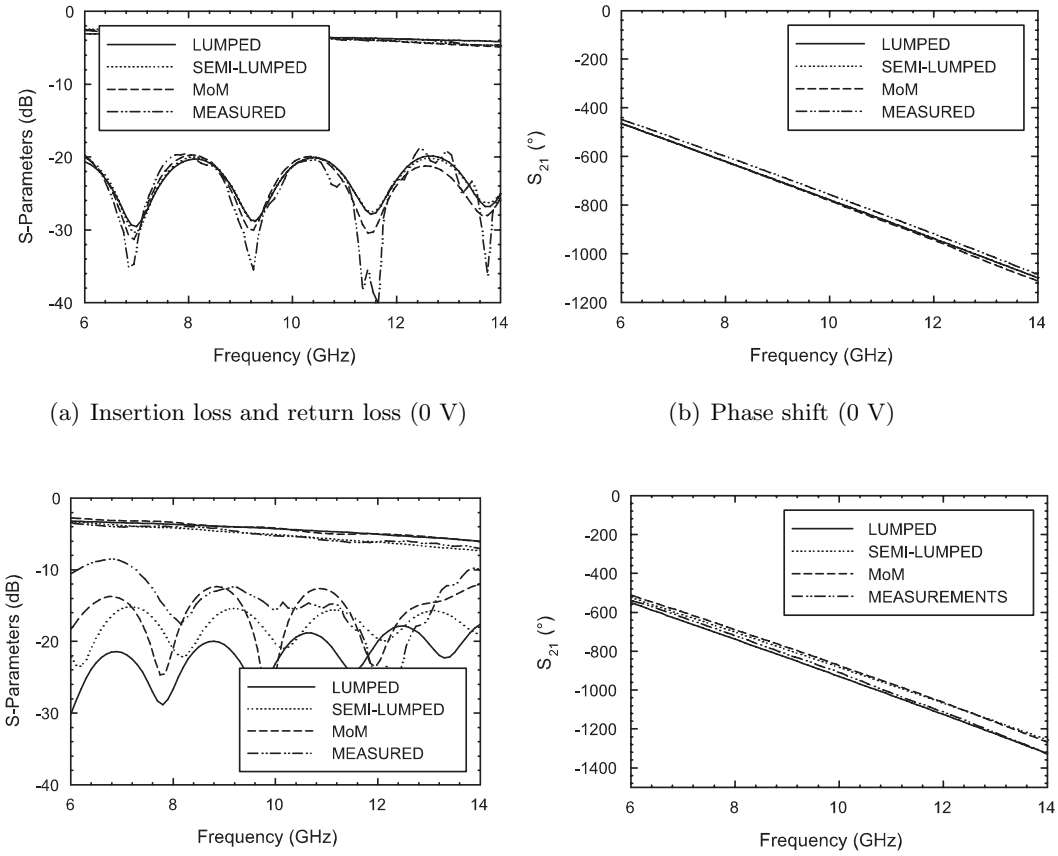

(a) Insertion loss and return loss (0 V)

(b) Phase shift (0 V)

(c) Insertion loss and return loss (7 V)

(d) Phase shift (7 V)

Figure 5.6: Comparison of measured and simulated S-parameters of DUT (renormalized to 75 Ω differential)

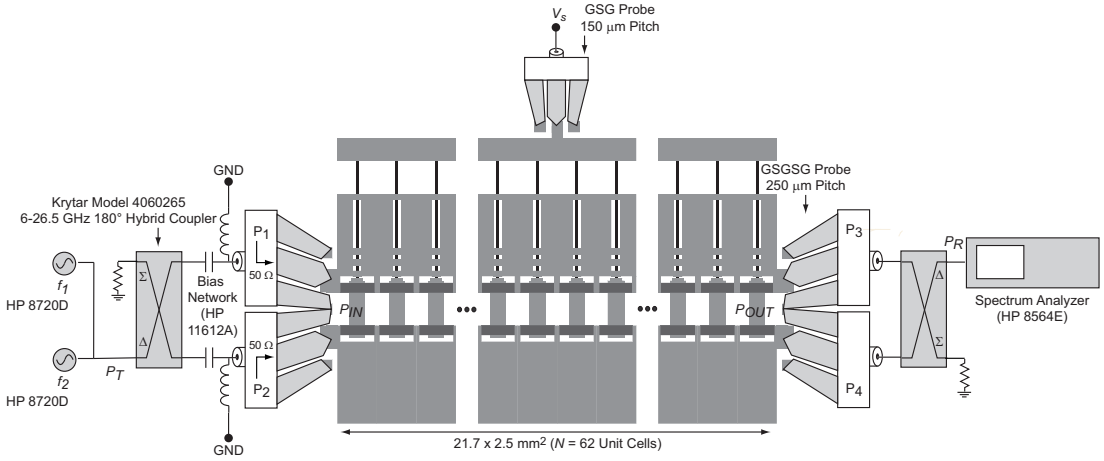

Figure 5.7: IP3 measurement setup (100 Ω differential)

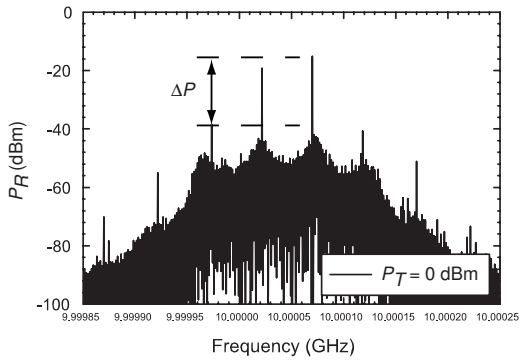

Figure 5.8: IP3 measurement of DUT (100 Ω differential)

is P_T minus the loss incurred between the vector network analyzers and the input port of the DUT (≈ 7.5 dB), and P_{OUT} is the sum of the loss incurred between the output port of the DUT and spectrum analyzer (≈ 3.8 dB) and P_R. Fig. 5.8 shows the P_R spectrum for P_T equal to 0 dBm. The input IP3 (IIP3), expressed in dBm, is obtained using

$$IIP3 = \frac{\Delta P}{2} + P_{IN} \tag{5.17}$$

with $\Delta P/2$ = 12.5 dB and P_{IN} = -7.5 dBm, and equates to 5 dBm. While the IIP3 can be increased by increasing the beam thickness, t_b, interference mitigation in wideband limited field-of-view systems is implemented more effectively using adaptive null steering.

5.4.4 Power Handling

The Hughes 1177H X-band TWT power amplifier is inserted between the Agilent 8722ES vector network analyzer, operating in CW mode, and the 180° hybrid couplers in order to verify the power handling of the DUT in a 100 Ω differential transmission line system. The power handling is verified up to P_{IN} = 28 dBm (P_T = 33 dBm) with approximately 5 dB of loss incurred between the power amplifier output and the DUT. No self-actuation (V_{RMS}-limited power handling) or electromigration (I_{RMS}-limited power handling) is observed.

5.5 Future Work

Lumped modelling indicates that the phase shift and the V_{RMS}-limited power handling can be increased to 60°/dB and 36 dBm ($V_{S_{EQ}}$ = 10 V), by fabricating the disclosed design

on a fused silica wafer with a beam thickness, t_b, of 8000 Å instead of 4000 Å, at the expense of an increase in bias voltages to 30-40 V. In addition, the electrode can be electroplated to further reduce the attenuation and equalize the distortion quotients. A millimeter-wave design will have a higher phase shift per decibel NF, as the phase shift increases linearly with the frequency, f, and the conductor loss increases with $\sqrt{f}$. Increasing the capacitive loading will increase the phase shift and decrease distortion as well, but will increase the return loss.

Design opportunities include a digital design based on impedance-matched differential slow-wave unit cells using a combination of capacitive and inductive loading in order to greatly enhance the phase shift per decibel NF. The differential slow-wave unit cell can also be implemented on other transmission line types, such as coplanar strips or unilateral finline [68]. An implementation on coplanar strips, which supports a TEM mode, will decrease dispersion over multiple octaves bandwidth. An implementation on unilateral finline, which is a one-conductor structure not supporting a TEM mode and with a cut-off frequency for the ground mode, offers a packaging opportunity. In addition, the analog slotline TTD phase shifter design can be implemented using monolithically integrated ferroelectric varactors or PIN diodes. Finally, other applications of the differential slow-wave unit cell include filters, leaky wave antennas and wideband frequency tunable slot antennas.

5.6 Conclusion

An analog RF MEMS slotline true time delay (TTD) phase shifter has been presented with compelling applications in wideband limited field-of-view systems. The design is a scalable distributed loaded-line cascade of 62 novel differential slow-wave unit cells. Each differential slow-wave unit cell comprises an electrically-short slotline section, which is loaded with a shunt impedance consisting of two center-pulled contactless fixed-fixed beam RF MEMS varactors in series, sharing a common electrode. The analog RF MEMS slotline TTD phase shifter is designed for transistor to transistor logic (TTL) bias voltage levels and exhibits a measured phase shift of 28.2°/dB (7.8 ps/dB) and 59.2°/cm at 10 GHz, maintaining a 75 Ω differential impedance match (S_{11} < -15.8 dB). The IIP3 is 5 dBm at 10 GHz for a Δf of 50 kHz, measured in a 100 Ω differential transmission line system. Design and fabrication opportunities, concerning distortion and loss reduction, as well as

packaging, have been discussed.

Acknowledgements

Prof. Jack East is thanked for kindly providing the Hughes 1177H X-band TWT power amplifier and Prof. Gabriel Rebeiz, UCSD, is thanked for providing the two 6-26.5 GHz Krytar Model 4060265 180° hybrid couplers. Fabrication of the RF MEMS slotline TTD phase shifter was done in the Michigan Nanofabrication Facility (MNF).

CHAPTER 6

A 94 GHz OFDM Frequency Scanning Radar

6.1 Introduction

Autonomous landing guidance (ALG) is an airborne navigation radar developed by BAE Systems North America in collaboration with MBDA UK. The 94 GHz ALG radar reduces dependence on ground-based instrument landing system (ILS) and space-borne GPS in landing the aircraft by allowing pilots to map the runway even under adverse weather conditions (ILS Category III C) [69, 70]. The selected radar frequency, 94 GHz, provides a pencil beam pattern despite stringent aperture size constraints and offers good image quality at operational ranges in all weather conditions, including low cloud, snow, mist and fog. The 94 GHz propagation window suffers from increased atmospheric attenuation in very heavy rain but benefits from greater contrast between concrete and vegetation compared to the 35 GHz propagation window. The ALG radar operates in ground mapping mode when the airplane starts descending on the ILS glide slope, typically 180 m to 150 m above ground and approximately 3 km from touchdown, as shown in Fig. 6.1. In order to image a wide swath with a 15 m cross-track (azimuth) resolution, a 0.3° beam with a scanning range of ±20° is required. Table 6.1 summarizes the desired specifications for a next-generation ALG radar. Note that the free space wavelength λ_0 at 94 GHz is 3.19 mm.

In this chapter, a novel 94 GHz orthogonal frequency division multiplexing (OFDM) frequency scanning radar (FSR) concept is presented, which offers potential cost and size reductions over the legacy design. A variety of phased array architectures [16, 71, 72, 12, 73, 74, 75, 76, 15] have initially been considered for a next-generation ALG radar and include frequency scanning, commutating beam based on a monopulse true time delay (TTD) beam

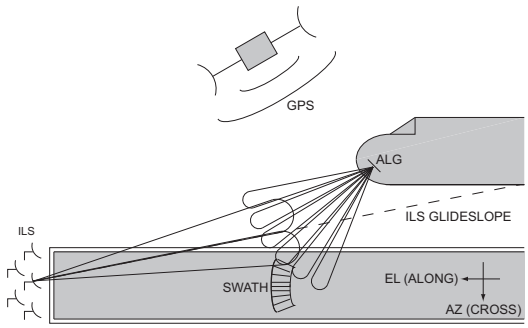

Figure 6.1: High resolution millimeter-wave imaging radars can assist pilots from a point on the ILS glide slope, typically 180 to 150 m above ground level and approximately 3 km from touchdown.

former and beam forming networks (BFNs) producing multiple spatially orthogonal beams.

A helical or serpentine waveguide-fed slot array that scans with frequency is selected for following reasons: cost, environmental and shock tolerance, power handling, simplicity, size. Frequency scanning is an old and established technique side-lined by the emergence of the monopulse TTD beam formers which are wideband and allow angle detection with an angular resolution that is a fraction of the beamwidth. Bandwidth is inversely related to the pulse width of the radar waveform as well as to the pulse-limited slant range resolution. The drawbacks of frequency scanning are decreased signal bandwidth and pulse-limited slant range resolution compared to TTD beam formers and the inability to take advantage of monopulse angle tracking techniques. However, at 94 GHz there is ample bandwidth to fit a pulse-Doppler radar waveform that provides sufficient pulse-limited slant range resolution. The availability of excess bandwidth allows the radar band to be divided into subbands (channels) using OFDM as shown in Fig. 6.2. Each subband carries a "colored" pulse-Doppler radar waveform for slant range and Doppler frequency shift detection and corresponds to a certain scanning angle. In addition, all scanning angles are measured at once, providing the pilot with an adequate refresh rate for the radar image. Note that legacy FSRs employ frequency swept local oscillators to vary the RF frequency and sequentially scan the beam.

OFDM divides the frequency spectrum into subbands small enough to allow for the channel transfer function to be assumed constant within a single subband. A subband software-defined radar waveform (echo) is I/Q (de)modulated using, for example, m-ary quadrature

Table 6.1: Desired specifications for a next-generation ALG radar

Specifications	Acceptable	Desirable
Aperture size	60 cm × 7 cm	45 cm × 7 cm
	188 × 22 λ_0	141 × 22 λ_0
Half-power beamwidth, β	AZ 0.3°, EL 0.3°	AZ 0.3°, EL 0.3°
Cost	\$30K	\$20K
Mean radiated power, P_m	0.5 W	2 W
Polarization	Vertical	Polarimetric
Maximum scanning angle	±20°	±45°
Scanning angular resolution	0.3°	0.3°
Slant range	3 km	6 km
Slant range resolution, r	1 m	30 cm

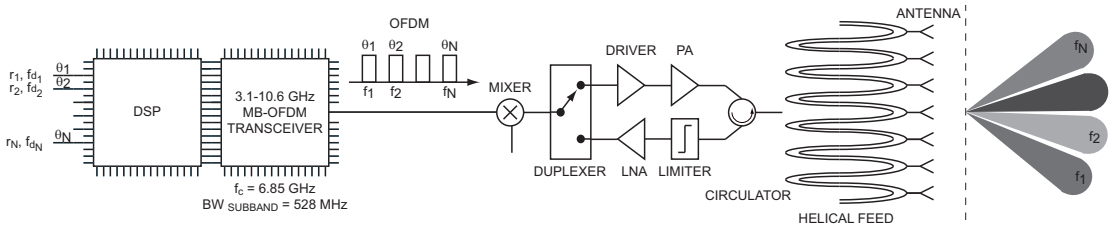

Figure 6.2: OFDM is used in conjunction with frequency scanning to provide high-resolution millimeter-wave imaging through low-cost and low-profile angle detection.

amplitude modulation (m-QAM). Fast fading effects[1], which induce high Doppler spread, disappear as they occur during the transmission of a single symbol.

Multi-carrier radar waveforms with favorable ambiguity function and peak-to-mean envelope power ratio (PMEPR) were introduced by Levanon and Mozeson in 2000 [77]. This chapter envisions the use of OFDM in conjunction with frequency scanning to provide high-resolution millimeter-wave imaging through low-cost and low-profile angle detection [78]. Indeed, the helical and serpentine waveguide-fed slot arrays are arguably among the cheapest existing phased array architectures and offer size reductions over Cassegrain reflector based

[1]Fast fading induces a high Doppler spread. The coherence time is less than the symbol period. The channel variations are faster than baseband signal variations.

designs. In addition, single-chip RF CMOS radios for multiband OFDM (MB-OFDM), as advocated by the WiMedia Alliance, will provide cost-effective half-duplex ultra-wideband transceivers [79, 80, 81]. A waveguide-based cold-switched T/R module is to be inserted between the OFDM transceiver and the helical or serpentine waveguide-fed slot array to up-convert and amplify the transmitted radar waveform and to down-convert the echo after reception with wide dynamic range. The inability to use monopulse techniques to increase the angular resolution in the cross-track [82, 13] can be overcome by implementing adjacent subband lobing, which is a technique similar to subpulse beam switching [83]. Adjacent subband lobing interpolates the angular position by comparing the amplitude of echoes received in adjacent subbands, which correspond to adjacent beams, after edge detection filtering. Doppler beam sharpening (DBS) can be applied to synthetically increase the off-nose along-track resolution as well [82, 84, 85].

6.2 Design

Six equations relate the design specifications of an FSR based on a uniformly excited phased array. It is assumed that no pulse compression is used - i.e. the time bandwidth product is equal to 1.

- The half-power beamwidth β in degrees is

$$\beta = 65\frac{\lambda_0}{N\,d} \tag{6.1}$$

  in which N is the number of array elements and d/λ_0 is the element spacing relative to the free-space wavelength at 94 GHz. For $N = 32$ and $d/\lambda_0 = 0.72$, β is 2.82°.

- The helical waveguide-fed slot array has 7 λ_{g_0} of electrical length s per turn, where λ_{g_0} is the wavelength of the TE_{10} mode at 94 GHz, to allow ±20° beam scanning from the boresight over a 4 GHz bandwidth.

$$\theta(f) = \arcsin\left(\frac{\lambda}{d}\left(\frac{s}{\lambda_g(f)} - \frac{s}{\lambda_{g_0}}\right)\right) \tag{6.2}$$

  The wavelength $\lambda_g(f)$ of the TE_{10} TE_{10} mode is

$$\lambda_g(f) = \frac{\lambda(f)}{\sqrt{1 - \left(\frac{\lambda(f)}{2\,a}\right)^2}} \tag{6.3}$$

in which $a = 2.54$ mm is the width of the WR-10 waveguide aperture. The scanning angle versus frequency is shown in Fig. 6.4.

- The relation between pulse-limited slant range resolution r and angular resolution or half-power beamwidth β is given in [16]

$$BW \leq \frac{\beta\,\Delta f}{256\,\sin\theta_m} \tag{6.4}$$

The maximum subband signal bandwidth BW is calculated for $\beta = 2.82°$ and $\Delta f = 4$ GHz, which is the bandwidth over which the FSR scans out to $\pm\theta_m$. θ_m is the maximum scanning angle and is equal to 20°. The maximum subband signal bandwidth BW that can be used is approximately 128.9 MHz, corresponding to a pulse-limited slant range resolution of 1.16 m using $r = c\tau/2$.

- The directivity in the cross-track (azimuth) of a linear array is [86]

$$D_a = 4.13\frac{N\,d}{\lambda_0} \tag{6.5}$$

yielding 19.8 dBi. The directivity in the along-track (elevation), D_e, is assumed to be 10 dBi. The 2-D directivity is related to the product of D_a and D_e. Assuming an array efficiency of 100% for now, the 2-D gain equals the 2-D directivity. Note that D_e can be improved by connecting the helical waveguide-fed slot array to a continuous transverse stub (CTS) array.

- The radar range equation is given by

$$R = \sqrt[4]{\frac{\lambda_0^2\,EIRP\,G_r/T\,\sigma}{64\,\pi^3\,k_B\,BW\,SNR}} \tag{6.6}$$

in which $EIRP = G_tP_t = 47.577$ MW, assuming an overall 2-D array gain $G_r = G_t = 29.8$ dBi and a peak transmit power $P_t = 50$ kW, and in which the target RCS, σ, is assumed to be 10 dBsm and the SNR is set to 20 dB. k_B is the Boltzmann constant.

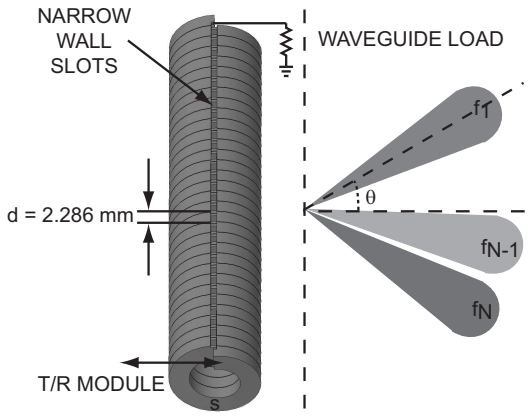

Figure 6.3: Ansoft HFSS model. 32 Turns with varying slot width constitute the helical waveguide-fed slot array.

At room temperature the range equation yields a maximum range detection up to 2.58 km.

- The mean radiated power, P_m, which is regulated, is

$$P_m = \frac{P_t}{PMEPR} = \frac{P_t\, PRF}{BW} \tag{6.7}$$

in which the pulse repetition frequency (PRF) is 10 kHz, yielding a $P_m = 2.58$ W per subband.

6.3 Components

6.3.1 Helical Waveguide-Fed Slot Array

A 94 GHz helical waveguide-fed slot array for wide-angle frequency scanning, as shown in Fig. 6.3, is designed. Several trade-offs are made in the design of a waveguide-fed slot array [87, 83, 88]:

- **Standing-wave versus travelling-wave feeding**: When the slots are equispaced a distance s not equal to $\lambda_g/2$, and when the waveguide is terminated in a matched load, the waveguide-fed slot array is said to be travelling-wave fed. While standing-

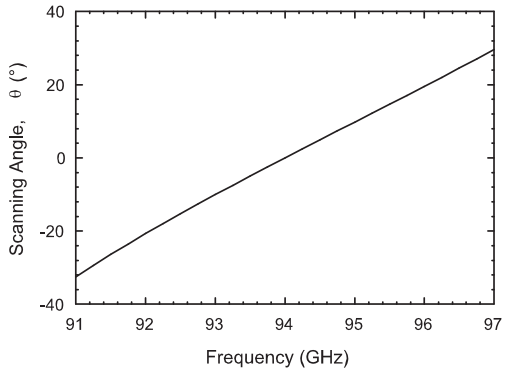

Figure 6.4: Scanning angle versus frequency as extrapolated from single turn S_{21} measurements.

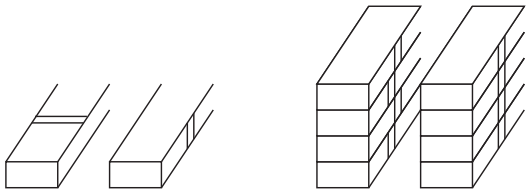

Figure 6.5: Broad wall versus narrow wall slots (left) and linearly aligned versus overlapping subarrays (right)

wave feeding allows for higher efficiency, its resonant impedance bandwidth drastically reduces the ability to scan with frequency and limits the maximum scanning angle.

- **Helical versus serpentine waveguide feeding**: Helical waveguide feeds have larger impedance bandwidth than serpentine waveguide feeds, but are not amenable to a two dimensional array implementation.

- **Broad wall versus narrow wall slots** (see Fig. 6.5): The slots are milled from the narrow wall in order to reduce the element spacing, d, and to allow wide-angle frequency scanning in the E-plane without intrusion of grating lobes in the visible region. Contrary to inclined broad wall slots, narrow wall slots cannot be assumed to be lying in an infinite ground plane and an analytical model for prediction of radiation characteristics is not available. However, the radiation characteristics of a rectangular aperture in free-space with a uniform field distribution are a good approximation [89].

- **Slot alignment** (see Fig. 6.5): The slots are linearly aligned in order to maximize directivity and minimize beamwidth. Ordering the slots on two parallel overlapping subarrays reduces mutual coupling at the expense of reduced directivity and increased beamwidth.

- **Slot width taper**: The slot width is tapered in order to excite the waveguide-fed slot array uniformly as uniform excitation minimizes the beamwidth. The slot width is bound between 0.2 mm to 1.5 mm. The minimum manufacturable slot width is 0.2 mm and sets the radiated power per slot. At 1.5 mm the slot width attains resonant length at 100 GHz.

- **Copper versus stainless steel**: The WR-10 waveguide wall thickness, as set by the MIL-DTL-85/3BL specification, is 1 mm for copper or coined silver and 0.5 mm for stainless steel. A stainless steel implementation reduces element spacing ($d/\lambda_0 = 0.72$) with grating lobes entering the visible region when scanning beyond 20° from the boresight above 96 GHz. However, stainless steel also attenuates the TE_{10} mode more (17 dB/m) than copper (2.6 dB/m), yielding lower gain. Galvanization of the inside of the helical waveguide-fed slot array is possible, but expensive.

The S-parameters of single helical waveguide turns with varying slot widths are simulated with the Ansoft HFSS finite element method (FEM) package, as shown in Fig. 6.6. The problem is electrically large and remains hard to solve by state-of-the-art workstations. The FEM solver adaptively refines the mesh during every pass in order to converge to the S-parameters. While amplitude convergence is observed and the S-parameters stated in dB are trustworthy, phase convergence is not observed within feasible mesh complexity.

The performance of three helical waveguide turns with varying slot width (w = 0 mm, 1 mm and 1.5 mm) is verified experimentally. The S-parameters of the helical waveguide turns are measured with an HP 85106D millimeter-wave network analyzer and are shown in Fig. 6.7(a). The three $|S_{21}|(w)$ data points are compared with HFSS simulation results at 94 GHz, as shown in Fig. 6.7(b). Good agreement is achieved. Co- and cross-polarized gain are derived from an S_{21} measurement using the gain-comparison measurement technique and are shown in Fig. 6.8(a) and Fig. 6.8(b). It is observed that the gain, stated in dB, regresses linearly on the slot width, whereas and the polarization purity increases with the slot width. The measurement setup is depicted in Fig. 6.9.

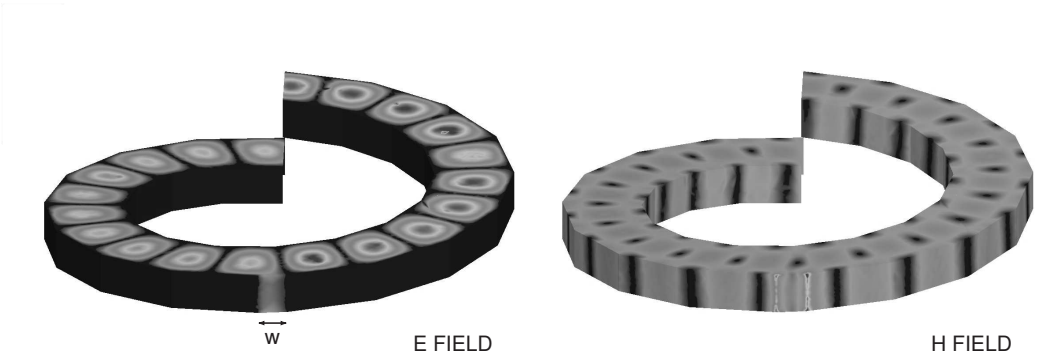

Figure 6.6: The E and H field distribution of the TE_{10} mode travelling through a single helical waveguide turn with a 1.5 mm wide narrow wall slot are shown. Note the quasi-uniform field distribution in the slot.

A recursive equation is derived to determine a slot width taper allowing uniform excitation. Let $\mathfrak{T} = |S_{21}|^2(w = 0mm)$ be the transmitted power fraction of a helical waveguide turn without slot and let $\mathfrak{R}_n = P_r/P_n$ be the radiated power fraction referring to the input of turn n. $\mathfrak{R}_n$ can be calculated recursively based on knowledge of $\mathfrak{T}$ and an initial guess of P_r which is the power radiated by the helix, using (6.8),

$$\mathfrak{R}_n = \frac{\mathfrak{R}_{n-1}}{\mathfrak{T}\,(1 - \mathfrak{R}_{n-1})} \tag{6.8}$$

in which $\mathfrak{R}_1 = P_r/N$. Fig. 6.7(b) is used as a lookup table for determination of the slot widths w_n once radiated power fractions $\mathfrak{R}_n$ are calculated. The slot widths w_n need to be between 0.2 and 1.5 mm as discussed earlier and if necessary P_r needs to be adjusted.

Table 6.2 for an 8 turn helical waveguide-fed slot array, currently under construction at Penn Engineering. Note that the above method does not allow for prediction of the effect of mutual coupling on the scan impedance and proper working of the waveguide-fed slot array remains to be validated experimentally.

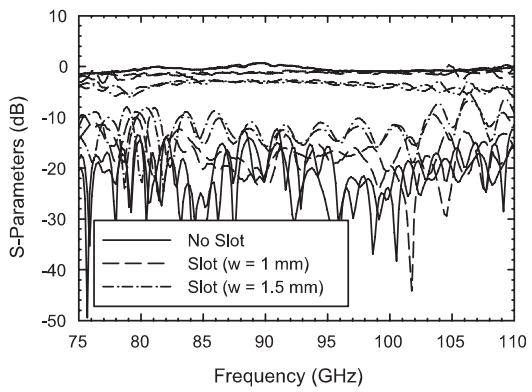

(a) Measured S-parameters of the helical waveguide turns.

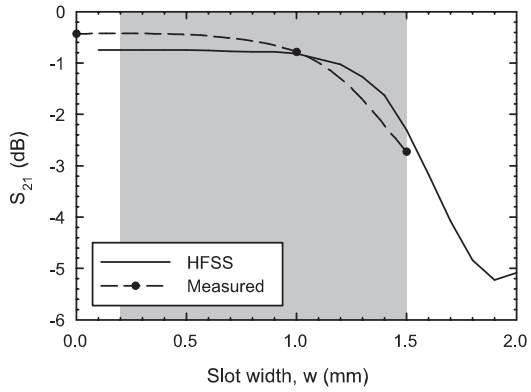

(b) The $|S_{21}|(w)$ data points are compared to HFSS simulation results at 94 GHz.

Figure 6.7: Measured S-parameters of the helical waveguide turns.

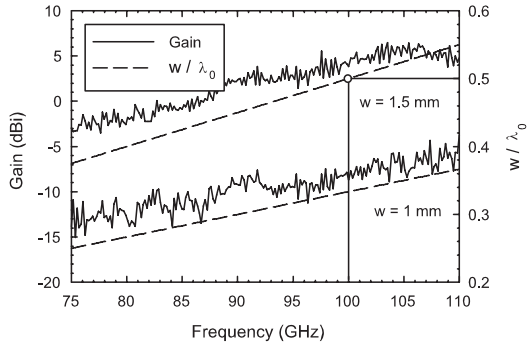

(a) Co-polarized gain.

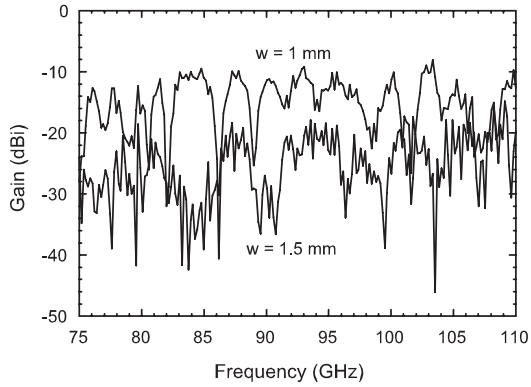

(b) Cross-polarized gain.

Figure 6.8: Measured gain of the helical waveguide turns at boresight.

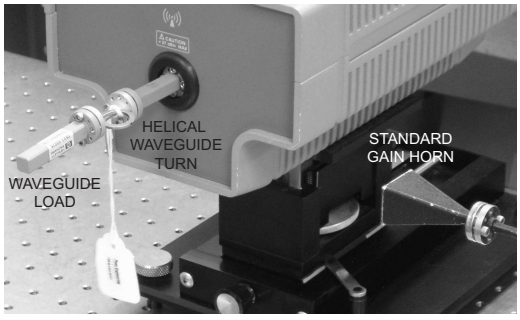

Figure 6.9: Gain measurement of a helical waveguide turn with a 1.5 mm wide narrow wall slot.

Table 6.2: $\mathfrak{R}_n$ and w_n for an 8 turn helical waveguide-fed slot array ($\mathfrak{T}$ = 91.20 % and $\mathfrak{R}_1$ = 7.00 %).

$\mathfrak{R}_1$	7 %	w_1	0.2 mm	$\mathfrak{R}_5$	14.95 %	w_1	1.2 mm
$\mathfrak{R}_2$	8.25 %	w_1	0.9 mm	$\mathfrak{R}_6$	19.27 %	w_1	1.3 mm
$\mathfrak{R}_3$	9.86 %	w_1	1.0 mm	$\mathfrak{R}_7$	26.88 %	w_1	1.4 mm
$\mathfrak{R}_4$	12.00 %	w_1	1.1 mm	$\mathfrak{R}_8$	38.88 %	w_1	1.5 mm

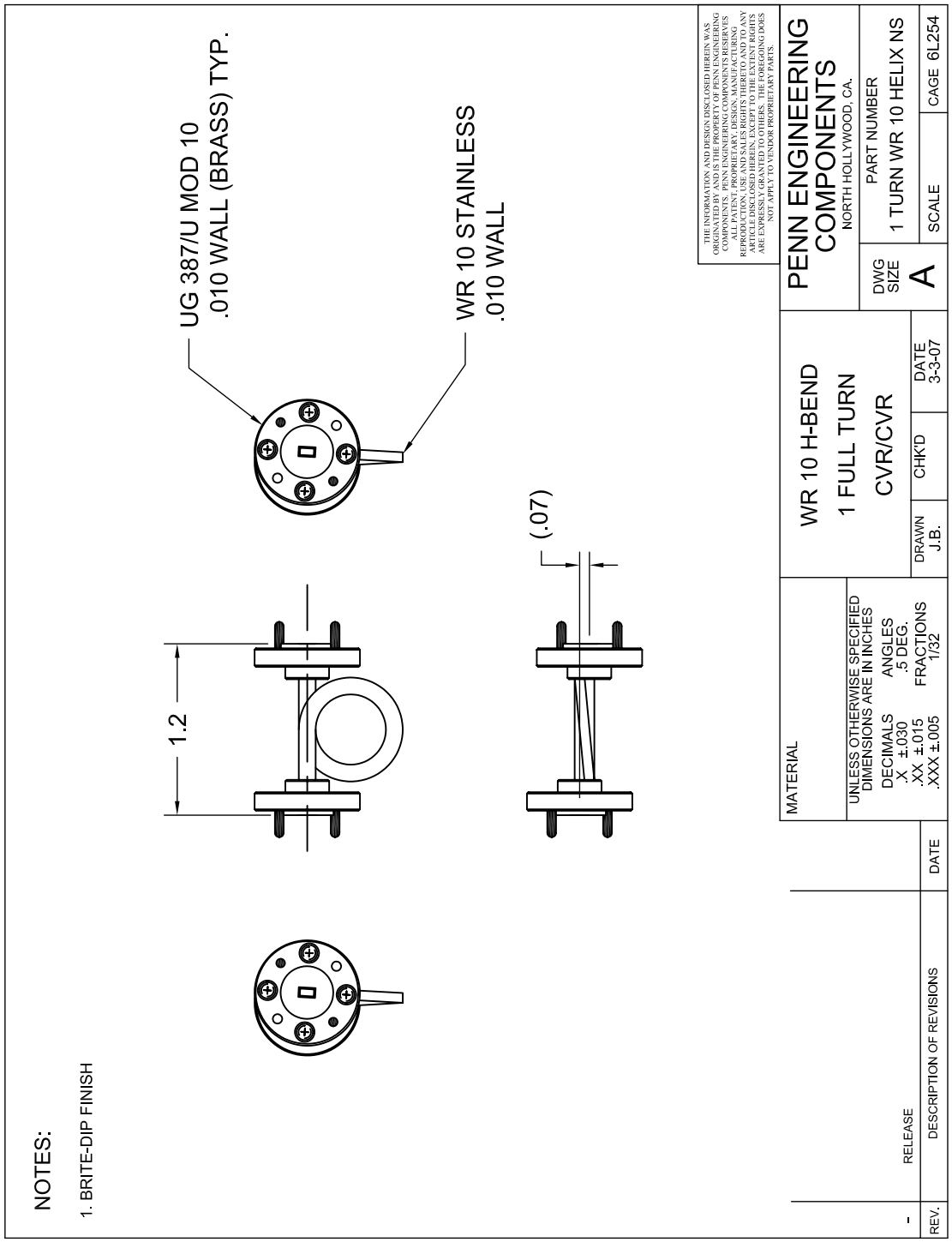

Figure 6.10: Mechanical drawing of the helical waveguide turns with varying slot width (w = 0 mm, 1 mm and 1.5 mm).

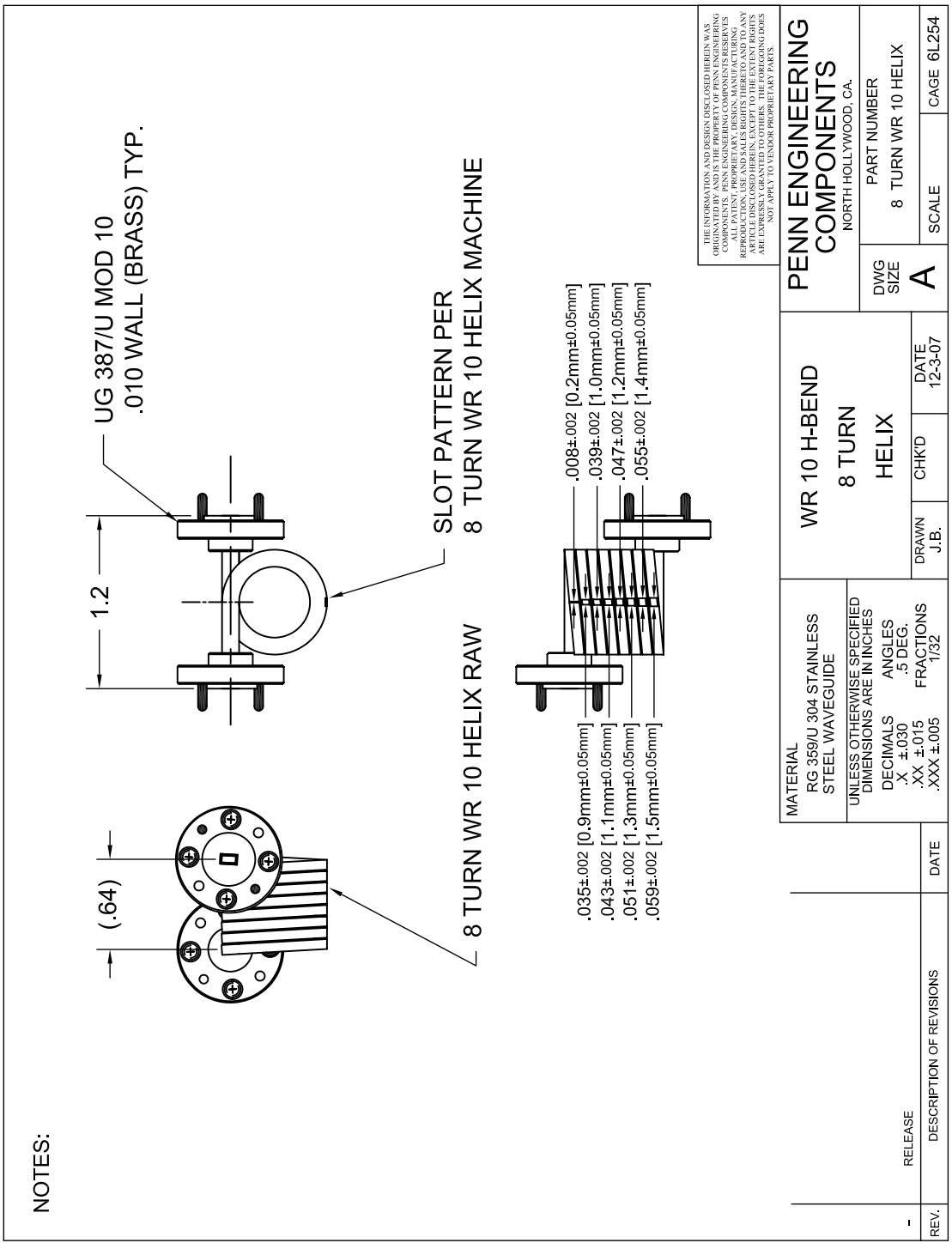

Figure 6.11: Mechanical drawing of the 8 turn helical waveguide-fed slot array.

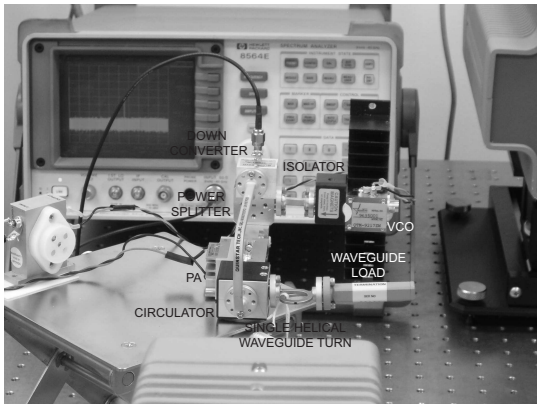

Figure 6.12: A 94 GHz T/R module with 2 GHz bandwidth is assembled based on commercial off-the-shelf WR-10 waveguide components for short-range indoor concept validation.

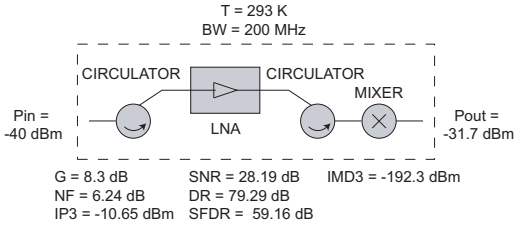

Figure 6.13: Block diagram and specifications of the receiver of the T/R module.

6.3.2 T/R Module

A 94 GHz T/R module with 2 GHz bandwidth is assembled based on commercial off-the-shelf WR-10 waveguide components for short-range indoor concept validation, as shown in Fig. 6.12. The design is optimized for peak transmit power (17.4 dBm) and spurious-free dynamic range at the receiver side (59.16 dB). The receiver has a gain of 8.3 dB, a noise figure (NF) of 6.24 dB and an input IP3 of -10.65 dBm. Other specifications are given in Fig. 6.13. The assembled T/R module consists of two circulators, an LNA, a mixer and a PA.

- **Circulator**: The Quinstar QJY-95023W circulator has an insertion loss of 1.6 dB and an isolation of 35 dB.
- **LNA**: The Quinstar QLN-95024520-00 LNA delivers 20 dB gain. Its noise figure is 4.5 dB and its P1dB is -10 dBm at 94 GHz.

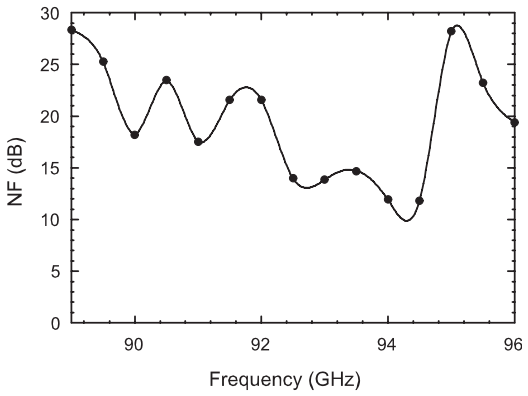

Figure 6.14: The noise figure (RF to IF) of a prototype T/R module without LNA

- **Mixer**: The Millitech MXP-10-RSSSL balanced mixer has a conversion loss of 8.5 dB and an IP3 of 3 dBm.
- **PA**: The Millitech AMP-10-02190 PA has 26 dB of gain over the 91 to 94 GHz frequency range and its P1dB is 19 dBm.

The noise figure (RF to IF) of a prototype T/R module without LNA is measured and shown in Fig. 6.14. Ideally, the T/R module should have 4 GHz of bandwidth to accommodate frequency scanning up to 20° from the boresight. Note that to achieve the range requirements, a 25 kW pulsed klystron would be needed as well.

6.3.3 OFDM Transceiver

The OFDM radar waveform is implemented using an MB-OFDM chipset evaluation board of one of the WiMedia Alliance members, such as the WisAir DV9110 UWB Development Kit. MB-OFDM utilizes 7.5 GHz of unlicensed spectrum from 3.1 to 10.6 GHz allocated by the Federal Communications Commission (FCC) for UWB communication. It divides the spectrum in 14 subbands of 528 MHz, which is the minimum instantaneous signal bandwidth required by the FCC, as shown in Fig. 6.15. UWB transceivers are furthermore half-duplex and compatible with pulsed radar operation. The OFDM radar waveform could also be implemented using an Agilent E8267D PSG vector signal generator which has an external I/Q modulation bandwidth of 2 GHz in order to demonstrate the OFDM FSR concept in transmit mode.

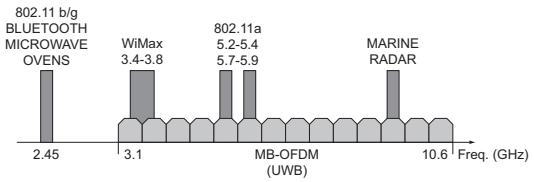

Figure 6.15: MB-OFDM utilizes 7.5 GHz of unlicensed spectrum from 3.1 to 10.6 GHz allocated by the Federal Communications Commission (FCC) for UWB communication. It divides the spectrum in 14 subbands of 528 MHz.

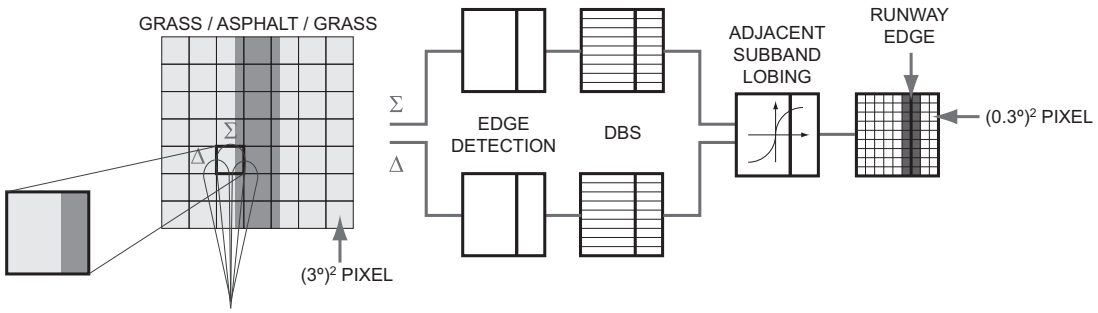

Figure 6.16: Beam sharpening is used to synthetically improve the angular resolution.

6.3.4 Radar Signal Processing

Millimeter-wave radar imagery suffers from a multitude of quality degradations, among which poor contrast, angular resolution loss, motion-induced distortion and blurring, and low SNR are the most troublesome. Temporal filters are used to reduce the scintillation effect and beam sharpening is used to synthetically improve the angular resolution. The along-track resolution is increased beyond real aperture beamwidth using DBS processing which uses the Doppler frequency shift to range discriminate between echoes received in the same range bin, as shown in Fig. 6.16. The cross-track resolution is increased beyond real aperture beamwidth using adjacent subband lobing processing, which interpolates the angular position by comparing the amplitude of echoes received in adjacent subbands, which correspond to adjacent beams, after edge detection filtering. The edge detection filter transforms the ground map from a distributed target to a constellation of point and line targets, as shown in Fig. 6.17.

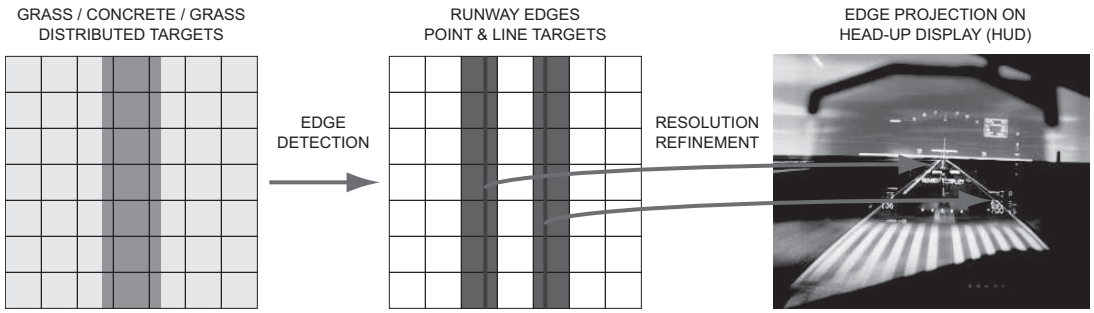

Figure 6.17: Distributed target to line target transformation (the right figure is an artist's rendition by NASA).

6.4 Discussion

To summarize, a list of all pros and cons (italic) is given for architectural choices made:

- **Why FSR?**
  - A passive phased array implementation, requiring only one T/R module, allows the use of high-power vacuum electronics devices (VEDs), like klystrons and travelling-wave tube (TWT) amplifiers.
  - There is no need for phase shifters or additional power combining (dividing) networks.
  - A stainless steel implementation allows 0.5 mm thick waveguide walls and dense element spacing with grating lobes entering the visible region when scanning beyond 20° from the boresight above 96 GHz.
  - *The beamwidth is related to the signal bandwidth, and hence the cross-track (azimuth) and pulse-limited slant range resolution are coupled resulting in an angle-Doppler-range ambiguity function.*
  - *Waveguide-fed slot arrays are not amenable to monopulse techniques.*
  - *Waveguide-fed slot arrays have a high cross-polarization and are incapable of polarimetric imaging.*
- **Why OFDM?**

- All scanning angles are measured at once, providing the pilot with an adequate refresh rate of the radar image.
- Single-chip RF CMOS radios for multiband OFDM (MB-OFDM), as advocated by the WiMedia Alliance, will provide cost-effective half-duplex ultra-wideband transceivers.
- Freedom of choice in I/Q modulation and demodulation of a subband. Every subband, containing an echoed pulse-Doppler waveform, can be 256 QAM demodulated for example.

- **Why pulse-Doppler?**
  - Longer range than frequency modulated continuous wave (FMCW) radar through usage of half-duplex T/R modules. Time-sharing of a single antenna for transmitter and receiver. Frequency modulated interrupted continuous wave (FMICW), though, allows half-duplex operation as well.
  - The along-track resolution can be increased beyond real aperture beamwidth using DBS processing.
  - The cross-track resolution can be increased beyond real aperture beamwidth using adjacent subband lobing.
  - *No pulse compression is used because it leads to coupling of range and Doppler frequency shift and to a more ambiguous Doppler frequency shift detection. However, shorter pulses require a higher PMEPR in order to maintain the SNR.*

- **Why waveguide?**
  - Low-loss compared to printed circuit implementations, resulting in high antenna gain and good receiver NF.
  - Highest available transmit power (>25 kW) through usage of VEDs. High receiver input IP3.
  - High EIRP or power-aperture product and high dynamic range which translates to increased range detection.
  - Wideband, the helical waveguide-fed slot array and the T/R module are WR-10 flanged and no mode conversions are made.

- WR-10 waveguide components, such as circulators, limiters, LNA's, mixers and power amplifiers (TWT) are commercially available.
- Very broad environmental tolerances, shock and corrosion resistant without specialized packaging.

6.5 Conclusion

In this chapter, a novel 94 GHz orthogonal frequency division multiplexing (OFDM) frequency scanning radar (FSR) concept for autonomous landing guidance (ALG) is presented, which offers potential cost and size reductions over the Cassegrain reflector based legacy design. The concept has potential in the automotive market as the radar sensor for 77 GHz long-range autonomous cruise control (ACC) and forward collision warning systems (FCWS) as well.

Acknowledgements

Mr. Jerry Brett of Penn Engineering is thanked for his advice on designing a manufacturable helical waveguide-fed slot array. Mr. Mustafa Rangwala of the University of Michigan, Ann Arbor, is thanked for assembling and testing the T/R module.

APPENDICES

Appendix A

A 2 to 40 GHz Probe Station Based Setup for On-Wafer Antenna Measurements

A.1 Introduction

The characterization of printed electrically small antennas for centimeter-wave radios, or printed array elements for millimeter-wave radars, poses several challenges for traditional antenna ranges, such as the compact antenna test range (CATR) [90, 91, 92], the far field and the near field antenna range [93, 94, 95, 96, 97]. Firstly, the aforementioned antennas - henceforth referred to as antennas under test (AUTs), are often smaller than the interconnection solution of the antenna range. As such, the interconnection solution, whether a coaxial connector or a waveguide flange, changes the aperture efficiency or self-impedance of the AUT. Secondly, they are often fabricated on brittle semiconductor or dielectric wafers, or multi-layer laminates, which cannot be readily packaged.

RF probing represents a small interconnection solution and obviates wafer dicing and custom-made test fixtures. Probe-tip return loss measurements have become common practice but probe-tip radiation pattern measurements are rarely applied. Two far field radiation pattern measurement techniques have been reported. The first technique uses an on-wafer integrated power meter, such as a bismuth or tellurium micro-bolometer based envelope detector [98, 99], or Schottky diode based envelope detector [100, 101]. In general, power meters are sensitive to 1/f noise, and require the AUT to be matched to the power meter and DC decoupled from it. In addition, an AUT with an on-wafer integrated power meter cannot be used for return loss measurements. The second technique, probe-tip radiation pattern measurements [102, 103, 104, 105], is a more convenient and less invasive technique

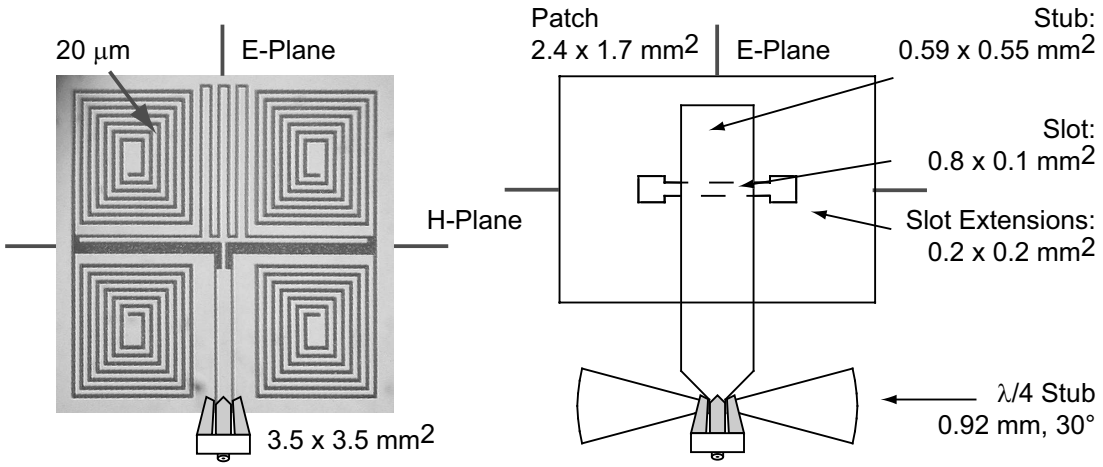

Figure A.1: Optical microscopy imagery of the low-band AUT: 2.45 GHz electrically short slot antenna (left), and the layout of the high-band AUT: 38 GHz aperture coupled microstrip antenna (right).

for on-wafer antennas fabricated in plurality, as it allows for measurement of the return loss, gain and radiation patterns. In addition, the AUT is probed where it will be connected to a transceiver IC later on, obviating the de-embedding of the measured data. Near field sampling with an electro-optic probe [106, 107], and with an electrically small slot antenna [108, 109] has been conducted as well.

A chronology of the prior art of far-field setups for probe-tip radiation pattern measurements is tabulated in Table A.1. In contrast to [102, 103, 104, 105], this chapter discusses a probe station based setup for on-wafer return loss and radiation pattern measurements of bi-directionally and broadside radiating AUTs, with the RF probe and probe positioner located in the measured half space. All aspects are discussed: the AUTs, the transmit and gain reference antennas, the setup which is based on a probe station and a single-axis positioner, return loss and radiation pattern measurements, and sources of error.

A.2 AUTs

The performance of the setup is demonstrated from 2 to 40 GHz through measurement of two AUTs.

Table A.1: Comparison of probe station based setups for on-wafer antenna measurements

	Simons, et al. 1999, [102]	Simons, et al. 2002, [110, 103]	Lin, et al. 2004, [104]	Zwick, et al. 2004, [105]	This work	
AUT properties						
Frequency	27.5-29 GHz	24 GHz	24 GHz	50-65 GHz	2.45 GHz	38 GHz
Gain (efficiency)	11 dBi	-	10-15%	4-7 dBi	-15 dBi	6 dBi
Size	38.1 × 23.3 mm^2	2.6 × 1.5 mm^2	2 × 0.03 mm^2	12 × 12.8 mm^2	3.5 × 3.5 mm^2	2.4 × 1.7 mm^2
Substrate	RT/Duroid 6010	silicon	silicon	fused silica	fused silica	fused silica & TMM3
Type	LTSA (end-fire)	patch (broadside)	dipole (broadside)	Vivaldi (end-fire)	slot (broadside)	patch (broadside)
Setup properties						
Field of view	0-180°	0-180°	90°	0-180°	50-130°	50-130°
Receiver	VNA	VNA	VNA	VNA	VNA/SA	VNA/SA
RF Probe	GS	GSG	SS	GSG	GSG	GSG
Transmit antenna	AUT to AUT	open-ended WR-42	AUT to AUT	WR-15 SGH	2.45 GHz patch	WR-28 SGH
Wafer chuck	styrofoam	absorbing sheet	Delrin ($\epsilon_r = 3.7$)	dielectric	absorbing cavity	absorbing cavity

A.2.1 Low-Band AUT: 2.45 GHz Electrically Short Slot Antenna

The low-band AUT is a 2.45 GHz electrically small slot antenna ($\lambda_0/35 \times \lambda_0/35$, 3.5 $\times$ 3.5 mm^2), shown in Fig. A.1. Miniaturization, which reduces the bandwidth or the efficiency, is achieved through symmetric inductive loading of a very small slot section [111]. It is fabricated on a low-loss fused silica wafer ($\epsilon_r = 3.78$, $h = 500$ μm). It has a simulated fractional bandwidth[1] of 3.7% (90 MHz), and a directivity of 2.27 dBi. It is difficult to accurately simulate the gain of an electrically small antenna because for inefficient antennas, small variations in the return loss cause large variations in gain.

A.2.2 High-Band AUT: 38 GHz Aperture Coupled Microstrip Antenna

The high-band AUT is a 38 GHz aperture coupled microstrip antenna, as shown in Fig. A.1. The patch is printed on a Rogers TMM3 substrate ($\epsilon_r = 3.3$, $h = 375$ μm), which is the frontside of the laminate. The feed, which includes a microstrip to CPW transition, is printed on a 76.2 mm fused silica wafer ($h = 250$ μm), which is the backside of the laminate. Only the backside gain is measured; the frontside gain could be measured with an on-wafer integrated power meter. The high-band AUT has a simulated fractional bandwidth of 5% (2 GHz), a frontside gain of 6.4 dBi and a backside gain of -7 dBi.

A.3 Transmit & Gain Reference Antenna

The transmit antenna is attached to the single-axis positioner and illuminates the AUT while being moved along a hemispherical cut around the probe station. Important parameters of the transmit antenna are the G/R_{FF}^2 factor, in which G is the gain and R_{FF} is the far field distance, the beam solid angle, Ω, and the weight. A large G/R_{FF}^2 factor increases the sensitivity. A well-aligned transmit antenna with small beam solid angle minimizes forward scattering of nearby objects. Forward scattering causes multipath induced fading. Low weight reduces the torque on the drive gear of the single-axis positioner. The three parameters are a function of the effective aperture, A [89, 112]. G is given by:

$$G = e\frac{4\,\pi}{\lambda^2}\,A \tag{A.1}$$

in which e is the efficiency and λ is the wavelength in free space. R_{FF} is defined as:

[1] The bandwidth is the 10 dB return loss bandwidth.

$$R_{FF} = \frac{2\,D^2}{\lambda} > \frac{2\,A}{\lambda} \tag{A.2}$$

in which D is the largest dimension of A. Ω is given by:

$$\Omega = e\frac{4\,\pi}{G} \tag{A.3}$$

Upon investigation of equations (A.3)-(A.2), it can be appreciated that a trade-off is to be made between the G/R_{FF}^2 factor, and the weight, and Ω - i.e. an antenna with a large G/R_{FF}^2 and low weight, has a low Ω, and vice versa.

A.3.1 Low-Band: 2.45 GHz Microstrip Antennas

The low-band transmit and gain reference antennas are identical 2.45 GHz edge-recessed microstrip antennas, printed on Rogers RT/Duroid 5880 substrate ($\epsilon_r = 2.2$, $h = 3.175$ mm). Microstrip antennas are light-weight and well-suited for use as transmit antennas at lower frequencies, due to the payload weight constraint of the single-axis positioner. The measured fractional bandwidth is 2.4% (60 MHz) and the measured gain at broadside is 7.0 dBi. The G/R_{FF}^2 factor is 5140 m^{-2}, the beam solid angle is 2.5 sr, and the weight is 115 g.

A.3.2 High-Band: WR-28 Standard Gain Pyramidal Horns

The high-band transmit and gain reference antenna are identical WR-28 standard gain pyramidal horn (SGH) antennas from Millitech with a gain of 24 dBi. The G/R_{FF}^2 factor is 174 m^{-2}, the beam solid angle is 0.05 sr, and the weight is 303 g.

The transmit and gain reference antennas could also be substituted for a 2.45 GHz circularly-polarized microstrip antenna or a tooth spiral antenna, or a WR-28 scalar feed horn in combination with a WR-28 orthomode transducer, in order to measure a circularly-polarized AUT, provided that the circularly-polarized AUT is fed by an on-wafer quadrature coupler.

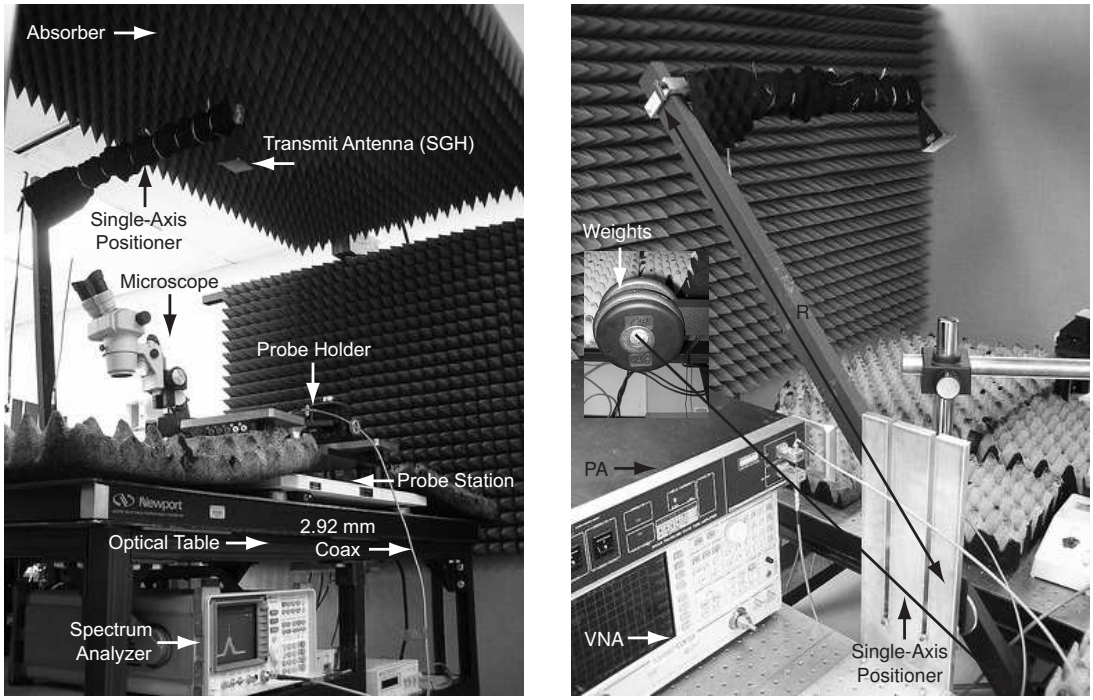

(a) Frontside (b) Backside

Figure A.2: Probe station based setup for on-wafer antenna measurements.

A.4 Setup

The setup is depicted in Fig. A.2(a)-(b). The probe station and the single-axis positioner are mounted on optical tables, contained in a small anechoic chamber based on ETS-Lindgren EHP-24PCL absorber. The probe station is an Alessi RHM-05, equipped with a Nikon 142268 microscope with 30× optical magnification, which is removed during measurements. The on-wafer AUT is placed on top of a cavity filled with Emerson & Cuming ECCOSORB GDS cavity resonance absorber, which is used instead of the probe station vacuum chuck, as shown in Fig. A.3. The E- and H-plane radiation pattern measurements require different probe holders. The probe holder is placed at one side of the probe station, making the setup slightly asymmetric.

The single-axis positioner is a Camera Turret PT-20, based on a Maxon coreless DC motor. Coreless DC motors have a rotor without a permanent magnet, leading to shorter mechanical time constants and less vibration during antenna measurements. A high-accuracy following pod is meshed to the drive gear for angle determination. Unlike a stepper or encoding system, the following pod is able to determine the angular position at all times,

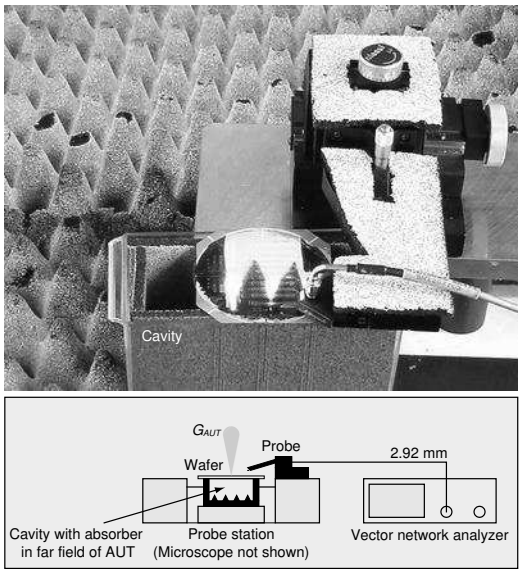

Figure A.3: Laminate with high-band AUTs (top). Setup for measurement of return loss & input impedance (bottom).

even when it is reset. The weight of the transmit antenna is counter balanced with an adjustable weight at the opposite side, to eliminate the torque, as shown in Fig. A.2(b). The arm can be extended to 1.5 meter to assure that the AUT is in the far-field of the transmit antenna. Laser alignment is used to align the AUT and the transmit antenna and to assure that the AUT is centered around the rotation axis of the single-axis positioner, in order to maintain a constant distance between AUT and transmit antenna during radiation pattern measurements.

The frequency range of operation of the setup is 2 to 40 GHz and is bounded by the necessity to satisfy far-field conditions and the maximum operating frequency of the RF probe, the cables, and the equipment.

A.5 Measurements

A.5.1 Return Loss

The AUT is connected to port 1 of a vector network analyzer by a ground-signal-ground probe (Picoprobe 40A-GSG-150-C). A probe-tip short-open-load (SOL) calibration is performed using an impedance standard substrate (Picoprobe CS-5 ISS), and S_{11} time

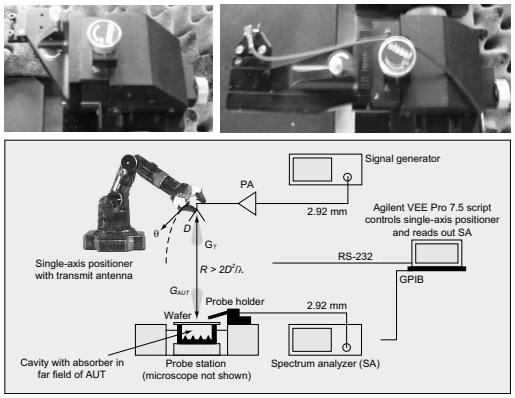

Figure A.4: Setup for measurement of radiation patterns.

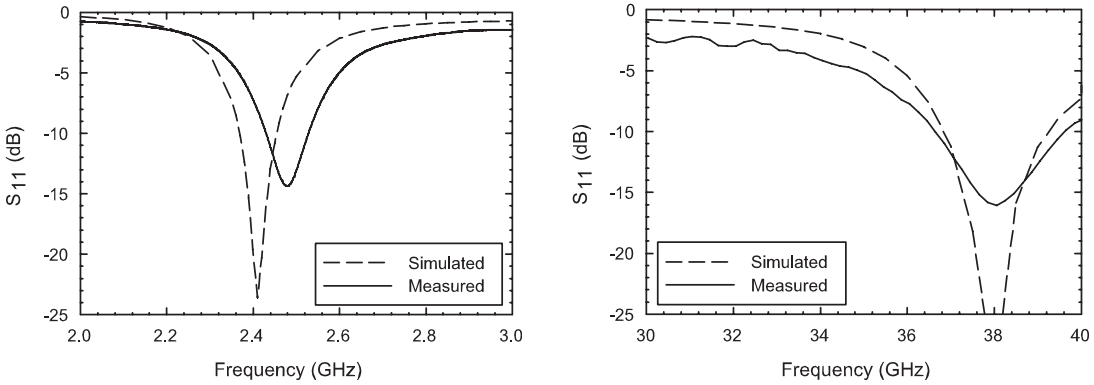

(a) Low-band AUT.

(b) High-band AUT.

Figure A.5: Simulated and measured $|S_{11}|$ results

domain gating is used to avoid reception of echoes during return loss measurements. The low-band AUT has a measured fractional bandwidth of 4.3% (106 MHz) at the design frequency of 2.45 GHz, and the high-band AUT has a fractional bandwidth of 7.8% (3 GHz) at the design frequency of 38 GHz. Simulated and measured results are compared in Fig. A.5(a)-(b) for the low-band and high-band AUT, respectively. The results are in good agreement.

A.5.2 Radiation Patterns

The radiation patterns are measured with the AUT in receive mode. The transmit antenna is mounted on a single-axis positioner while satisfying the far-field region condition ($R = 1$ m for the low-band transmit antenna and 1.2 m for the high-band transmit antenna).

The choice between a vector network analyzer setup and a spectrum analyzer setup depends on the bandwidth and the gain of the AUT. The vector network analyzer setup can only take advantage of S_{21} time domain gating for avoidance of multipath induced fading if the AUT is sufficiently wideband. In addition, the vector network analyzer setup requires the AUT to have a gain higher than 0 dBi, because of the limited dynamic range which is typically 30 dB to 40 dB after calibration. If the AUT has low gain and if the dynamic range becomes an issue, then a spectrum analyzer setup is recommended. In a spectrum analyzer setup, as shown in Fig. A.4, the transmit antenna is connected to a signal generator or a vector network analyzer operating in continuous wave (CW) mode, and the AUT is connected to a spectrum analyzer. The gain is calculated by replacing the AUT by a reference antenna with known gain.

Vector Network Analyzer Setup

Gain is derived from the measured S_{21} using the Friis transmission formula. Note that the transmit antenna is connected to port 2 of the vector network analyzer, after coaxial SOL calibration and S_{21} time domain gating is used to avoid fading due to multi-path during transmission measurements. The absolute-gain measurement technique is used to determine the gain of the identical low-band and high-band transmit (G_T) and reference (G_{REF}) antennas [89, 112]. The vector network analyzer setup is used after coaxial calibration at transmit and receive side.

$$\begin{aligned} (G_T)_{dB} &= (G_{REF})_{dB} \\ &= \frac{1}{2}\left[20\log_{10}\left(\frac{4\pi R}{\lambda}\right) + 20\log_{10}\left(|S_{21}|\right)\right] \end{aligned} \tag{A.4}$$

The measured gain of the the low-band transmit and reference antenna is 7.0 dBi at broadside. The measured gain of the high-band transmit and reference antenna is 24 dBi at 38 GHz.

Spectrum Analyzer Setup

The gain of the low-band AUT and the backside radiation gain of the high-band AUT are anticipated to be low and in the order of 0 to -20 dBi. A spectrum analyzer setup is therefore used to accommodate increased dynamic range. The gain-comparison measure-

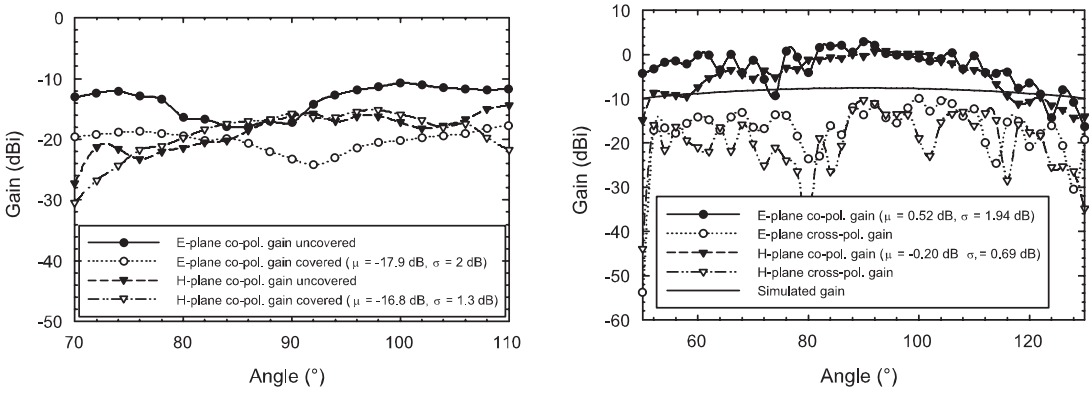

(a) Low-band AUT.

(b) High-band AUT.

Figure A.6: Measured radiation patterns

ment technique is used to find the gain of the AUT [89, 112]. The technique utilizes the reference antenna as a gain standard to determine the gain of the AUT, using

$$(G_{AUT})_{dB} = (G_{REF})_{dB} + 10\log_{10}(\frac{P_{AUT}}{P_{REF}}) \tag{A.5}$$

in which P_{AUT} is the received power through the AUT, and P_{REF} is the received power through the gain reference antenna.

The co-polarized radiation patterns of the low-band AUT are measured with and without Emerson & Cuming ECCOSORB LS 24 absorber covering the probe holder, as shown in Fig. A.6(a), in order to study the effect of multi-path induced fading. The E-plane radiation pattern suffers from more amplitude ripple than the H-plane radiation pattern because the E-plane probe holder is closer to the AUT than the H-plane probe holder. It is concluded that the forward scattering from nearby objects such as the RF probe and probe holder, is the primary source of error. The measured gain at broadside, derived from the covered probe H-plane measurement is -15 dBi, which corresponds to a radiation efficiency of 2.4%. The cross-polarized radiation patterns could not be measured because the received power is below the sensitivity of the probe station.

The measured backside co-polarized gain of the high-band AUT at broadside is 0 dBi, which is 6.4 dB less than the front side radiation. The measured backside cross-polarized gain at broadside is -10 dB. The results are shown in Fig. A.6(b).

Sources of Error

Sources of measurement error are related to gain calibration, insufficient dynamic range, misalignment between AUT, transmit antenna and rotation axis of the single-axis positioner, forward scattering from the RF probe and probe positioner, and vibration:

- **Gain Calibration**: Since the reference antennas have a coaxial connector, the additional loss of the microwave probe must be taken into account in order to achieve an accurate gain measurement at the probe tips. The insertion loss of coplanar microwave probes is characterized by the vendor before shipment to the customer. The measured gain is therefore augmented with 0.25 dB at 2.45 GHz and 0.75 dB at 38 GHz. The 0.3 dB insertion loss of the HP R281A WR-28 waveguide to 2.4 mm adapter is subtracted from the measured gain.

- **Dynamic Range**: The low-band sensitivity of the setup is limited by SMA coaxial cable leakage through its braided sheath, and sets a lower boundary for measurement of the cross-polarized radiation patterns. The measured sensitivity is -25 dBi. The dynamic range could be increased by using a power amplifier in the transmit path, or a low noise amplifier or lock-in amplifier in the receive path. The high-band sensitivity of the setup is limited by thermal noise. Note that high-end 2.92 mm coaxial cables from Gore-Tex and Micro-Coax are used. The dynamic range is increased substantially by adding the Hughes 8001H TWT power amplifier in the transmit path, with a minimal output power of 1 W over the Ka-band. Usage of a power amplifier at Ka-band is necessary to overcome path loss and measure the radiation patterns of low-gain antennas or the nulls and the side-lobes of antenna arrays.

- **Misalignment**: Angular misalignment between the AUT and the transmit antenna leads to polarization loss (gain), during measurement of the co-polarized (cross-polarized) radiation patterns, and is avoided.

- **Scattering**: The field of view of the setup, which is $\pm$ 40° from broadside in the principal planes, is primarily limited by forward scattering of nearby objects such as the RF probe and the probe holder. It also changes the self-impedance and the aperture efficiency of the AUTs. Forward scattering could be improved by reducing the forward radar cross section (RCS) of these objects, for example by covering the

surfaces of obstacles with high quality microwave absorbing tape, such as the Emerson & Cumming ECCOSORB FDS/FF6M, or with ferrite-loaded paint. Geometrical theory of diffraction (GTD) and physical theory of diffraction (PTD) solvers, such as EFIELD or FEKO, could be used to study the effect of the forward scattering and shadow radiation from nearby objects on the radiation pattern.

Given the measurement uncertainty, a statistical approach is used for estimation of the measurement accuracy. The average, μ_G, and standard deviation, σ_G, of the gain within an angular window of 10° from broadside in the principal planes are calculated, as shown in Fig. A.6(a)-(b). σ_G is an indicator for the measurement error caused by the frequency-specific cyclic angular variation of the gain due to forward scattering from the RF probes and probe positioner.

- **Vibration**: Vibration of the optical table through movement of the single-axis positioner displaces and wears off the coplanar microwave probe. The single-axis positioner is therefore installed on a separate platform.

A.6 Conclusion

A probe station based setup is described for on-wafer return loss and radiation pattern measurements of bi-directionally and broadside radiating AUTs, with the RF probe and probe positioner located in the measured half space. The primary source of error is the forward scattering from nearby objects such as the RF probe and probe holder, which causes a frequency-specific angular variation of the measured gain. The standard deviation ranges between 0.69 to 2 dB along broadside direction. Forward scattering also affects the self-impedance and the aperture efficiency of the AUTs, and it could be reduced by reducing the forward RCS of the RF probe and probe holder.

Appendix B

A 2.45 GHz Electrically Small Slot Antenna

B.1 Introduction

Electrically small antennas have gained more attention because of an increased demand for miniaturized short-range wireless communication systems. Contemporary multi-band transceivers have stringent size restrictions and miniature antennas are needed to allow for dense packaging while maintaining low mutual and parasitic coupling [113, 114, 115]. Integration of antennas on-chip through the system-on-a-chip (SoC) approach, or on-package through the system-in-a-package (SiP) approach, reduces overall cost as well.

Fundamental limitations of electrically small antennas have been explored previously [116, 117, 118, 119]. Miniaturization increases the Q factor of the antenna, reduces the antenna efficiency, and makes the matching network complex and lossy. Examples of miniaturization techniques include meandering of the wire antenna, reactive loading [111], and usage of composite left- and right-handed metamaterials [120] and substrates with high dielectric constants.

The 2.45 GHz electrically small slot antenna, shown in Fig. B.1, is a continuation of the work presented in [111], where following modifications have been made: firstly, the antenna is scaled from $\lambda_0/20$ at 300 MHz to $\lambda_0/35$ at 2.45 GHz. Secondly, the critical dimension of the antenna is reduced from 500 μm to 15 μm, requiring micro-fabrication techniques. Thirdly, in order to ease the fabrication, the antenna is redesigned to be uniplanar, with a capacitively-coupled 15/170/15 μm coplanar waveguide (CPW) feed instead of a proximity coupled microstrip feed. Due to the uniplanar nature of the antenna, the effective aperture is not enhanced by the large finite ground plane or by the transceiver chassis [121]. Fourthly,

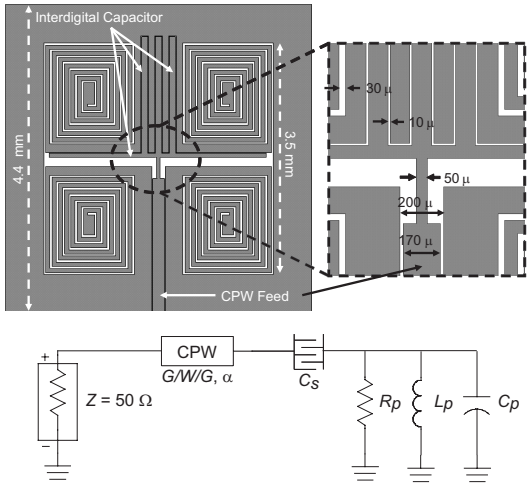

Figure B.1: CAD imagery of the 2.45 GHz electrically small slot antenna with a metal thickness of 2000 Å (top), equivalent lumped circuit model (bottom)

characterization of the antenna, which is too small to be connectorized, is challenging, and a probe-station based setup for on-wafer antenna measurements is used to measure the return loss and gain.

B.2 Design

Miniaturization is achieved through symmetric inductive loading of an electrically small slot section. In order to ensure inductive loading, the length of the spiral slot lines must be less than a quarter wavelength. Usage of two inductive spiral slot lines in series, at both sides of a slot section end, allows for increased inductive loading and a further reduction in size. In addition, the magnetic currents flowing in opposite directions cancel out along the principal planes. Mutual coupling within the spiral slot lines reduces the effective inductance, and therefore, a longer unfolded spiral slot line length is needed compared with a straight slot line, in order to achieve the desired inductance. In order to decrease the self-inductance, a narrow slot width must be chosen for the spiral slot line.

Center-fed electrically small slot antennas have a low radiation conductance at the first resonant frequency and are therefore difficult to match to a 50 Ω transmission line. The resonant frequency of the inductively loaded slot section is therefore designed for a resonance frequency slightly higher than 2.45 GHz, making the antenna slightly inductive at the feed

Table B.1: Equivalent lumped circuit model parameters

	2000 Å	5000 Å
Coupling Capacitance, C_s	118.502 fF	115.2 fF
Parallel Capacitance, C_p	34.7 fF	
Parallel Inductance, L_p	27.8 nH	
Parallel Resistance, R_p	3.7 $k\Omega$	4.3 $k\Omega$

point. An integrated interdigital capacitor is used to capacitively match the antenna to a 50 Ω CPW without the use of an external matching network. While CPW feeding reduces the effective aperture of the antenna, it allows the antenna to be fabricated using a single lithography step and hence eases fabrication. As confirmed by method of moment simulation and measurement results, the antenna does not require an air bridge or bond wire across the CPW to suppress excitation of the odd mode in the CPW.

B.3 Fabrication

The antenna is fabricated on a low-loss fused silica wafer ($\epsilon_r = 3.78$, h = 500 μm, $\tan\delta = 0.0002$) and is defined through a back-etch of a golden metal film. The bandwidth and gain of the antenna, as well as some of the parameters of the equivalent lumped circuit model, tabulated in Table B.1, are found to be a function of the metal thickness, t, which is fraction of the skin depth, δ, due to fabrication constraints. In the Michigan Nanofabrication Facility (MNF), the evaporated metal thickness, t, is limited to 5000 Å, which is 31.5% of the skin depth, δ, at 2.45 GHz. The resistivity of gold, ρ, is 2.44 $\mu\Omega$ cm and the skin depth, δ, is 1.589 μm at 2.45 GHz. The RF sheet resistance, R_s,

$$R_s = \frac{\rho}{t}\frac{1}{1-e^{-t/\delta}} \tag{B.1}$$

of a 2000 Å and 5000 Å film is therefore 0.13 Ω/□ and 0.0569 Ω/□ respectively at 2.45 GHz. The limited thickness increases the losses, and the gain is measured for two designs optimized for two different metal thicknesses: 2000 Å and 5000 Å, in order to study the effect of metal thickness on the bandwidth and the gain. The design requires the interdigital feed capacitance, C_s, to be decreased as the metal thickness, t, is to maintain a good match.

Evaporation is used for two reasons: First, the input impedance of an electrically small antenna is very sensitive to the RF sheet resistance, R_s, of the film, which is inversely related to its achieved thickness. The deviation between achieved and desired thickness is a few Å for evaporation, while it is thousands of Å for electroplating[1]. Secondly, electroplating would require two lithography steps and induce alignment errors. Note that the critical dimension of the design is 15 μm.

B.4 Measurements

The on-wafer electrically small slot antennas, henceforth referred to as antennas under test (AUTs), are measured with a probe station based setup [60], which eliminates the need for wafer dicing, custom-built test fixtures and de-embedding of the measured data.

A 0.5 to 6 GHz probe tip short-open-load (SOL) calibration is performed and the return loss of the AUTs is measured. The 2000 Å AUT has a measured fractional bandwidth of 6.1% (150 MHz), and the 5000 Å AUT has a measured fractional bandwidth of 4.3% (106 MHz) at the design frequency of 2.45 GHz. Lumped circuit model simulation results, fitted to the measurement results, method of moments simulation results, and measurement results are compared in Fig. B.2(a) and Fig. B.2(b), and are in good agreement.

The co-polarized radiation patterns in the principal planes are measured by rotating the wafer over 90° and using an E- or H-plane probe holder. The co-polarized radiation patterns are then remeasured with probe holders covered with absorber, in order to study the effect of multi-path induced fading on the gain measurement. Note that the received power is below the sensitivity of the probe station based setup for the cross-polarized radiation patterns. The co-polarized radiation patterns for both AUTs are shown in Fig. B.2(c) and Fig. B.2(d). It is observed that the E-plane radiation patterns are less smooth and trustworthy than the H-plane radiation patterns. This is due to the fact that the bulk of the E-plane probe holder is closer to the AUT than the H-plane probe holder, obstructing the line-of-sight, as pointed out in [60]. The measured gain at broadside, derived from the H-plane measurements in which the probe is covered with absorber, is -18 dBi for the 2000 Å AUT and -15 dBi for the 5000 Å AUT. This corresponds to a radiation efficiency of 0.86% and 1.6%, with the remaining 99.14% and 98.4% of the power being dissipated in

[1]The Cu-Damascene process of IBM allows for accurate control of the back-end metal thickness up to 4 μm, while maintaining vertical sidewalls [122].

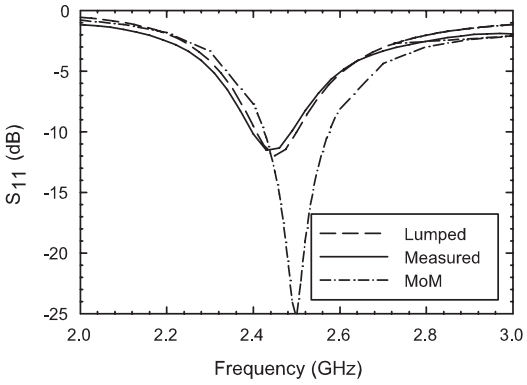

(a) S_{11} of the 2000 Å AUT

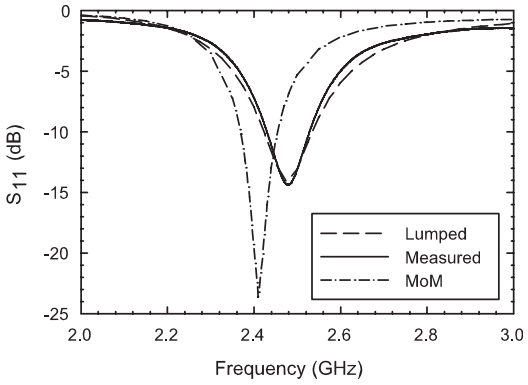

(b) S_{11} of the 5000 Å AUT

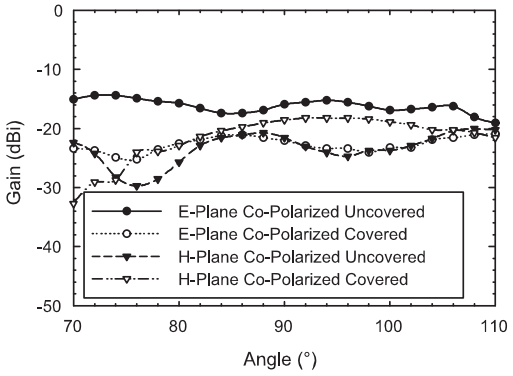

(c) Co-polarized radiation patterns of the 2000 Å AUT

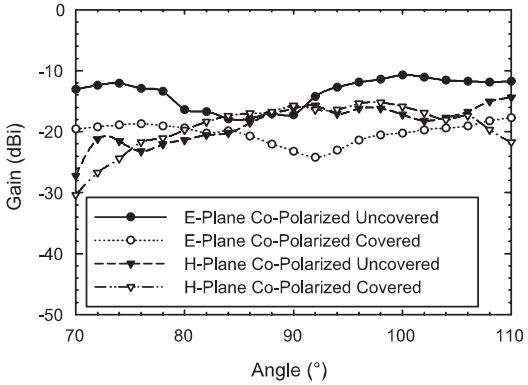

(d) Co-polarized radiation patterns of the 5000 Å AUT

Figure B.2: Probe station based on-wafer measurements

the loss resistance. Imagine dividing up the AUT in squares and multiplying the amount of squares with the RF sheet resistance, R_s; it intuitively explains the high loss resistance of the antenna.

B.5 Discussion

The measurement results are summarized in Table B.2. A measured gain of -15 dBi for the 5000 Å AUT does not violate the theoretical Wheeler-Chu-McLean upper limit and compares to state-of-the-art published results [114, 115]. The theoretical Wheeler-Chu-McLean upper limit for the gain of an electric dipole is given by [117, 118, 119]:

Table B.2: Summary of measured results

	2000 Å	5000 Å
BW_{3dB} (MHz)	550	362.5
BW_{10dB} (MHz)	150	106
f_r (GHz)	2.45	2.475
$G_{MEASURED}$ (dBi)	-18	-15
Q	4.5	6.8
G_{LIMIT} (dBi)	-11.4	-9.6

$$Q = \eta_e \left[\frac{1}{(k\,a)^3} + \frac{1}{k\,a} \right] \approx \frac{\eta_e}{(k\,a)^3} \;\; (k\,a << 1) \tag{B.2}$$

where η_e is the radiation efficiency of the antenna, a is the radius of the smallest sphere that encloses the electrically small antenna, and k is the wavenumber. Losses increase the bandwidth and decrease the Q factor. With $Q = f_r/BW_{3dB} = 6.8$, the theoretical Wheeler-Chu-McLean upper limit for the gain of an $\lambda_0/35 \times \lambda_0/35$ electrically small antenna becomes -9.6 dBi. Regression of bandwidth and gain on metal thickness indicates that a metal thickness of more than 2 μm will decrease the bandwidth to 75 MHz and increase the gain to -12 dBi.

B.6 Conclusion

A 2.45 GHz electrically small slot antenna ($\lambda_0/35 \times \lambda_0/35$, 3.5 × 3.5 mm^2) with a measured bandwidth of 106 MHz and a measured gain of -15 dBi is disclosed.

BIBLIOGRAPHY

BIBLIOGRAPHY

[1] C. Nguyen, "MEMS technology for timing and frequency control," *IEEE Trans. Ultrason., Ferroelect., Freq. Contr.*, vol. 54, no. 2, pp. 251–270, February 2007.

[2] S. Chang and S. Sivoththaman, "A tunable RF MEMS inductor on silicon incorporating an amorphous silicon bimorph in a low-temperature process," *IEEE Electron Device Lett.*, vol. 27, no. 11, pp. 905–907, November 2006.

[3] G. M. Rebeiz, *RF MEMS, Theory, Design and Technology.* John Wiley & Sons, 2003.

[4] C. L. Goldsmith, B. M. Kanack, T.-H. Lin, B. R. Norvell, L. Y. Pang, B. Powers, Jr., C. Rhoads, and D. Seymour, "Micromechanical microwave switching," U.S. Patent 5,619,061, April 8, 1997.

[5] C. L. Goldsmith, Z. Yao, S. Eshelman, and D. Denniston, "Performance of low-loss RF MEMS capacitive switches," *IEEE Microwave Wireless Compon. Lett.*, vol. 8, no. 8, pp. 269–271, August 1998.

[6] P. M. Zavracky, S. Majumder, and N. E. McGruer, "Micromechanical switches fabricated using nickel surface micromachining," *J. Microelectromech. Syst.*, vol. 6, no. 1, pp. 3–9, March 1997.

[7] P. M. Zavracky, N. E. McGruer, R. H. Morrison, and D. Potter, "Microswitches and microrelays with a view toward microwave applications," *International Journal of RF and Microwave Computer Aided Design*, vol. 9, no. 4, pp. 338–347, July 1999.

[8] S. Pranonsatit, A. S. Holmes, I. D. Robertson, and S. Lucyszyn, "Single-pole eight-throw RF MEMS rotary switch," *J. Microelectromech. Syst.*, vol. 15, no. 6, pp. 1735–1744, December 2006.

[9] A. Margomenos and L. P. B. Katehi, "Fabrication and accelerated hermeticity testing of an on-wafer package for RF MEMS," *IEEE Trans. Microwave Theory Tech.*, vol. 52, no. 6, pp. 1626–1636, June 2004.

[10] M. J. Chen, A.-V. H. Pham, N. A. Evers, C. Kapusta, J. Iannotti, W. Kornrumpf, J. Maciel, and N. Karabudak, "Design and development of a package using LCP for RF/microwave MEMS switches," *IEEE Trans. Microwave Theory Tech.*, vol. 54, no. 11, pp. 4009–4015, November 2006.

[11] C. Goldsmith, J. Maciel, and J. McKillop, "Demonstrating reliability," *IEEE Microwave Magazine*, vol. 8, no. 6, pp. 56–60, December 2007.

[12] G. W. Stimson, *Introduction to Airborne Radar, 2nd Ed.* SciTech Publishing, 1998.

[13] P. Lacomme, J.-P. Hardange, J.-C. Marchais, E. Normant, M.-L. Freysz, and R. Hickman, *Air and Spaceborne Radar Systems: An Introduction.* IEE, 2001.

[14] M. I. Skolnik, *Introduction to Radar Systems, 3rd Ed.* McGraw-Hill, 2005.

[15] R. J. Mailloux, *Phased Array Antenna Handbook.* Artech House, 2005.

[16] E. Brookner, *Practical Phased Array Antenna Systems.* Artech House, 1991.

[17] A. Ludloff, *Praxiswissen Radar und Radarsignalverarbeitung, 2. Auflage.* Viewegs Fachbücher der Technik, 1998.

[18] C. G. Christodoulou, "RF MEMS and its applications to microwave systems, antennas and wireless communications," in *Proceedings of the 2003 SBMO/IEEE MTT-S International Microwave and Optoelectronics Conference*, vol. 1, September 2003, pp. 525–531.

[19] D. F. Sievenpiper, "RF MEMS-tuned slot antenna and a method of making same," U.S. Patent 6,864,848, March 8, 2005.

[20] C. Jung, M. Lee, G. P. Li, and F. De Flaviis, "Reconfigurable scan-beam single-arm spiral antenna integrated with RF MEMS switches," *IEEE Trans. Antennas Propagat.*, vol. 54, no. 2, pp. 455–463, February 2006.

[21] G. H. Huff and J. T. Bernhard, "Integration of packaged RF MEMS switches with radiation pattern reconfigurable square spiral microstrip antennas," *IEEE Trans. Antennas Propagat.*, vol. 54, no. 2, pp. 464–469, February 2006.

[22] N. Kingsley, D. E. Anagnostou, M. Tentzeris, and J. Papapolymerou, "RF MEMS sequentially reconfigurable Sierpinski antenna on a flexible organic substrate with novel DC-Biasing technique," *J. Microelectromech. Syst.*, vol. 16, no. 5, pp. 1185–1192, October 2007.

[23] S. Park, K. Lee, and G. M. Rebeiz, "Low-loss 5.15-5.70 GHz RF MEMS switchable filter for wireless LAN applications," *IEEE Trans. Microwave Theory Tech.*, vol. 54, no. 11, pp. 3931–3939, November 2006.

[24] S. Park, K. Van Caekenberghe, and G. M. Rebeiz, "A miniature 2.1 GHz low loss microstrip filter with independent electric and magnetic coupling," *IEEE Microwave Wireless Compon. Lett.*, vol. 14, no. 10, pp. 496–498, October 2004.

[25] G. Tan, R. E. Mihailovich, J. B. Hacker, J. F. DeNatale, and G. M. Rebeiz, "Low-loss 2- and 4-bit TTD MEMS phase shifters based on SP4T switches," *IEEE Trans. Microwave Theory Tech.*, vol. 51, no. 1, pp. 297–304, January 2003.

[26] J. B. Hacker, R. E. Mihailovich, M. Kim, and J. F. DeNatale, "A Ka-band 3-bit RF MEMS true-time-delay network," *IEEE Trans. Microwave Theory Tech.*, vol. 51, no. 1, pp. 305–308, January 2003.

[27] C. D. Nordquist, C. W. Dyck, G. M. Kraus, I. C. Reines, C. L. Goldsmith, W. D. Cowan, T. A. Plut, F. Austin, P. S. Finnegan, M. H. Ballance, and C. T. Sullivan, "A DC to 10 GHz 6-bit RF MEMS time delay circuit," *IEEE Microwave Wireless Compon. Lett.*, vol. 16, no. 5, pp. 305–307, May 2006.

[28] N. S. Barker and G. M. Rebeiz, "Optimization of distributed MEMS phase shifters," in *IEEE MTT-S International Microwave Symposium Digest*, vol. 1, June 1999, pp. 299–302.

[29] A. S. Nagra and R. A. York, "Distributed analog phase shifters with low insertion loss," *IEEE Trans. Microwave Theory Tech.*, vol. 47, no. 9, pp. 1705–1711, September 1999.

[30] N. S. Barker and G. M. Rebeiz, "Optimization of distributed MEMS transmission-line phase shifters - U-band and W-band designs," *IEEE Trans. Microwave Theory Tech.*, vol. 48, no. 11, pp. 1957–1966, November 2000.

[31] J. Perruisseau-Carrier, R. Fritschi, P. Crespo-Valero, and A. K. Skrivervik, "Modeling of periodic distributed MEMS application to the design of variable true-time delay lines," *IEEE Trans. Microwave Theory Tech.*, vol. 54, no. 1, pp. 383–392, January 2006.

[32] B. Lakshminarayanan and T. M. Weller, "Design and modeling of 4-bit slow-wave MEMS phase shifters," *IEEE Trans. Microwave Theory Tech.*, vol. 54, no. 1, pp. 120–127, January 2006.

[33] ——, "Optimization and implementation of impedance-matched true-time-delay phase shifters on quartz substrate," *IEEE Trans. Microwave Theory Tech.*, vol. 55, no. 2, pp. 335–342, February 2007.

[34] J. J. Lee, C. Quan, and B. M. Pierce, "Low-cost 2-D electronically scanned array with compact CTS feed and MEMS phase shifters," U.S. Patent 6,677,899, January 13, 2004.

[35] C. Quan, J. J. Lee, B. M. Pierce, and R. C. Allison, "Wideband 2-D electronically scanned array with compact CTS feed and MEMS phase shifters," U.S. Patent 6,822,615, November 23, 2004.

[36] J. J. Maciel, J. F. Slocum, J. K. Smith, and J. Turtle, "MEMS electronically steerable antennas for fire control radars," *IEEE Aerosp. Electron. Syst. Mag*, vol. 22, no. 11, pp. 17–20, November 2007.

[37] J. Schoebel, T. Buck, M. Reimann, M. Ulm, M. Schneider, A. Jourdain, G. J. Carchon, and H. A. C. Tilmans, "Design considerations and technology assessment of phased-array antenna systems with RF MEMS for automotive radar applications," *IEEE Trans. Microwave Theory Tech.*, vol. 53, no. 6, pp. 1968–1975, June 2005.

[38] X-band T/R module block diagram. [Online]. Available: http://www.macom.com/markets/aerospacedefense/cots.asp

[39] K. J. Herrick, G. Jerinic, R. P. Molfino, S. M. Lardizabal, and B. Pillans, "S-Ku band intelligent amplifier microsystem," *Proceedings of the SPIE*, vol. 6232, May 2006.

[40] T. Vähä-Heikkilä, J. Varis, and G. Rebeiz, "A 20-50 GHz RF MEMS single-stub impedance tuner," *IEEE Microwave Wireless Compon. Lett.*, vol. 15, no. 4, pp. 205–207, April 2005.

[41] J. C. Sarace, R. E. Kerwin, D. L. Klein, and R. Edwards, "Metal-nitride-oxide-silicon field effect transistors with self-aligned gate," *J. Solid-State Electronics*, vol. 11, no. 7, pp. 653–660, July 1968.

[42] M. E. Alperin, T. C. Holloway, R. A. Haken, C. D. Gosmeyer, R. V. Karnaugh, and W. D. Parmantie, "Development of the self-aligned titanium silicide process for VLSI applications," *IEEE J. Solid-State Circuits*, vol. 20, no. 1, pp. 61–69, February 1985.

[43] P. D. Agnello, "Process requirements for continued scaling of CMOS - the need and prospects for atomic-level manipulation," *IBM J. Res. & Dev.*, vol. 46, no. 2/3, pp. 317–338, March/May 2002.

[44] N. S. Barker, "The future of N/MEMS," *IEEE Microwave Magazine*, vol. 8, no. 6, pp. 52–55, December 2007.

[45] D. Mercier, K. Van Caekenberghe, and G. M. Rebeiz, "Miniature RF MEMS switched capacitors," in *IEEE MTT-S International Microwave Symposium Digest*, June 2005.

[46] B. Lacroix, A. Pothier, A. Crunteanu, C. Cibert, F. Dumas-Bouchiat, C. Champeaux, A. Catherinot, and P. Blondy, "Sub-microsecond RF MEMS switched capacitors," *IEEE Trans. Microwave Theory Tech.*, vol. 55, no. 6, pp. 1314–1321, June 2007.

[47] S.-J. Park, K.-Y. Lee, and G. M. Rebeiz, "Low-loss 5.15-5.70 GHz RF MEMS switchable filter for wireless LAN applications," *IEEE Trans. Microwave Theory Tech.*, vol. 54, no. 11, pp. 3931–3939, November 2006.

[48] T. Vähä-Heikkilä, K. Van Caekenberghe, J. Varis, J. Tuovinen, and G. M. Rebeiz, "RF MEMS impedance tuners for 6-24 GHz applications," *Wiley Interscience International Journal of RF and Microwave Computer-Aided Engineering*, vol. 17, no. 3, pp. 265–278, May 2007.

[49] C. L. Goldsmith, "Proximity micro-electromechanical system," U.S. Patent 6,608,268, August 19, 2003.

[50] R. A. York, A. S. Nagra, and A. Borgioli, "Capacitive microelectromechanical switches," U.S. Patent 6,452,124, September 17, 2002.

[51] B. Pillans, J. Kleber, C. Goldsmith, and M. Eberly, "RF power handling of capacitive RF MEMS devices," in *IEEE MTT-S International Microwave Symposium Digest*, June 2002.

[52] J. M. Bustillo, R. T. Howe, and R. S. Muller, "Surface micromachining for microelectromechanical systems," *Proc. IEEE*, vol. 86, no. 8, pp. 1552–1574, August 1998.

[53] K. R. Williams and R. S. Muller, "Etch rates for micromachining processing," *J. Microelectromech. Syst.*, vol. 5, no. 4, pp. 256–269, December 1996.

[54] S. D. Senturia, *Microsystem Design.* Kluwer Academic Publishers, 2001.

[55] K. R. Williams, K. Gupta, and M. Wasilik, "Etch rates for micromachining processing - Part II," *J. Microelectromech. Syst.*, vol. 12, no. 6, pp. 761–778, December 2003.

[56] O. Auciello, S. Pacheco, A. V. Sumant, C. Gudeman, S. Sampath, A. Datta, R. W. Carpick, V. P. Adiga, P. Zurcher, Z. Ma, H.-C. Yuan, J. A. Carlisle, B. Kabius, J. Hiller, and S. Srinivasan, "Are diamonds a MEMS' best friend?" *IEEE Microwave Magazine*, vol. 8, no. 6, pp. 61–75, December 2007.

[57] J. R. Webster, C. W. Dyck, J. P. Sullivan, T. A. Friedmann, and A. J. Carton, "Performance of amorphous diamond RF MEMS capacitive switch," *Electronics Letters*, vol. 40, no. 1, pp. 43–44, January 2004.

[58] B. D. Jensen, K. Saitou, J. L. Volakis, and K. Kurabayashi, "Fully integrated electrothermal multidomain modeling of RF MEMS switches," *IEEE Microwave Wireless Compon. Lett.*, vol. 13, no. 9, pp. 364–366, September 2003.

[59] H. A. Schafft, T. C. Staton, J. Mandel, and J. D. Shott, "Reproducibility of electromigration measurements," *IEEE Trans. Electron Devices*, vol. 34, no. 3, pp. 673–681, March 1987.

[60] K. Van Caekenberghe, K. M. Brakora, K. Jumani, M. Rangwala, Y.-Z. Wee, and K. Sarabandi, "A probe station based setup for on-wafer antenna measurements," in *AMTA Symposium Digest*, October 2006.

[61] K. Van Caekenberghe, T. Vähä-Heikkilä, G. M. Rebeiz, and K. Sarabandi, "Ka-band RF MEMS TTD passive electronically scanned array," in *IEEE AP-S International Symposium Digest*, July 2006.

[62] P. J. Gibson, "The Vivaldi aerial," in *9th European Microwave Conference Digest*, June 1979, pp. 101–105.

[63] J. D. S. Langley, P. S. Hall, and P. Newham, "Novel ultrawide-bandwidth Vivaldi antenna with low crosspolarisation," *Electronics Letters*, vol. 29, no. 23, pp. 2004–2005, November 1993.

[64] J. J. Lee, R. Y. Loo, S. Livingston, V. I. Jones, J. B. Lewis, H.-W. Yen, G. L. Tangonan, and M. Wechsberg, "Photonic wideband array antennas," *IEEE Trans. Antennas Propagat.*, vol. 43, no. 9, pp. 966–982, September 1995.

[65] J. D. S. Langley, P. S. Hall, and P. Newham, "Balanced antipodal vivaldi antenna for wide bandwidth phased arrays," *IEE Proceedings—Microwaves, Antennas and Propagation*, vol. 143, no. 2, pp. 97–102, April 1996.

[66] M. J. Chen, A.-V. Pham, N. Evers, C. Kapusta, J. Iannotti, W. Kornrumpf, and J. Maciel, "Multilayer organic multichip module implementing hybrid microelectromechanical systems," *IEEE Trans. Microwave Theory Tech.*, vol. 56, no. 4, pp. 952–958, April 2008.

[67] G. P. Agrawal, *Fiber-Optic Communication Systems, Second Edition.* John Wiley & Sons, 1997.

[68] K. C. Gupta, R. Garg, I. Bahl, and P. Bhartia, *Microstrip Lines and Slotlines, 2nd Ed.* Artech House, 1996.

[69] G. Gray, "Radar imaging with ALG - the on-board low visibility landing aid," in *IEE Aviation Surveillance Systems*, January 2002.

[70] F. Sadjadi, M. Helgeson, J. Radke, and G. Stein, "Radar synthetic vision system for adverse weather aircraft landing," *IEEE Trans. Aerosp. Electron. Syst.*, vol. 35, no. 1, pp. 2–14, January 1999.

[71] J. Sowers, N. Byer, B. Edward, D. McPherson, S. Weinreb, and F. Rucky, "Electronically steered, receive monopulse, active phased array at 94 GHz," in *IEEE MTT-S International Microwave Symposium Digest*, Jun. 1996.

[72] R. C. Hansen, *Phased Array Antennas*. John Wiley & Sons, 1998.

[73] F. le Chevalier, "Future concepts for electromagnetic detection," *IEEE Aerosp. Electron. Syst. Mag*, vol. 14, no. 10, pp. 9–17, October 1999.

[74] D. Parker and D. C. Zimmermann, "Phased arrays - Part I: Theory and architectures," *IEEE Trans. Microwave Theory Tech.*, vol. 50, no. 3, pp. 678–687, March 2002.

[75] ——, "Phased arrays - Part II: Implementations, applications, and future trends," *IEEE Trans. Microwave Theory Tech.*, vol. 50, no. 3, pp. 688–698, March 2002.

[76] B. Kopp, M. Borkowski, and G. Jerinic, "Transmit/receive modules," *IEEE Trans. Microwave Theory Tech.*, vol. 50, no. 3, pp. 827–834, March 2002.

[77] N. Levanon and E. Mozeson, *Radar Signals*. John Wiley & Sons, 2004.

[78] K. Van Caekenberghe, K. F. Brakora, and K. Sarabandi, "OFDM frequency scanning radar," U.S. Patent 12,233,818 (Utility Patent Application), September 19, 2008.

[79] R. Aiello and A. Batra, *Ultra Wideband Systems*. Newnes, 2006.

[80] H. Arslan, Z. N. Chen, and M.-G. D. Benedetto, *Ultra Wideband Wireless Communication*. John Wiley & Sons, 2006.

[81] M. Ranjan and L. E. Larson, "A low-cost and low-power CMOS receiver front-end for MB-OFDM ultra-wideband systems," *IEEE J. Solid-State Circuits*, vol. 42, no. 3, pp. 592–602, March 2007.

[82] L. H. Hui, "Monopulse thresholding," U.S. Patent 5,450,089, September 12, 1995.

[83] R. C. Johnson, *Antenna Engineering Handbook, 3rd Ed.* McGraw-Hill, 1993.

[84] R. K. Raney, "The delay/doppler radar altimeter," *IEEE Trans. Geosci. Remote Sensing*, vol. 36, no. 5, pp. 1578–1588, September 1998.

[85] J. R. Jensen, "Angle measurement with a phase monopulse radar altimeter," *IEEE Trans. Antennas Propagat.*, vol. 47, no. 4, pp. 715–724, April 1999.

[86] R. E. Collin, *Antennas and Radiowave Propagation*. McGraw-Hill, 1985.

[87] Y. T. Lo and S. W. Lee, *The Antenna Handbook - Volume 2: Antenna Theory*. Van Nostrand Reinhold, 1993.

[88] J. C. Young, J. Hirokawa, and M. Ando, "Analysis of a rectangular waveguide, edge slot array with finite wall thickness," *IEEE Trans. Antennas Propagat.*, vol. 55, no. 3, pp. 812–819, March 2007.

[89] C. A. Balanis, *Antenna Theory, Analysis and Design, 2nd Ed.* John Wiley & Sons, 1997.

[90] MI-Technologies website. [Online]. Available: http://www.mi-technologies.com/

[91] W. D. Burnside, M. C. Gilreath, B. M. Kent, and G. L. Clerici, "Curved edge modification of compact range reflector," *IEEE Trans. Antennas Propagat.*, vol. 35, no. 2, pp. 176–182, February 1987.

[92] J. Tuovinen, A. Vasara, and A. Räisänen, "Compact antenna test range," U.S. Patent 5,670,965, September 23, 1997.

[93] A. D. Yaghjian, "An overview of near-field antenna measurements," *IEEE Trans. Antennas Propagat.*, vol. 34, no. 1, pp. 30–45, January 1986.

[94] R. C. Baird, A. C. Newell, and C. F. Stubenrauch, "A brief history of near-field measurements of antennas at the national bureau of standards," *IEEE Trans. Antennas Propagat.*, vol. 36, no. 6, pp. 727–733, June 1988.

[95] A. C. Newell, "Error analysis techniques for planar near-field measurements," *IEEE Trans. Antennas Propagat.*, vol. 36, no. 6, pp. 754–768, June 1988.

[96] G. Hindman and A. C. Newell, "Simplified spherical near-field accuracy assessment," *IEEE Antennas Propagat. Mag.*, vol. 49, no. 1, pp. 233–240, February 2007.

[97] J. L. Volakis, *Antenna Engineering Handbook, Fourth Edition.* McGraw-Hill, 2007.

[98] D. P. Neikirk, W. W. Lam, and D. B. Rutledge, "Far-infrared microbolometer detectors," *International Journal of Infrared and Millimeter Waves*, vol. 5, no. 3, pp. 245–278, March 1984.

[99] G. P. Gauthier, S. Raman, and G. M. Rebeiz, "A 90-100 GHz double-folded slot antenna," *IEEE Trans. Antennas Propagat.*, vol. 47, no. 6, pp. 1120–1122, June 1999.

[100] G. P. Gauthier, J.-P. Raskin, L. P. B. Katehi, and G. M. Rebeiz, "A 94 GHz aperture coupled micromachined microstrip antenna," *IEEE Trans. Antennas Propagat.*, vol. 47, no. 12, pp. 1761–1766, December 1999.

[101] N. Kingsley, G. E. Ponchak, and J. Papapolymerou, "Reconfigurable RF MEMS phased array antenna integrated within a liquid crystal polymer (LCP) system-on-package," *IEEE Trans. Antennas Propagat.*, vol. 56, no. 1, pp. 108–118, January 2008.

[102] R. N. Simons and R. Q. Lee, "On-wafer characterization of millimeter-wave antennas for wireless applications," *IEEE Trans. Microwave Theory Tech.*, vol. 47, no. 1, pp. 92–96, January 1999.

[103] R. N. Simons, "Novel on-wafer radiation pattern measurement technique for MEMS actuator based reconfigurable patch antennas," in *AMTA Symposium Digest*, November 2002.

[104] J. Lin, L. Gao, A. Sugavanam, X. Guo, R. Li, J. E. Brewer, and K. K. O, "Integrated antennas on silicon substrates for communication over free space," *IEEE Electron Device Lett.*, vol. 25, no. 4, pp. 196–198, April 2004.

[105] T. Zwick, C. Baks, U. R. Pfeiffer, D. Liu, and B. P. Gaucher, "Probe based MMW antenna measurement setup," in *IEEE AP-S International Symposium Digest*, June 2004.

[106] Y. Imaizumi, H. Kamitsuna, M. Shimizu, and H. Ogawa, "Novel planar antenna measurement techniques with electro-optic sampling (EOS)," in *IEEE AP-S International Symposium Digest*, June 1994.

[107] R. M. Reano, W. Thiel, J. F. Whitaker, and L. P. B. Katehi, "Measured and simulated electric, magnetic, and thermal field distributions of a patch antenna operating at high power," in *IEEE AP-S International Symposium Digest*, June 2002.

[108] J. Laurin, J. Zurcher, and F. E. Gardiol, "Near-field diagnostics of small printed antennas using the equivalent magnetic current approach," *IEEE Trans. Antennas Propagat.*, vol. 49, no. 5, pp. 814–828, May 2001.

[109] A. Shamim, L. Roy, N. Fong, and N. G. Tarr, "24 GHz on-chip antennas and balun on bulk Si for air transmission," *IEEE Trans. Antennas Propagat.*, vol. 56, no. 2, pp. 303–311, February 2008.

[110] R. N. Simons, D. Chun, and L. P. B. Katehi, "Microelectromechanical systems (MEMS) actuators for antenna reconfigurability," in *IEEE MTT-S International Microwave Symposium Digest*, June 2001, pp. 215–218.

[111] R. Azadegan and K. Sarabandi, "A novel approach for miniaturization of slot antennas," *IEEE Trans. Antennas Propagat.*, vol. 51, no. 3, pp. 421–429, March 2003.

[112] J. D. Kraus and R. J. Marhefka, *Antennas*. McGraw-Hill, 2001.

[113] C. D. Nallo and A. Faraone, "Multiband internal antenna for mobile phones," *Electronics Letters*, vol. 41, no. 9, April 2005.

[114] K. K. O, K. Kim, B. A. Floyd, J. L. Mehta, H. Yoon, C. Hung, D. Bravo, T. O. Dickson, X. Guo, R. Li, N. Trichy, J. Caserta, W. R. Bomstad, II, J. Branch, D. Yang, J. Bohorquez, E. Seok, L. Gao, A. Sugavanam, J. Lin, J. Chen, and J. Brewer, "On-chip antennas in silicon ICs and their application," *IEEE Trans. Electron Devices*, vol. 52, no. 7, pp. 1312–1323, July 2005.

[115] L. M. Feldner, C. T. Rodenbeck, C. G. Christodoulou, and N. Kinzie, "Electrically small frequency-agile PIFA-as-a-package for portable wireless devices," *IEEE Trans. Antennas Propagat.*, vol. 55, no. 11, pp. 3310–3319, November 2007.

[116] R. C. Hansen, "Fundamental limitations in antennas," *Proc. IEEE*, vol. 69, no. 2, pp. 170–182, February 1981.

[117] J. S. McLean, "A re-examination of the fundamental limits on the radiation Q of electrically small antennas," *IEEE Trans. Antennas Propagat.*, vol. 44, no. 5, pp. 672–676, May 1996.

[118] S. R. Best, "A discussion on the quality factor of impedance matched electrically small wire antennas," *IEEE Trans. Antennas Propagat.*, vol. 53, no. 1, pp. 502–508, January 2005.

[119] A. D. Yaghjian and S. R. Best, "Impedance, bandwidth, and Q of antennas," *IEEE Trans. Antennas Propagat.*, vol. 53, no. 4, pp. 1298–1324, April 2005.

[120] A. Lai, K. M. K. H. Leong, and T. Itoh, "Composite right/left-handed metamaterial antennas," in *2006 IEEE International Workshop on Antenna Technology, Small Antennas, and Novel Metamaterials*, March 2006, pp. 404–407.

[121] P. Vainikainen, J. Ollikainen, O. Kivekäs, and I. Kelander, "Resonator-based analysis of the combination of mobile handset antenna and chassis," *IEEE Trans. Antennas Propagat.*, vol. 50, no. 10, pp. 1433–1444, October 2002.

[122] J. N. Burghartz, D. C. Edelstein, K. A. Jenkins, and Y. H. Kwark, "Spiral inductors and transmission lines in silicon technology using copper-damascene interconnects and low-loss substrates," *IEEE Trans. Microwave Theory Tech.*, vol. 45, no. 10, pp. 1961–1968, October 1997.